Fluid inclusion and $\delta^{18}O$ isotope values of fluids responsible for mineralization in the Hope Reef and Main Reef Complex of the Fairview Mine, Barberton, South Africa

By

Christina Marie Comuso

Thesis presented in fulfilment of the requirements for the degree of Masters of Earth Science, at Stellenbosch University.

Supervisor: Dr. Bjorn P. von der Heyden

March 2020

Declaration

By submitting this thesis electronically, I declare that the entirety of the work contained therein is my own, original work, that I am the authorship owner thereof (unless to the extent explicitly otherwise stated) and that I have not previously in its entirety or in part submitted it for obtaining any qualification.

Christina Marie Comuso

Date: .....

Acknowledgements

I have never expected to pursue a master's degree in South Africa, but it truly has been a gratifying and life changing experience. I am immensely grateful for my undergraduate adviser Dr. Matthew Severs for informing me about the posted MSc position but more importantly I cannot explain how thankful I am for my supervisor Dr. Bjorn von der Heyden. The road of this degree has been a rocky one, through project changes and the unexpected acquired injuries that have set me back in my timeline. Although there was a multitude of obstacles along the way, Bjorn has been there to assist whenever I needed it. Bjorn thanks for all that you have taught me and all your patience during the rough times. I would also like to thank Barberton Mines for allow us access to the Fairview and Sheba Mine, making this study possible.

I want to also thank all the humble people I have met during my time in SA that I now am so happy to call my mates. This experience holds a place in my heart, and I will forever treasure the moments and people who were a part of it. I largely would have not achieved as much as I have without my family and mainly my amazing friends who were there by my side the entire way. I want to give a huge thanks to Professor Chris Harris from the University of Cape Town for assisting with setting up the fluid inclusion laboratory at Stellenbosch University. This project would have never occurred if it wasn't for the funding from DST-NRF-CIMERA and the Society of Economic Geology (SEG). Thank you CIMERA for the two years of funding and thank you SEG for the top up funds that kept this project afloat. All in all, there are no words that I can say nor a single person I can thank for the past two years, I am grateful more than words could explain for everyone who has been a part of my time in South Africa.

Abstract

Gold mineralization within the Fairview Mine of the Barberton Greenstone Belt (BGB) is structurally confined to various mineralized shear zones, better known as reef complexes. Regionally altered lithologic units and structural features promoted large scale fluid migration that in turn resulted in the gold abundance throughout the Fairview Mine. Four progressive deformational phases along with a F_3 folding event of the Ulundi syncline offer the ideal conditions for orogenic gold formation. Grades of mineralization in the HR and MRC are likely due to variations in proximal lithological packages and structural fabrics. Progressive gold rich fluid flow throughout the MRC and HR has led to the high gold endowment in both the reef complexes.

This study focuses on the structurally, lithologically, and temporally different Main Reef Complex (MRC) and the Hope Reef (HR), in order to develop an understanding of the mineralizing fluids that were present throughout both reef complexes. Oriented quartz veins associated with mineralization were analyzed from both the MRC and HR for: (1) oxygen stable isotope values; (2) fluid inclusion types and trapping conditions determined by microthermometry experiments; (3) followed by a constituent analysis of volatiles within fluid inclusions through Raman micro spectroscopy. The perplexities on the composition and origin of the gold mineralizing fluid, as well as the variations in alteration within the MRC and HR, will hopefully be better understood with the data presented in this study.

Fluid inclusion data of secondary and primary inclusions from the HR present homogenization ranges from 185°C to 340°C. Salinity values for these analyzed FI in HR occur at 2.07 to 18.63 wt. %. Moderate clathrate melting temperatures of HR fluid inclusions, 7.90°C to 19.5°C suggest the presence of a thin liquid or vapor film of a more complex volatile, i.e. CH_4, C, HCl, and N_2. Like the HR data of both secondary and primary, FI from the MRC show homogenization ranges from 225.60°C to 400°C. These moderate higher homogenization values are representative of H_20-CO_2 rich hydrothermal fluids. The MRC displays low to moderate salinity's ranging from 2.76 to 16.34 wt. %. Overall clathrate values for the MRC were slightly lower than HR, 1.20°C to18.9°C. Oxygen stable isotope values of selected quartz vein samples at the HR range 12.85 to 14.30‰, similarly, the MRC 13.75 to 14.90‰. Raman spectroscopy was performed on FI within both the

HR and MRC revealing peaks of CO_2, CH_4, H_2O and C. Higher intensities of CH_4 are visible in the MRC then the HR.

Aside from partially dissecting the fluid geochemistry of the MRC and HR, a chapter of this thesis was dedicated to documenting the technique development for the newly established fluid inclusion laboratory in the Department of Earth Science at Stellenbosch University. This brief but concise laboratory manual provides a walkthrough on how to set up and run microthermometry experiments using the Linkam THMS600 heating homogenization and freezing stage, as well as a simple yet informative methodology on how to carry out a fluid inclusion study at Stellenbosch University.

Opsomming

Goudmineralisasie binne die Fairview-myn van die Barberton Greenstone Belt (BGB) is struktureel beperk tot verskillende gemineraliseerde skeersones, beter bekend as rifkomplekse. Regtelik veranderde litologiese eenhede en strukturele kenmerke het grootskaalse vloeistofmigrasie bevorder wat op hul beurt die goudoorvloed regdeur die Fairview-myn tot gevolg gehad het. Vier progressiewe vervormingsfases, tesame met 'n F3-vougebeurtenis van die Ulundi-sinklinie, bied die ideale omstandighede vir orogeniese goudvorming. Grade van mineralisasie in die HR en MRC is waarskynlik te wyte aan variasies in proksimale litologiese pakkette en struktuurstowwe.

Hierdie studie fokus op die struktureel, litologiese en tydelik verskillende Main Reef Complex (MRC) en die Hope Reef (HR), ten einde 'n begrip te ontwikkel van die mineraliserende vloeistowwe wat in albei rifkomplekse aanwesig was. Georiënteerde kwartsare wat met mineralisasie geassosieer word, is vanuit beide die MRC en HR geanaliseer vir: (1) suurstofstabiele isotoop-handtekeninge; (2) vloeistofinsluitingstipes en vangtoestande bepaal deur mikrotermometrie-eksperimente; (3) gevolg deur 'n samestellende ontleding van vlugtige toestande in vloeistofinklusies deur middel van Raman-mikrospektroskopie. Die verwarring oor die samestelling en oorsprong van die goudmineraliserende vloeistof, sowel as die variasies in

verandering binne die MRC en HR, sal hopelik beter verstaan word met die gegewens wat in hierdie studie aangebied word.

Afgesien van die gedeeltelike disseksie van die vloeistofgeochemie van die MRC en HR, is 'n hoofstuk van hierdie proefskrif gewy aan die nuut gevestigde laboratorium vir vloeistofinklusie in die departement Aardwetenskap van die Universiteit Stellenbosch. Huidige metodologieë vir 'n goed ontwikkelde studie vir vloeistofinsluiting is verouderd en versuim om die belangrikheid van die handhawing van strukturele oriëntasie in monsters te demonstreer, uitgebreide kartering van die populasie van die opname van vloeistowwe en die korrekte hantering van monsters tydens die vorming van mikrotermometrie-eksperimente. Hierdie kort, maar bondige laboratoriumhandleiding gee 'n deurslag oor hoe om mikrotermometrie-eksperimente op te stel en uit te voer deur gebruik te maak van die Linkam THMS600 verwarming- en vriesfase, asook 'n eenvoudige dog informatiewe metodologie oor die uitvoering van 'n vloeistofinsluitingstudie.

Table of Contents

List of Figures

List of Tables

List of Abbreviations

BGB - Barberton Greenstone Belt

BIF - Banded Iron Formation

BSD - Backscattered Electron Detector

CCD - charge-coupled device

EDXS - Electron Dispersive X-ray Spectrometer

EHT- Beam acceleration voltage

FE SEM - Resolution Field Emission Scanning Electron microscope

FI - Fluid Inclusion

FIA - Fluid Inclusion Assemblage

HR - Hope Reef

L - Liquid

LA-ICPMS - laser ablation inductively coupled mass spectrometry

MRC - Main Reef Complex

SEM-CL - Scanning Electron Microscope with cathodoluminescence

Tcm - Temperature of clathrate melting

Th - Temperature of total homogenization

Tm_{ice} - Temperature of ice melting

TTG - Tonalite-Trondjhemite-Granodiorite

V-Vapor

Chapter 1 : Introduction

1.1 Preface

Archean Greenstone Belts are found on almost every continent and harbor some of the world's largest gold deposits. These deposits share numerous structural, geochemical and mineralogical elements, however, there is no clear evidence as to how the abundance of gold formed on various continents in these Greenstone Belts. The Barberton Greenstone Belt (BGB) is not only one of the oldest and most studied Archean orogenic gold system, but it is also one of the main gold abundant locations in South Africa (Anhaeusser 1976a, 1976b, 1986; Altigani et al., 2016; Anhaeusser, 2019).

Structural kinematics provide a crucial role in fluid flow through shear zones as stated in many studies and models (Colvine, 1989; Groves et al., 1992; De Ronde et al., 1992; Goldfarb et al., 2005; Gloyn-Jones and Kisters, 2018, 2019). Other studies give structural overviews for the entire Barberton region that provide insight into the mechanisms that allowed for gold deposition (Dziggel et al., 2007; Dirks et al., 2009; Munyai et al., 2011; Dirks et al., 2013). Various phases of deformation are thought to be the gateways that allowed hydrothermal fluids to permeate through sheared lithologies (Dirks et al., 2009). These fluids are believed to be the leading cause for the high levels of mineralization found in the BGB. Although there is knowledge on some structural mechanisms that have resulted in gold mineralization, the geochemistry of the fluid during the time of gold emplacement remains highly enigmatic.

Quartz and quartz- carbonate veins, present throughout the Fairview Mine were examined to inspect, with greater depth, the fluid source. Understanding the type of fluid inclusions present is important for exploration purposes. Fluid inclusion studies by Hagemann and Cassidy, (2000) followed by others, consider the likelihood of multiple fluid pathways. These fluid pathways allowed various phases of hydrothermal fluids to percolate through fractures and vein networks, leading to the distribution of mineralization (Hagemann and Cassidy, 2000). This study will use an array of vein sets in both the Hope Reef Complex (HR) and Main-Reef Complex (MRC) from the Fairview Mine within the BGB, to locate differences in fluid inclusion and isotopic data for the studied area. This will help provide a better spatial understanding of the ore forming fluids when paired with the structural geology.

There is a strong association between gold mineralization and H_2O-CO_2 rich fluids (Kerrich, 1983; Roedder, 1984; Smith et al., 1984; Cameron and Hattori, 1987; Hagemann and Cassidy, 2000; Goldfarb and Groves, 2015). By determining the type of inclusions found in the vein sets in both the MRC and HR, better parameters can be set on the fluid geochemistry. This will, in turn, provide further information on how gold was emplaced in the BGB and additionally assist in understanding other gold-mineralized Greenstone Belts worldwide.

1.2 Research Aims

Numerous geochemical and fluid inclusion studies have been conducted in gold mines within the BGB (De Ronde et al., 1992; Vries and Touret, 2007; Farber et al., 2016) to name a few , however more confined fluid inclusion studies on mineralizing reefs are devoid in the Fairview mining district. The goal of this study is to inspect quartz and quartz-carbonate veins from the MRC and HR for fluid inclusions (FI) and fluid inclusion assemblages (FIA) to identify the types of FI present within each selected vein type. The samples of interest are those dominated by quartz, quartz-carbonate and zones of alteration associated with mineralized margins in the MRC and HR. Thin sections of selected samples were analyzed to initially determine the mineralogy, followed by mapping and identifying of FI and FIAs. Each FIA was extensively sketched and mapped to assist in understanding the FI phases and assemblages present.

In addition to petrographic analysis, heating/homogenization and freezing experiments were conducted in samples where visible FIs and FIAs were present. Microthermometry studies constitute for majority of the work, in efforts to determine what the trapping conditions were during the time of mineral formation. Fluid inclusions were also analyzed via micro- Raman spectroscopy in order to indicate molecules present within the liquid- vapor phases of the FI, as well as within the quartz host. Mineral zonation in host minerals were identified using scanning electron microscope with cathodoluminescence (SEM-CL). Present growth zones assisted with identifying primary versus secondary fluid inclusions within thin sections. Lastly, quartz samples were analyzed through $\delta^{18}O$ stable isotope to interpret whether fluids display magmatic, meteoric or metamorphic signatures. The compilation of these selected analytical techniques will be coupled with the structural analysis completed by (Gloyn-Jones and Kisters, 2018, 2019) of the MRC and HR to assist in finding the potential fluid source when compared to the overall structural regime present within the Fairview Mine. These structurally confined samples allow

for a more precise geochemical study and will hopefully set the stage for further comparative work within gold deposits in the BGB and worldwide.

Research questions:

I. What is the nature and source of the gold-forming fluids throughout the Main Reef Complex and Hope Reef within Fairview Mining district?
II. Does the fluid inclusion and isotopic data from the Main Reef Complex compare or contrast to the Hope Reef and what does this state about the mineralizing fluids?

1.3 Thesis Outline

This thesis is broken up into five chapters as followed:

Chapter 1: Introduction and background on the Barberton Greenstone Belt and other Archean orogenic gold deposits followed by the overall research aims and objective for this thesis.
Chapter 2: This chapter presents the structural evolution and gold mineralization within the BGB Archean hydrothermal fluids and background information on gold precipitation. The transporting mechanism and background on mining in the BGB is presented in the form of a literature review.
Chapter 3: A manuscript for publication into the Geofluids: Structural Controls on Basin- and

Crustal- Scale Fluid Flow and Resulting Mineral Reactions, special issue. This chapter is currently in the format for submission to the special issue Geofluids journal and will be submitted to the editors in December 2019. Publication date for this journal issue will be May 2020. This manuscript is based on the fluid inclusion and oxygen stable isotope analysis on the structurally confined Main Reef Complex and the Hope Reef Complex within the Fairview Mine in the Barberton mountain region, South Africa; All data and material from Chapter 3 were presented at the following conferences; Geocongress Conference, Johannesburg, 18th of July 2018; Society of Economic Geologists (SEG), Keystone Colorado, USA , 22-25th September 2018; DSI-NRF CIMERA Annual Colloquium Johannesburg, 13th November 2018 & 7th November 2019; Society for Geology Applied to Mineral Deposits (SGA) Glasgow Scotland, 27-30th August 2019. The extended abstract found in Appendix I was also published in the conference proceedings titled; Life with Ore Deposits on Earth-15th SGA Biennial Meeting 2019, Volume 2, pages (756-759).

Chapter 4: Instructional laboratory manual and methodology for the newly established microthermometry laboratory in the Earth Science Department at Stellenbosch University. This is an unconventional chapter for a master's thesis; however, it is critical for the development and usage of the new microthermometry laboratory. My previous experience working with fluid inclusions and the Linkam microthermometry stage has allowed me to share my knowledge in efforts to establish an operational fluid inclusion laboratory at Stellenbosch University for students, faculty and other researchers. In this chapter there is a step by step guide on how to set up and operate the Linkam THMS600 heating homogenization and freezing stage. There is also a suggested methodology on how to carry out a fluid inclusion studies.

Chapter 5: Concluding remarks on previously mentioned chapters

All data and analysis not incorporated in the bulk of the thesis are listed in the appendices following Chapter 5.

1.4 References

Altigani, M., Merkle, R. and Dixon, R., 2016. Geochemical identification of episodes of gold mineralisation in the Barberton Greenstone Belt, South Africa. Ore Geol. Rev. 75, 186-205.

Anhaeusser, C.R., 1976a. The nature and distribution of Archaean gold mineralization in Southern Africa. Miner. Sci. Eng. 8, 46–84.

Anhaeusser, C.R., 1976b. The geology of the Sheba hills area of the Barberton mountain land, South Africa, with particular reference to the Eureka syncline. Trans. Geol. Soc. South Africa.

Anhaeusser, C. R., 1986a. Archaean gold mineralization in the Barberton Mountain Land, 113-154. In: Anhaeusser, C. R. and Maske, S. eds. Mineral Deposits of Southern Africa, I. Geological Society of South Africa. 1020.

Anhaeusser, Carl. 2019. The geology and tectonic evolution of the northwest part of the Barberton Greenstone Belt, South Africa: A review. South African Journal of Geology. 10.25131/sajg.122.0033.

Cameron, E. M., Hattori K., 1987, Archean gold mineralization and oxidized hydrothermal fluids. Econ. Geol. 82 (5), 1177–1191. https://doi.org/10.2113/gsecongeo.82.5.1177

Colvine, A.C., Andrews, A.J., Cherry, M.E., Durocher, M.E., Fyon, A.J., Lavigne, M. J., MacDonald, A.J., Marmont, S., Poulsen, K.H., Springer, J.S., Troop, D.G., 1984. An integrated model for the origin of Archean lode gold deposits. Ontario Geol. Surv. Open file Rep. 5524, 98.

De Ronde, C.E.J., Spooner, E.T.C., De Wit, M.J., Bray, C.J., 1992. Shear zone-related, Au quartz vein deposits in the Barberton Greenstone Belt, South Africa: Field and petrographic characteristics, fluid properties and light stable isotope geochemistry. Econ. Geol. 87, 366–402.

Dirks, P.H.G.M., Charlesworth, E.G., Munyai, M.R., 2009. Cratonic extension and Archaean gold mineralisation in the Sheba-Fairview mine, Barberton greenstone belt, South Africa. South African J. Geol. 112, 291–316. https://doi.org/10.2113/gssajg.112.3-4.291

Dirks, P.H.G.M., Charlesworth, E.G., Munyai, M.R., Wormald, R., 2013. Stress analysis, post-orogenic extension and 3.01Ga gold mineralisation in the Barberton Greenstone Belt, South Africa. Precambrian Res. 226, 157–184. https://doi.org/10.1016/j.precamres.2012.12.007

Dziggel, A., Otto, A., Kisters, A.F.M., Meyer, F.M. 2007. Chapter 5.8 Tectono-Metamorphic Controls on Archean gold mineralization in the Barberton Greenstone Belt, South Africa: An Example from the New Consort Gold Mine. Dev. Precambrian Geol., 15, 699-727. https://doi.org/10.1016/s0166-2635(07)15058-1

Gloyn-Jones, J.N, Kisters, A.F.M., 2018. (in press). Ore-shoot formation in the Main Reef Complex of the Fairview Mine: multiphase gold mineralization during regional folding, Barberton greenstone belt, South Africa. Mineralium Deposita.

Gloyn-Jones, J.N, Kisters, A.F.M., 2019. Ore-shoot formation in the Main Reef Complex of the Fairview Mine—multiphase gold mineralization during regional folding, Barberton Greenstone Belt, South Africa. Mineralium Deposita. https://doi.org/10.1007/s00126-019-00865-9

Goldfarb, R.J., Groves, D.I., 2015. Orogenic gold: Common or evolving fluid and metal sources. Lithos 233, 2–26.

Goldfarb, R.J., Baker, T., Dube, B., Groves, D.I., Hart, C.J.R., Gosselin, P., 2005. Distribution, character, and genesis of gold deposits in metamorphic belts. Econ. Geol. 100th Anniv. 407–450.

Groves, D.I., Barley, M.E., Barnicoat, A.C., Cassidy, K.F., Fare, R.J., Hagemann, S.G., Ho, S.E., Hronsky, J.M.A., Mikucki, E.J., Mueller, A.G., McNaughton N.J., Perring, C.S., Ridley, J.R., Vearncombe, J.R., 1992. Sub-greenschist- to granulitehosted Archaean lode-gold deposits of the Yilgarn Craton: A depositional continuum from deep-sourced hydrothermal fluids in crustal-scale plumbing systems. In: Glover, J.E., Ho, S.E. _Eds.., The Archaean:

Terrains, Processes and Metallogeny. Proceedings of the Third International Archaean Symposium, Perth, 1990. Geol. Dep. Univ. Ext., Univ. West. Aust. Publ. 22, 325–338.

Hagemann, S.G., Cassidy, K.F., 2000. Archean orogenic lode gold deposits. Society of Economic Geologists, Reviews in Econ. Geol. 13, 9-68.

Kerrich, R., 1983. Geochemistry of gold deposits in the Abitibi greenstone belt Canadian Institute of Mining Special Paper 27, 75.

Munyai, M.R., Dirks, P.H.G.M., Charlesworth, E.G., 2011. Archaean gold mineralisation during post-orogenic extension in the New Consort gold mine, Barberton greenstone belt, South Africa. South African J. Geol. 114, 121–144. https://doi.org/10.2113/gssajg.114.2.121

Roedder, E., 1984. Fluid inclusions. Rev. Mineral. 12.

Smith, T. J., Cloke, P. L., and Kesler, S. E., 1984. Geochemistry of fluid inclusions from the McIntyre-Hollinger gold deposit, Timmins, Ontario, Canada: Econ. Geol., 79, 1265-1285.

Chapter 2 : Structural evolution and gold mineralization of the BGB

This chapter includes a brief literature review on the types of Archean hydrothermal fluids, gold deposition in worldwide Archean orogenic deposits, the mechanisms of transport and precipitation of gold and finally background information on the mining history and general locality of the BGB. This chapter will assist in setting the general scene for the chapters that follow. As such, there will be a slight overlap in the geologic background of the manuscript in Chapter 3 to that found in this chapter.

2.1 Archean hydrothermal fluids

There is a commonality in the chemical composition of mineralizing fluids in Archean orogenic gold systems seen throughout different locations worldwide (Goldfarb and Groves, 2015). Archean gold deposits are suggested to form over a large range of metamorphic conditions and at varying crustal depths (Mikucki, 1997). The dominate reoccurring similarity with all studied Archean orogenic lode gold deposits is the evidence that supports a low-moderate salinity, mixed aqueous-carbonic fluid that resulted in gold mineralization (Hagemann and Cassidy, 2000). These fluids, however, do not have the same capacity to transport other base metals as they do for gold.

Investigating fluid wall-rock interactions and alteration assemblages present within samples can better aid in understanding the fluid types that have flowed through the BGB and other Archean lode deposits. Most alteration assemblages show enrichment in K and CO_2 with an association to metals such as Au, Ag, As, B, Bi, Sb, Te and W (Hagemann and Cassidy, 2000). Although most fluid inclusion data at various Archean lode gold deposits show low-moderate aqueous-carbonic rich fluids, there is evidence for a variety of volatile compositions which can be present within liquid and/or vapor phases of fluid inclusions e.g., CO_2, CH_4, N_2 (De Ronde et al., 1992; Van Reenen et al., 1993; Hagemann and Cassidy, 2000; Vries and Touret, 2007).

2.1.1 Gold mineralization in Archean orogenic gold deposits

Archean orogenic gold bodies worldwide typically have complex histories due to multiple deformational phases and metamorphism events and many are still well preserved. These deposits are classified by the type of mineralization, which in most cases is referred to as epigenetic, and formed from the focusing of relatively uniform low to moderate salinity, aqueous-carbonic rich

fluids during late reactivation of volcano-sedimentary terranes (Hagemann and Cassidy, 2000; Goldfarb and Groves, 2015). The depositional environment of these deposits appears to be the biggest contrast amongst Archean lode gold deposits (Hagemann and Cassidy, 2000); many being associated with a convergent and/or collisional belt in an accretionary setting (Groves et al., 1998; Goldfarb et al., 2001; Goldfarb and Groves, 2015; Gloyn-Jones and Kisters, 2018). Orogenic lode deposits are more than often associated with cratonic margins or accreted orogens and are hosted by a multitude of second and third order fault systems (Groves et al., 1998; Goldfarb et al., 2001; Goldfarb and Groves, 2015.

Localized dilatancies in areas such as fold hinges, fold influenced fractures and/or lithological contacts are critical for allowing fluid flow and vein networks to form within orogenic deposits (Groves et al., 1998; Goldfarb et al., 2015; Gloyn-Jones and Kisters, 2018, 2019). Archean orogenic gold deposits are commonly found in ultramafic to mafic volcanic suites with intrusive bodies within and/or in the surrounding region (Colvine et al., 1984; Robert and Poulsen, 2001; Gloyn- Jones and Kisters, 2018). Mineralization in Archean gold deposits is syn to post peak metamorphism in the later stages of the host terranes tectonic evolution (Hagemann and Cassidy, 2000). The timing of worldwide Archean orogenic gold provinces is illustrated in Table 2.1.

Table 2.1: Compilation of referenced and summarized Archean orogenic gold deposits with highlighted province, and timing of deformation and mineralization (modified from Goldfarb et al., 2001).

Gold province	Host area	Districts (deposits)	Deformation age (Ma)	Granitoid ages (Ma)	Mineralization age (Ma)	Reference
Barberton G.B.	Kaapvaal craton	(Sheba, New Consort, Fairview, Agnes)	3230–3080	3490–3450, 3230, 3105, 2690	3126–3084	Anhaeusser (1986), de Ronde et al. (1991), de Ronde and de Wit (1994)
Northern Pilbara craton	Pilbara craton	(Mount York, Bamboo Creek, Marble Bar, Blue Spec	3340, 3200, 3000–2900	3520–3400, 3315–3270, 3100, 3000–2900	3430–3300, 3200, 3000–2900	Neumayr et al. (1998), Witt et al. (1998)
Pre-Dnieprovian block	Ukrainian shield	(Sergeevsk, Balka Zolotaya, Appolonovsk)	3000, 2750	3500–3100, 2970, 2800–2600	Middle Archean? 2900–2500	Kushev and Kornilov (1997), Koval et al. (1997)
Eastern Goldfields superterrane	Yilgarn craton	(Golden Mile, Norseman, Kambalda, Bronzewing, Sunrise Dam, Jundee)	2660–2640	2900–2630	2670–2660 2640–2620, 2600	Witt et al. (1998), Kent et al. (1996), Yeats et al. (1999)
Southern Cross superterrane	Yilgarn craton	(Marvel Loch, Transvaal)	2660–2650	2700–2620	2650–2620	same as above
West Yilgarn superterrane	Yilgarn craton	(Big Bell, Hill 50)	2900, 2660–2640	2900–2630	2640–2620	same as above
Southern Superior Province (mainly Abitibi G.B.)	Canadian shield	(McIntyre–Hollinger, Sigma–Lamaque, Hemlo(?), Dome, Kerr–Addison)	2710–2670	2720–2670	2720–2660, 2600	Robert (1990, 1996), Kerrich and Cassidy (1994), Polat and Kerrich (1999)
Slave Province	Canadian shield	Yellowknife (Con, Giant), Gordon Lake, Lupin(?)	> 2800, 2700–2600	2800, 2700–2580	2670–2656, 2585	Abraham et al. (1994), King and Helmstaedt (1997)
Greenstone belts of E. Dharwar block	Indian shield	Kolar (Champion, Mysore, Nandydroog, Oorgaum) Hutti, Ramagiri, Gadag	2630–2520	2750–2510	≥ 2550	Hamilton and Hodgson (1986), Balakrishnan et al. (1999), Radhakrishna and Curtis (1999), Chadwick et al. (2000)
Midlands, Harare–Shamva, and Odzi–Mutare greenstone belts	Zimbabwe craton	Kwekwe (Globe/Phoenix), Kadoma (Cam/Motor), (Freda–Rebecca, Shamva, Rezende, Redwing)	2710–2620	2680–2580	2670–2650, 2618–2604, 2413(?)	Herrington (1995), Darbyshire et al. (1996), Vinyu et al. (1996), Schmidt-Mumm et al. (1994), Oberthur et al. (2000)
Limpopo belt	Between Kaapvaal and Zimbabwe cratons	(Renco)	2700–2600, 2550–2530	2720–2550, 2400	2570	Kisters et al. (1998), Kolb et al. (2000)
Lake Victoria goldfields	Tanzania craton	Geita (Bulyanhulu, Buhemba, Macalder)	2750–2530	2680, 2580–2570, 2530, 1870	< 2644, 2568–2534	Borg (1994), Walraven et al. (1994), Pinna et al. (1999)
Rio das Velhas greenstone belt	S. Sao Francisco craton	Quadrilatero Ferrifero (Cuiaba, Morro Velho, Raposos, Sao Bento, Santana)	2780–2770, 2150–1800, ca. 600	2780–2770, 2720–2700, 2600	2710–2580, 1830, ca. 600	Chauvet et al. (1994), Olivo et al. (1996), Lobato et al. (2001)
South Pass greenstone belt	Wyoming province	Sweetwater (Miners Delight, Carissa)	2800, 2630–2550	2800, 2670, 2630, 2550	2800	Bayley et al. (1973), Wilks and Harper (1997)
Karelian craton	Fennoscandian shield	Ilomantsi (Kelokorpi, Kuittila, Korvilansuo, Muurinsuo, Ramepuro), Kuhmo (Lokkiluoto)	2750–2720	2840, 2750–2690	2740–2690, 2607	Sorjonen-Ward et al. (1997), Stein et al. (1998), Eilu (1999)

2.1.2 Gold precipitation and mechanisms of transport

Modern day thermodynamic calculations on the conditions of Archean hydrothermal fluids that mineralize gold provide estimations as to which ligands complex with gold (Mikucki, 1997). The inability of gold to be complexed and transported in water makes it reliant on complexes such as chloride (Cl^-) and bisulfide that are found in hydrothermal fluids. The fluids that are responsible for the mineralization of gold in these systems are dominantly hydrothermal in origin but vary in terms of P-T space. For instance, epithermal deposit fluids are almost ambient, whereas other magmatic and metamorphic mineralizing fluids types can be rich in volatiles (e.g., CO_2, CH_4, H_2S) and have temperatures from 250-350˚C (Lui et al., 2014).

2.1.3 Mining in the Barberton Gold District

There are over 300 deposits within the BGB, but Sheba/Fairview Mines stand apart from the rest (Anhaeusser, 1986a; Agangi et al., 2014) due to the large tonnage of ore that have been produced. Since 1883, over 345t of Au have been produced from the Barberton region with majority of production coming from Sheba (123.7t) and Fairview (63.4t) (Dirks et al., 2009; Agangi et al., 2014). The overall gold production for the three main mines in the Barberton area, Sheba, Fairview and New Consort, is roughly 2.9 tons annually (Pan African Resources, 2015; Altigani et al., 2016).

In the northern portion of the BGB, near the contact between the Kaap Valley Pluton, deposits are dominantly hosted within greenschist facies lithologies, in forming conditions estimated around 300˚C and 1-4kbar (De Ronde et al., 1992; Agangi et al., 2014). Sheba and Fairview are believed to have formed at greater temperatures based off interpretations from geothermometry results of alteration assemblages (Dziggel et al., 2006; Otto et al., 2007; Agangi et al., 2014).

Sheba/Fairview hosts gold mineralization in a variety of styles however, two styles particularly important include: 1) quartz veins in quartzite from the Moodie's Group and 2) rich disseminated sulphide ore zones within shale and greywacke of the Fig Tree Group (Dirks et al., 2009). This nonuniform localization of gold is seen not only in Sheba/Fairview, but in all BGB mines. A large factor for gold centralized at Sheba/Fairview is thought to exist due to the presence of the Sheba shear zone (Dirks et al., 2009).

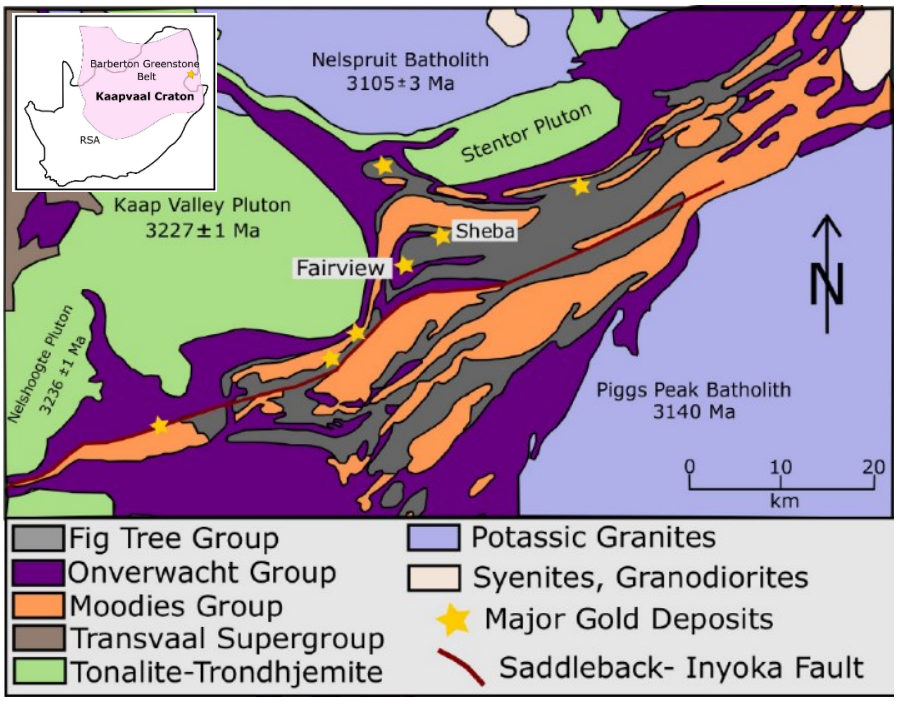

Figure 2.1: Regional geologic map of the Barberton Greenstone belt, illustrating the localities of major gold deposits, stratigraphic suites, and intrusive bodies (modified from Anhaeusser et al., 1981; Dirks et al., 2013; Agangi et al., 2014; Gloyn-Jon Jones and Kisters, 2018, 2019)

2.2 Structural evolution of the BGB

2.2.1 Geologic background

The Fairview gold mine is located within the hanging wall of the Sheba Fault, which follows a NE-E arcuate trend and dips steeply to the east, see Figure 2.1, (Gloyn-Jones and Kisters, 2018). The Sheba Fault is an N-W verging thrust fault that separates both the Ulundi and Eureka Synclines, coring the rocks of the Fig Tree and Moodie's Groups (Ramsay, 1963; Anhaeusser, 1976a, 1976b; Wigget et al., 1986; Lowe and Byerly, 2007; Barberton Mines, 2013; Agangi et al., 2014; Gloyn-Jones and Kisters, 2018, 2019). To the north, both the Eureka and Ulundi Synclines are bounded by the Kaap Valley Tonalite (3227 Ma) in the NW-SW, the Stentor Pluton (3300-3105 Ma) in the NE, as well as the Nelspruit batholith (3106 Ma) in the NE (Viljoen and Viljoen, 1969; Anhaeusser et al., 1981; De Ronde and De Wit, 1994; Kamo and Davis, 1994; Lowe and Byerly, 2007; Gloyn- Jones and Kisters, 2018, 2019).

Portions of the BGB that were subjected to NW-SE shortening are dominated by upright folds (F3a) trending NE-SW (De Ronde and De Wit, 1994; Gloyn- Jones and Kisters, 2018, 2019).

Through further structural analysis (e.g. Ramsey, 1963; Anhaeusser, 1963, 1976b; De Wit et al., 1987; Lowe et al., 1999; Lowe and Byerly, 2007) of the BGB it is evident that these folds have undergone a refolding event resulting in a NW-SE trending axial plane (F3b) (Anhaeusser,1963, 1976b; Gloyn- Jones and Kisters, 2018, 2019). The doubly folded Ulundi Syncline is moderately plunging W-SW, while the Eureka Syncline on the other hand plunges steeply W-S (Gloyn-Jones and Kisters, 2018, 2019). The Lily fault constrains the Eureka Syncline to the north, while the Ulundi Syncline is bounded by the Barbrook fault to the S (Agangi et al., 2014).

2.2.2 Stratigraphy/Age

The BGB is constructed of three main stratigraphic units which include, starting with the base and moving upward: (1) The Onverwacht Group (3550-3270 Ma), composed of mostly mafic and ultramafic volcanic lithologies, interbedded with thinly layered chert and felsic volcanics; (2) the Fig Tree Group (3260 - 3225 Ma), consisting of turbiditic greywackes, chert, mudstone, shale, banded iron formations and some volcaniclastic rocks; (3) the Moodie's Group (3225-3215 Ma), mainly clastic sedimentary rocks, sub greywacke, quartzose, and feldspathic sandstones (De Ronde et al., 1992; Lowe and Byerly, 1999; Lowe and Byerly, 2007; Agangi et al., 2014).

The BGB is divided into tectonic domains with varying stratigraphy, age, deformation and depositional events. Structural studies indicate the BGB is a succession of various repeating stratigraphic units that are fault bounded (De Ronde et al., 1992). The Inyoka- Saddleback fault, a 3.23 Ga suture zone, divided the rocks in all three stratigraphic groups (Dirks et al., 2009). In the Onverwacht Group the rocks to the north of the Inyoka fault are much thinner and younger than those in the south of the fault (Dirks et al., 2009). Within the Fig Tree Group, the southern facies consist of shallow marine sediments and greywacke sandstones while the north of the fault present deep water clastic facies; the Moodies Group rocks are coarser toward the south of the fault and finer to the north (De Ronde et al., 1992; Hofmann, 2005; Dirks et al., 2009).

2.2.3 Structural Kinematics

The entire Sheba/Fairview Mine district is dominated by two synforms, i.e. the Eureka and Ulundi Synclines (Dirks et al., 2009). Along the central-southern part of the Eureka and Ulundi Synclines sits the Fairview Mine (Otto et al., 2007). These two major synformal structures are separated by the Sheba Fault and bounded by both the Lily Fault to the north and the Barbrook

fault to the south (Otto et al., 2007; Dziggel et al., 2007; Altigani et al., 2016). Over time, the Eureka and Ulundi Synclines were refolded leading to the multitude of quartz-carbonate veins seen throughout many of the mines in the BGB (Dziggel et al., 2007). The increase in structural porosity through these less competent rocks allowed for the abundant gold endowment that is preserved in the numerous vein sets within the Fairview Mine (Hofmann and Harris, 2008; Altigani et al., 2016).

Both the Ulundi and Eureka Synclines vary in structural orientation. The Sheba Fault, which acts as a catalyst for most deformational events within the Fairview mining district is made up of various sheared and regressed serpentinites, talc- carbonate schists and cherts, all of which are found within the Weltevreden Formation and are fixed between both the Ulundi and Eureka synforms (Ramsay, 1963; Byerly et al., 1996; Lowe and Byerly, 1999; Lowe and Byerly, 2007; Gloyn- Jones and Kisters, 2018). Frequent periods of faulting and deformation aided in the development of mineralized brittle- ductile shear zones termed "reefs" which are present throughout the Fairview Mine and BGB (Gloyn-Jones and Kisters, 2018, 2019). Two reefs particularly interesting are the Main Reef Complex and the Hope Reef found within the Fairview Mine.

2.2.4 Deformation

There have been several deformation events: the earliest being D_o (3.49-3.45 Ga), which represents alteration and extension near oceanic volcanic spreading regions; followed by D_1 (3.45-3.42 Ga) where thermo tectonic events emplaced ophiolite allochatons and TTG plutons; then D_2 (3.26 -3.23 Ga), a second period of subduction paired with inter- arc deformation and culmination by a separate arc system and sutured by the Inyoka-Saddleback fault (De Ronde et al., 1994; Dirks et al., 2009; Agangi et al., 2014). Next is early D_3 (3.23-3.13Ga) which marks periods of convergence, accretion and transpressional events, followed by the formation of strike parallel faulting which are associated with the start of gold mineralization; late D_3 (3126 +/-26 Ma 3084 +/-18 Ma) transpressional events shifted to transtensional events and gold mineralization peaks (De Ronde et al., 1992; De Ronde et al., 1994; Dirks et al., 2009; Agangi et al., 2014; Gloyn-Jones and Kisters, 2018). The ranges in age for gold mineralization are due to early dating results of a single zircon by De Ronde et al., 1991, followed by the dating of hydrothermal rutile. With further studies, recent ages have been given to the mineralization event, between ca. 3030-3040 Ma

(Dziggel et al., 2010). The final phase of deformation, D_4 (3.1Ga) is a series of extensional collapse within the region followed by the intrusion of potassic granite batholiths, which jumpstarted cratonization in the area (Dirks et al., 2009; Agangi et al., 2014).

Although gold mineralization is at its peak in the third stage of deformation, it seems all deformational periods (D_1-D_4) played crucial roles to the emplacement of the gold throughout the BGB. As mentioned, these shearing mechanisms allowed for fractures in the lithologies which permeated fluids upward, leaving behind pockets of gold. The multitude of structural alterations has led to the economically rich deposits found throughout the BGB and highlights why this is a particularly interesting study area.

2.2.5 Main Reef Complex (MRC)

The MRC is located along the Birthday No. 2 Anticline near the SE limb. At Fairview Mine, the MRC main ore shoot is closer to the SE plunging SW hinge of the Birthday No. 2. Anticline (Gloyn-Jones and Kisters, 2019). The wall rocks of the MRC are mainly composed of greywacke (1.5m wide) and graphitic shale (5-25m wide) units from the Fig Tree Group which overlay ultramafics and chert of the Weltevreden Formation (Gloyn-Jones and Kisters, 2019). Within the footwall of the MRC in the Weltevreden Formation contains talc-carbonate schist, serpentinite, and few banded cherts. Along foliation planes are numerous series of folded black quartz veins and quartz breccias. It is the shale and greywacke units of the Fig Tree Group that contain economic mineralized gold grades (Gloyn-Jones and Kisters, 2019). Units of the lower Fig Tree shales outside of the MRC have little to no graphite present, unlike the shale within the MRC where there is significant graphitic material throughout the sheared planes. This graphitic material within the MRC shales hosts large amounts of sulphides.

The main portion of the ore shot at the MRC is dominated by graphitic carbonate alteration and sulphides, particularly pyrite, and arsenopyrite. Gold grades vary throughout the reef, but average between >40-60g/t (Roelf Le Roux, Barberton Mines, pers. Comm., March 2018; Gloyn-Jones and Kisters, 2019). Areas of the MRC that are steeply dipping have been sheared out, leaving a truncation within the stratigraphy of the wall rock adjacent to the contact between the Weltevreden Formation and Fig Tree Group (Gloyn-Jones and Kisters, 2019). These lithological contacts with the Weltevreden Formation and the Fig Tree provide evidence for the present high

strain fabrics and shearing. The contacts between the Weltevreden Formation and the Fig Tree group are sheared with evidence of this shearing seen by the high-strain fabrics and truncation of the units. This contact of sheared lithologies is the controlling structure of the MRC. It is this contact and high level of shearing that controls the MRC structure. This altered wall rock feature is where economic grades are being mined.

High strain (S_1) fabrics of bedding-parallel foliation can be seen within the graphitic shale units. This S_1 is parallel to the contact between the Fig Tree Group and Weltevreden Formation and dips at a steep 50-60˚ to the E-SE (Gloyn-Jones and Kisters, 2019). According to (Gloyn-Jones and Kisters, 2019) the S_1 fabric is indicated by the preferred orientation of quartz and carbonate grains within the matrix of the shale units. Graphite bearing seams form parallel to the S_1 fabric within the shales.

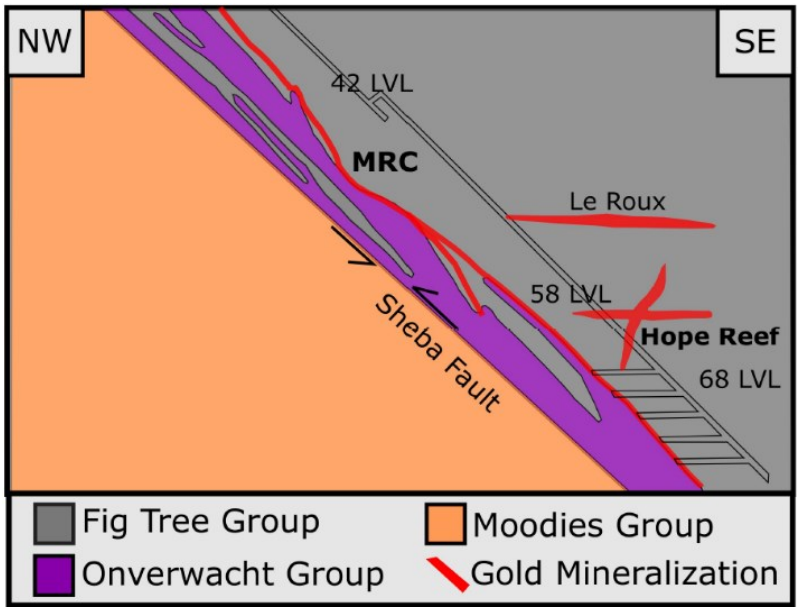

Figure 2.2: Cross sectional view of Fairview Mines with both the Ulundi and Eureka synclines. Lithological units and mineralized zones are also illustrated (modified from Barberton Mines, 2013; Gloyn-Jones and Kisters, 2018).

Some areas with S_1 fabrics have been deformed by both S_2 and S_3 foliations resulting in refolding and crenulation of the original S_1. High strain fabrics can also be seen within the deformation and localization of sulphides throughout the reef. There is a more dominant presence of sulphides within the graphitic shales and greywacke units unlike the sub economic gold grades and sulphides seen in the rocks of the Weltevreden Formation (Gloyn-Jones and Kisters, 2019).

2.2.6 Hope Reef Complex (HR)

Structural analysis from (Gloyn-Jones and Kisters, 2018) was done within the Fairview Mine of the Hope Reef Complex at level 58. This level of the mine is the shallow portion of the reef and shows high-grade mineralization with associated quartz veining, sulphide mineralization, and wall-rock alteration, all bounded by a SE shallow dipping brittle-ductile shear zone system (Gloyn- Jones and Kisters, 2018). The HR is situated in the lower portion of the Sheba Formation, above the Sheba Fault and Main Reef Complex, composed of mostly a greywacke package (Gloyn-Jones and Kisters, 2018). The entirety of the HR is made up of both shallow and steeply dipping mineralized zones that are confined to the greywacke units of the Fig Tree Group (Gloyn-Jones and Kisters, 2018). The shallow portion of the reef, however, is where majority of quartz veining and mineralization was recorded and sampled.

The following planer fabrics help delineate the mechanisms that caused such structural alteration in the HR. The oldest planar fabric in the HR is bedding (S_0), present within Fig Tree metasediments and showing deflection with rotation into the shallow mineralized body of the HR (Gloyn- Jones and Kisters, 2018). There is a partial sub-parallel foliation (S_1) seen by the preferred mineralization direction of the surrounding sericite and chlorite. Following this foliation is (S_2), which is SE dipping and parallel to the shear direction and is indicated by the imbrication of quartz vein fragments as well as the altered wallrock. Majority of gold is isolated to the shallow portions of the reef with minor mineralization present in the steep regions. Kinematic indicators such as microfaults and S-C fabrics provide evidence to a NW sense of motion along regions of low angle central shear zones (Gloyn- Jones and Kisters, 2018). These kinematic markers suggest that the HR is a low angled thrust zone. Aside from a NW indication of motion, quartz carbonate veins with components of sulphides point to a SE, normal movement, however, this is less prominent than the NW shearing.

2.2.7 Quartz Veining

Quartz and quartz-carbonate veins are categorized according to their location within the MRC. The first group of veins have been deformed and overprinted by progressive deformational events. These veins are located within or adjacent to the central reef, whereas the second group of veins are seen outside the central reef and within the wall rock. This proximal set of veins show less deformation and, in some areas, preserve the primary vein textures, i.e. syntaxial growth zones and compositional zonation (Gloyn- Jones and Kisters, 2018).

The quartz veining and mineralization of the shallow Hope Reef complex can be seen in four different structural fashions. The first, as NE trending, semi deformed quartz veins that are adjacent to the central fault; followed by fault zone foliation parallel, sheared out quartz stringers; then as splays of quartz sulphide veinlets from the central fault and finally as quartz wall-rock breccias, which are bounded between fault planes in NE- trending discontinuous antiformal stacks (Gloyn- Jones and Kisters, 2018). Examples of quartz veins in the Hope Reef can be seen in Figure

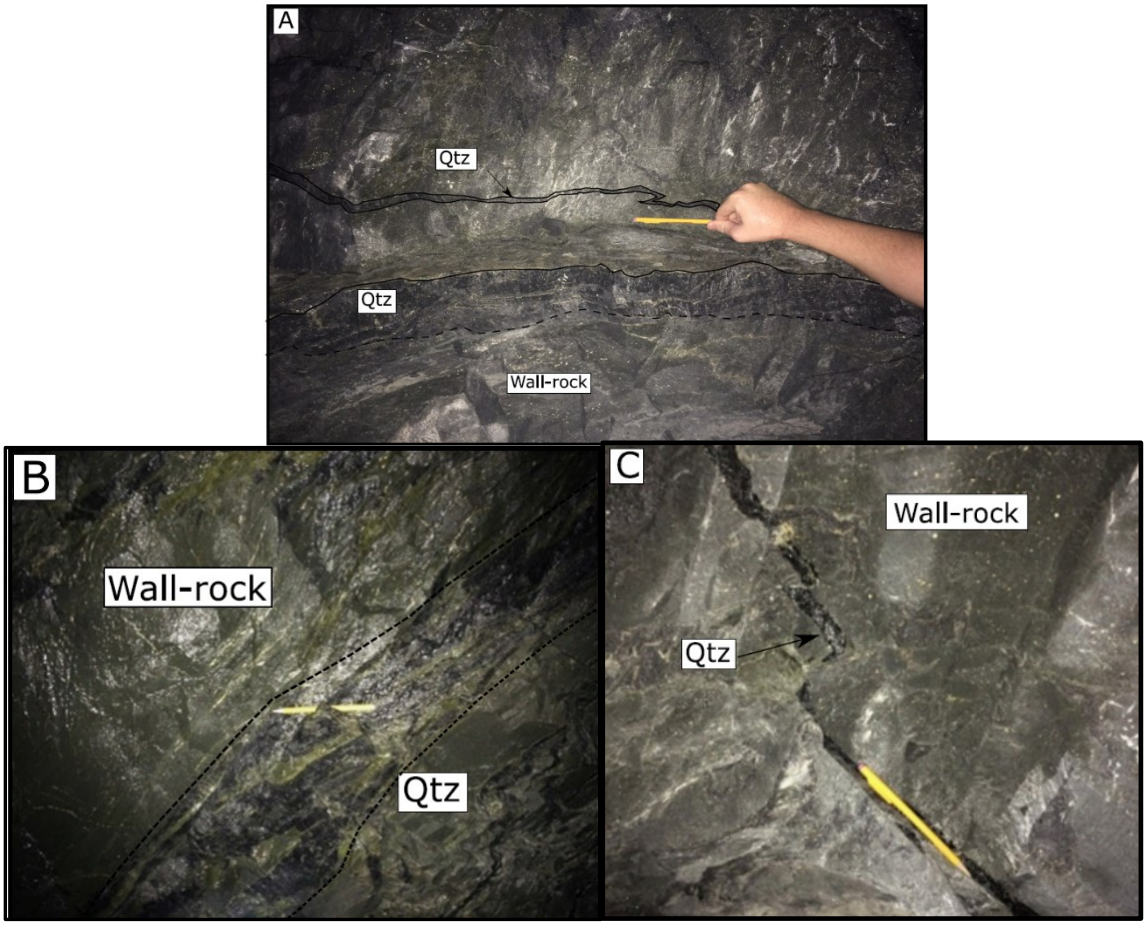

Figure 2.3: A. Sheared- extensional pinnate vein containing sulphide, surrounded by proximal alteration halos. B. Deformed sheared veins within the HRC showing laminated quartz/ quartz-carbonate veins at the bottom and folded shear veins on the top. C. Quartz veins showing "stepped" pattern within the hanging wall of HRC.

2.3.Quartz veining in the MRC is displayed as low angle- fault-filled or foliation parallel as hybrid extensional sheared pinnate veins or as sulphide rich quartz carbonate veins

Like the HR quartz veins in the MRC are black, some containing carbonate intergrowths and sulphide aggregates. MRC extensional veins follow a NE striking dextral strike slip motion whereas low angle fault-filled veins strike N-NE in relation to S2 foliation of the central shear

zone (Gloyn- Jones and Kisters, 2019). A list of samples and the respective orientation can be seen in Table 3.1.

2.3 Gold Mineralization

The bulk of the gold mineralization is hosted within the Fig Tree and Moodie's Group; however, gold is also disseminated throughout other lithologies in the BGB (Dziggel et al., 2007; Dirks et al., 2013; Altigani et al., 2016). The variable amounts of gold mineralization in the BGB are either the result of multiple or protracted fluid flow events, in both Sheba and Fairview Mines (Bierlein and Maher, 2001; Altigani et al., 2016).

In the MRC of the Fairview Mine, higher gold grades are spatially associated with shale units of the Onverwacht Group (Gloyn- Jones and Kisters, 2018). There are two distinct forms of mineralization within the MRC; sulphide mineralization that is associated with blackish-grey quartz carbonate veins and mineralization of similar sulphides dominantly in the surrounding shale wall-rocks (Gloyn-Jones and Kisters, 2018).

Gold mineralization within the Sheba/Fairview Mines formed as a result of fracture systems during late D_3 deformation with the structural porosity and quartz- carbonate veining showing the greatest association to gold mineralization (Dziggel et al., 2007, 2010; Dirks et al., 2013; Altigani et al., 2016). The ideal pressure- temperature conditions for fluids to transport gold are of ca. 200-650^{o}C and 1-5 kbar, with low salinity and high CO_2 contents (Altigani et al., 2016). According to Dziggel et al., 2007; Pettke et al., 1998, these auriferous mineralizing fluids generated from metamorphic reactions in the mid-lower crust and form from devolatilization of metamorphic fluids; Hofmann, 2005 and Vanko, 1986, on the other hand, suggest the fluids are dominated by a magmatic signature.

Most of the mineralization of gold in the Fairview district is dominantly presumed to be in the form of sulphide reefs and quartz reefs (Altigani et al., 2016; Gloyn-Jones and Kisters, 2018). After the major folding events, tangential shearing in the Fig Tree greywackes and shales allowed for sulphide reefs to be disseminated (Dziggel et al., 2007; Altigani et al., 2016). These sulphide reefs can be seen extending roughly 500m along strike with widths ranging 2cm to 2m (Otto et al., 2007; Dziggel et al., 2007; Altigani et al., 2016).

2.4 Alteration

Almost all the BGB has been altered in some aspect at temperatures greater than 300°C, however there are still numerous original structures and fabrics that are visible on a finer scale (Xie et al., 1997; Cloete, 1999; Tice et al., 2004; Lowe and Byerly, 2007). Most of the refractory primary minerals have been overprinted due to widespread metasomatism across the BGB, leaving behind only detrital and early diagenetic minerals such as chromite, zircon, apatite, rutile, coarse quartz, carbonates, iron oxides, and barite (Lowe and Byerly, 2007). This extensive period of metasomatism shows whole rock K-Ar geochron ages like that of serpentinites in the lower part of the Onverwacht Group, about 3300 Ma (De Ronde et al., 1992). Igneous lithics, such as peridotite-rich komatiites, have been altered into various mosaics of serpentine, magnetite, tremolite and chlorite while preserving the original structure and textures (Lowe and Byerly, 2007). The tops of volcanic sequences are marked by intense metasomatic alteration of komatiitic and basalt flows and usually underlie proximal chert units (Lowe and Byerly, 2007).

Complex quartz veins cut through the remaining Cr- rich sericite dominated mineralogy (Lowe and Byerly, 2007). It is interpreted that these various altered lithologic zones are sea floor flow-top alteration zones (Lowe and Byerly, 1986a; Lowe et al., 1999), hydrothermal alteration zones (Dunchac and Hanor, 1987; Hanor and Duchac, 1990), or shear zones from major thrust faults (De Wit, 1982, 1983; Lowe and Byerly, 2007).

On a finer scale within the Fairview Mine in the Hope Reef complex there is significant chlorite-sericite-carbonate hydrothermal alteration. There is distinct greenish-alteration contrasting surrounding sulphide mineralization within the Fig Tree greywackes, refer to Figure 2.4 (Gloyn-Jones and Kisters, 2018). This trend of alteration extends almost 4m from the HR into the surrounding lithics, clearly distinguishing the proximal and distal alteration assemblages (Gloyn-Jones and Kisters, 2018). Distal alteration zones present a dull-greenish color within the dark gray Fig Tree rocks indicating the level of chlorite- sericite and carbonate occurrences. There are carbonate “spots” seen around halo zones of quartz veins that resemble a peppered texture, becoming finer and fading with an increase of distance from the quartz veins (Gloyn-Jones and Kisters, 2018).

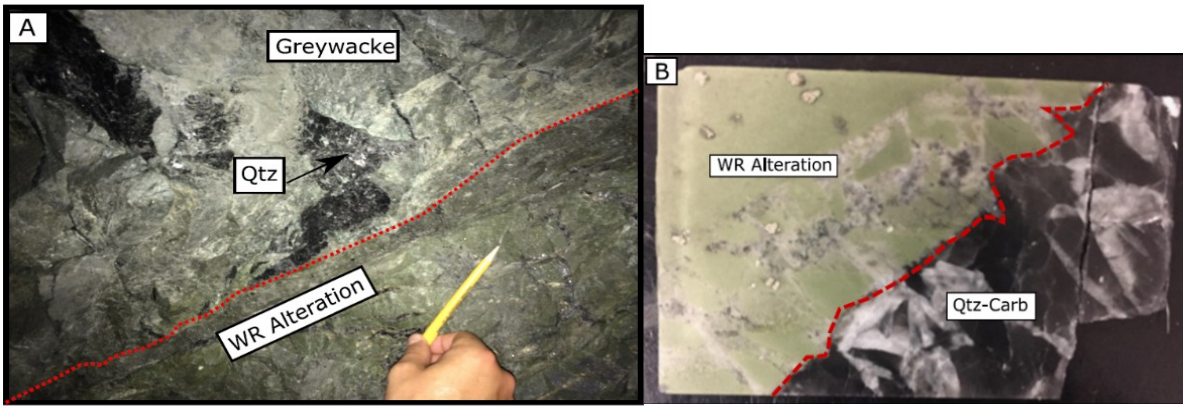

Figure 2.4: A. Alteration boundary within Hope Reef complex. Chlorite-sericite-rich proximal alteration along contact (red dashed line) with greywacke wall rock. Inside the wall-rock is a splayed pinnate quartz vein. B. Thin section used for microthermometry analysis shows a contact (red dashed line) between a chlorite-sericite rich wall-rock to black quartz and bladed white carbonate veins.

Closer to the reef, the intensity of alteration becomes more noticeable. Proximal alteration portrays more pristine carbonate spots and stringers that delineate the S_1 type foliation in the Fig Tree greywackes (Gloyn-Jones and Kisters, 2018). Coarse grained euhedral pyrite replaces the carbonate spots and stringers in some areas of the wall rock (Gloyn-Jones and Kisters, 2018). Central shears are surrounded by bright green halos about two meters wide, indicating a more pervasive chlorite- sericite- carbonate alteration with a spatial association to the close sulphide mineralization (Gloyn-Jones and Kisters, 2018).

In the Main Reef Complex there are two visible forms of alteration that are associated to the shear zones within the complex. First is a graphite alteration that is believed to have developed in proximal areas to the surrounding chert units or as a result of the abundant shale units in this part of the reef (Gloyn-Jones and Kisters, 2019). The graphite in these rocks is situated in the S_1 foliation of the hanging wall, indicating it either predates the early development of the S_1 fabrics and MRC shear zoning or it was introduced after the shear zones had formed (Gloyn-Jones and Kisters, 2018).

Carbonate alteration is the second type to affect MRC, in both the shales and greywackes of the Fig Tree Group (Gloyn-Jones and Kisters, 2018). Like the graphitic alteration this too formed within MRC shear zones. The influx in the wall rocks by this carbonization is likely associated with early to coeval shear foliation development and quartz-carbonate veining (Gloyn-Jones and Kisters, 2018).

Alteration halos around fracture zones containing gold can be used as an exploration indicator for defining ore zones underground and at surface (Schouwstra, 1995). Major mineralogical changes of the wall rock are sulphidation, replacement of chlorite by muscovite, hydrolysis of feldspar and carbonization, all of which are within a vein material or disseminated throughout the wall rock (Schouwstra, 1995). An increase in S, As, K_2O, Rb, and CO_2 followed by a decrease of Na_2O and MgO are the major characteristics for chemical alteration within the Sheba Mine wall rocks (Schouwstra, 1995). Geochemical indicators of alteration show that gold concentrations are erratic, even within gold bearing fracture zones.

2.5 References

Agangi, A., Hofmann, A. and Przybylowicz, W., 2014. Trace element zoning of sulfides and quartz at Sheba and Fairview gold mines: Clues to Mesoarchean mineralisation in the Barberton Greenstone Belt, South Africa. Ore Geol. Rev. 56, 94-114. https://doi.org/10.1016/j.oregeorev.2013.08.016

Altigani, M., Merkle, R. and Dixon, R., 2016. Geochemical identification of episodes of gold mineralisation in the Barberton Greenstone Belt, South Africa. Ore Geol. Rev. 75, 186-205.

Anhaeusser, C.R., 1963. The geology of the Lily syncline and position of the Eureka syncline between Sheba siding and Louw's Creek station, Barberton Mountain Land, M.Sc. thesis (unpubl.). Univ. Witwatersrand, Johannesburg. 150.

Anhaeusser, C.R., 1976a. The nature and distribution of Archaean gold mineralization in Southern Africa. Miner. Sci. Eng. 8, 46–84.

Anhaeusser, C.R., 1976b. The geology of the Sheba hills area of the Barberton mountain land, South Africa, with particular reference to the Eureka syncline. Trans. Geol. Soc. South Africa.

Anhaeusser, C. R., 1986a. Archaean gold mineralization in the Barberton Mountain Land, 113-154. In: Anhaeusser, C. R. and Maske, S. eds. Mineral Deposits of Southern Africa, I. Geological Society of South Africa. 1020.

Anhaeusser, C.R., Robb, L.J., Viljoen, M.J., 1981. Provisional geological map of the Barberton Greenstone Belt and surrounding terrane, eastern Transvaal and Swaziland scale 1: 125,000. Geol. Soc. South Africa.

Barberton Mines (Pty), 2013. Mineral Resource and Mineral Reserve Report 2017.

Bierlein F. P., Maher S., 2001. Orogenic disseminated gold in Phanerozoic fold belts: examples from Victoria, Australia and elsewhere. Ore Geol Rev. 18, 11.

Byerly, G., Kröner, A., Lowe, D., Todt, W., Walsh, M., 1996. Prolonged magmatism and time constraints for sediment deposition in the early Archean Barberton greenstone belt: evidence from the Upper Onverwacht and Fig Tree groups. Precambrian Res. 78(1-3), 125-138.

Cloete, M., 1999. Aspects of volcanism and metamorphism of the Onverwacht Group lavas in the south-western portion of the Barberton greenstone belt. Geol. Surv. South Africa Mem. 84, 232.

Colvine, A.C., Andrews, A.J., Cherry, M.E., Durocher, M.E., Fyon, A.J., Lavigne, M. J., MacDonald, A.J., Marmont, S., Poulsen, K.H., Springer, J.S., Troop, D.G., 1984. An integrated model for the origin of Archean lode gold deposits. Ontario Geol. Surv. Open file Rep. 5524, 98.

De Ronde, C.E.J., de Wit, M.J., 1994. Tectonic history of the Barberton greenstone belt, South Africa: 490 million years of Archean crustal evolution. Tectonics, 13(4): 983–1005.

De Ronde, C.E.J., Spooner, E.T.C., De Wit, M.J., Bray, C.J., 1992. Shear zone-related, Au quartz vein deposits in the Barberton Greenstone Belt, South Africa: Field and petrographic characteristics, fluid properties and light stable isotope geochemistry. Econ. Geol. 87, 366–402.

De Vries, S.T., Touret, J.L.R., 2007. Early Archaean hydrothermal fluids; a study of inclusions from the similar to 3.4 Ga Buck Ridge Chert, Barberton Greenstone Belt, South Africa. Chem. Geol. 237 (3–4), 289–302.

De Wit, M. J., 1982. Gliding and overthrust nappe tectonics in the Barberton greenstone belt: Structural Geology. 4, 2.

De Wit, M.J., 1983. Notes on a preliminary 1:25,000 geological map of the southern part of the Barberton Greenstone Belt. In: Anhaeusser, C.R. (Ed.), Contributions to the Geology of the Barberton Mountain Land. Spec. Publ. Geol. Soc. South Africa, 185–187.

De Wit, M.J., Hart, R. A., Hart, R. J., 1987. The Jamestown Ophiolite Complex, Barberton mountain belt: a section through 3.5 Ga oceanic crust. Journal of African Earth Sciences (1983), 6(5): 681-730.

Dirks, P.H.G.M., Charlesworth, E.G., Munyai, M.R., 2009. Cratonic extension and Archaean gold mineralisation in the Sheba-Fairview mine, Barberton greenstone belt, South Africa. South African J. Geol. 112, 291–316.
https://doi.org/10.2113/gssajg.112.3-4.291

Dirks, P.H.G.M., Charlesworth, E.G., Munyai, M.R., Wormald, R., 2013. Stress analysis, post-orogenic extension and 3.01Ga gold mineralisation in the Barberton Greenstone Belt, South Africa. Precambrian Res. 226, 157–184.
https://doi.org/10.1016/j.precamres.2012.12.007

Dunchac, K. C., and Hanor, J.R., 1987. Origin and timing of the metasomatic silicification of an early archean komatiite sequence, barberton mountain land, South Africa. Precambrian Res. 37.2, 125-146.
https://doi.org/10.1016/0301-9268(87)90075-1

Dziggel, A., Otto, A., Kisters, A.F.M., Meyer, F.M. 2007. Chapter 5.8 Tectono-Metamorphic Controls on Archean gold mineralization in the Barberton Greenstone Belt, South Africa: An Example from the New Consort Gold Mine. Dev. Precambrian Geol., 15, 699-727.
https://doi.org/10.1016/s0166-2635(07)15058-1

Dziggel, A., Poujol, M., Otto, A., Kisters, A., Trieloff, M., Schwarz, W., Meyer, F., 2010. New U–Pb and 40Ar/39Ar ages from the northern margin of the Barberton greenstone belt, South Africa: Implications for the formation of Mesoarchaean gold deposits. Precambrian Res. 179(1-4), 206-220.
https://doi.org /10.1130/2006.2405.09

Dziggel, A., Stevens, G., Poujol, M., Armstrong, R., 2006. Contrasting source components of clastic metasedimentary rocks in the lowermost Formations of the Barberton greenstone belt. Special Paper of the Geol. Soc. of Am. 405, 157-172.

Gloyn-Jones, J.N., Kisters, A.F.M., 2018. (in press). Ore-shoot formation in the Main Reef Complex of the Fairview Mine: multiphase gold mineralization during regional folding, Barberton greenstone belt, South Africa. Mineralium Deposita.

Gloyn-Jones, J., Kisters, A., 2019. Ore-shoot formation in the Main Reef Complex of the Fairview Mine—multiphase gold mineralization during regional folding, Barberton Greenstone Belt, South Africa. Mineralium Deposita.
https://doi.org/10.1007/s00126-019-00865-9.

Goldfarb, R.J., Groves, D.I., 2015. Orogenic gold: Common or evolving fluid and metal sources. Lithos 233, 2–26.

Goldfarb, R.J., Groves, D.I., Gardoll, S., 2001. Orogenic gold and geologic time: A global synthesis. Ore Geol. Rev. 18, 1–75.

Groves, D.I., Goldfarb, R.J., Gebre-Mariam, M., Hagemann, S.G., Robert, F., 1998. Orogenic gold deposits: A proposed classification in the context of their crustal distribution and relationship to other gold deposit type. Ore Geol. Rev. 13, 7-27.

Hagemann, S.G., Cassidy, K.F., 2000. Archean orogenic lode gold deposits. Society of Economic Geologists, Reviews in Econ. Geol. 13, 9-68.

Hanor, J., Duchač, K., 1990. Isovolumetric Silicification of Early Archean Komatiites: Geochemical Mass Balances and Constraints on Origin. The Journal of Geology. 98(6), 863-877.

Hofmann, A., 2005. The geochemistry of sedimentary rocks from the Fig Tree Group, Barberton greenstone belt: Implications for tectonic, hydrothermal and surface processes during mid-Archaean times. Precambrian Res. 143(1–4), 23-49. https://doi.org/10.1016/j.precamres.2005.09.005.

Hofmann, A., Harris, C., 2008. Silica alteration zones in the Barberton greenstone belt: A window into subseafloor processes 3.5–3.3 Ga ago. Chem. Geol. 257(3–4), 221-239. https://doi.org/10.1016/j.chemgeo.2008.09.015.

Kamo, S.L., Davis, D.W., 1994. Reassessment of Archean crustal development in the Barberton Mountain Land, South Africa, based on U-Pb dating. Tectonics 13, 167-192. https://doi.org/https://doi.org/10.1029/93TC02254.

Liu, W., Etschmann, B., Testemale, D., Hazemann, J., Rempel, K., Müller, H., Brugger, J., 2014. Gold transport in hydrothermal fluids: Competition among the Cl−, Br−, HS− and NH3(aq) ligands. Chem. Geol. 376, 11-19. https://doi.org/10.1016/j.chemgeo.2014.03.012.

Lowe, D.R., and Byerly, G.R., 1999. Stratigraphy of the west-central part of the Barberton greenstone belt, South Africa, in Lowe, D.R., and Byerly, G.R., eds., Geological Evolution of the Barberton Greenstone Belt, South Africa: Geol. Soc. of Am. Special Paper 329, 1–36.

Lowe, D.R., Byerly, G.R., 2007. An Overview of the Geology of the Barberton Greenstone Belt and Vicinity: Implications for Early Crustal Development. Precambrian Geol. 15, 481-526.

Lowe, D.R., Byerly, G.R., Heubeck, C., 1999. Structural divisions and development of the 70 west-central part of the Barberton Greenstone Belt, South Africa. Geol. Soc. Am. Spec. Pap, 329, 37–82.

Mikucki, E., 1997. Hydrothermal transport and depositional processes in Archean lode-gold systems: A review. Ore Geol. Rev.13, 307-321.

Otto, A., Dziggel, A., Kisters, A. and Meyer, F., 2007. The New Consort Gold Mine, Barberton greenstone belt, South Africa: orogenic gold mineralization in a condensed metamorphic profile. Mineralium Deposita. 42(7), 715-735.

Pan African Resources, 2015. http://www.panafricanresources.com/operations-overview/barberton/ accessed on 2015-08-20.

Pettke, T., Diamond, LW, Kramers, JD., 1998. Mesothermal gold lodes in lodes in the north-western Alps: A review of genetic constraints from radiogenic isotopes. European Journal of Mineral. 12, 213-230.

Ramsay, J.G., 1963. Structural investigations in the Barberton Mountain Land, Eastern Transvaal. Trans. Geol. Soc. South Africa 66, 353–401.

Robert, F., Poulsen, K.H., 2001. Vein formation and deformation in greenstone gold deposits. Soc. Econ. Geol. Rev. 14, 111–155. https://doi.org/10.5382/Rev.14.05.

Schouwstra, R.P., 1995. Wall-rock alteration as a guide to gold-bearing fracture zones in the Zwartkoppie section, Sheba gold mine, South Africa. South Africa J. Geol. 98, 399–414.

Tice, M.M., Bostick, B.O., Lowe, D.R., 2004. Thermal history of the 3.5–3.2 Ga Onverwacht and Fig Tree Groups, Barberton Greenstone Belt, South Africa, inferred by Raman microscopy of carbonaceous material. Geology 32, 37–40.

Van Reenen, D.D., Du Toit, T., Hoernew, S., Roering, C., Smit, C.A., 1993. CO2-rish fluids and potassium metasomatism associated with deep crustal (granulite-facies) shear zones in the Limpopo Belt, South Africa. Abstr. USA.

Vanko, D.A., 1986. High-chlorine amphiboles from oceanic rocks: Product of highly saline hydrothermal fluids. American Mineralogist, 71, 51–59.

Viljoen, M.J., Viljoen, R.P., 1969a. An introduction to the geology of the Barberton granite-greenstone terrain. Geol. Soc. South Africa Spec. Publ. 2, 9-28.

Wiggett, B.S.C., Brink, W.C.J., Vorster, M.A., 1986. The Fairview gold mine, Barberton greenstone belt, in C.R. Anhaeusser and S. Maske (Eds.). Miner. Depos. South. Africa 1, 169–179.

Xie, X., Byerly, G.R., Ferrel, R.E., 1997. IIb trioctahedral chlorite from the Barberton Greenstone Belt: crystal structure and rock composition constraints with implications for geothermometry. Contrib. Mineral. Petrol. 126, 275–291.

Chapter 3 : Fluid evolution in an evolving orogenic gold mineralizing system: case study from Fairview mining complex, Barberton Greenstone Belt, South Africa

This chapter presents a manuscript prepared for submission to the special issue of Geofluids: Structural Controls on Basin- and Crustal- Scale Fluid Flow and Resulting Mineral Reactions. This manuscript will be submitted to the editors in December 2019. Publication of this journal will be in May 2020. The paper provides a brief background on the geologic setting and overall structural kinematics that set the stage for this geochemical- isotopic- fluid inclusion study. There are structural and lithological differences seen within the MRC and HR that are further investigated along with the fluids that may have been responsible for the different mineralization grade in these two reef complexes.

Collecting and preparation of samples, microthermometry experiments, Raman micro spectroscopy analysis, petrographic and scanning electron microscope (SEM) analysis, interpretation of results and preparation of manuscript were carried out by Christina Comuso with supervision by Dr. Bjorn Von der Heyden and Dr. Mathew Severs. Assisted interpretations of preliminary microthermometry analysis were done by Christina Comuso and Dr. Matthew Severs. Interpretation of Raman spectroscopy was done by Nomathamsanqa Lindokuhle Makhathini. Proceeding the submission of this thesis Ms. Makhathini, Dr. Bjorn Von der Heyden and Dr. Mathew Severs will assist in the final stages of writing before submitting this manuscript to the editors. Lastly, oxygen stable isotope analysis was performed at the University of Cape Town by Professor Chris Harris.

3.1 Abstract

Fluid inclusion (FI) and isotopic analysis of the structurally, lithological and temporally different Main Reef Complex (MRC) and Hope Reef (HR) within the Fairview Mine of the Barberton Greenstone Belt (BGB) indicates a possible evolving fluid from a similar fluid source. Fluid inclusion data shows both aqueous and H_2O- CO_2 rich fluids. Clathrate melting temperatures ranged from 3°C to as high as 18.9°C suggesting a presence of CH_4. These clathrate temperatures also indicate a thin liquid or vapor film that may exist within the FI as well as a fluid composition of H_2O-CO_2-CH_4. Finally, homogenization temperatures for the Hope Reef range from 198°C to 352°C and from 202 to 382°C for the Main Reef Complex, suggesting a possible link in the mineralizing fluids composition. Higher gold abundance is present in graphitic shales of the MRC whereas a lower abundance of gold is found in the HR where, the latter devoid of, graphitic

alteration. Differences present in the alteration, surrounding lithologies, proximity to the Sheba Fault, and structural kinematics are the key components as to why there are variations present in the analyzed datasets. Slight differences were revealed through a student t-test when comparing microthermometry data of primary and secondary FI between the MRC and HR. Whilst there seems to be a similarity in the data between the two reef structures, it is the subtle differences in the data that are crucial in understanding the history of the fluids. As such, this newly gained knowledge on the MRC and HR of the Fairview Mine provide an overall view on how Archean orogenic gold systems and the fluids that infiltrated them evolved through geologic time. Geochemical data from this study coupled with previously interpreted structural kinematics allow for a more finite exploration in economically viable gold regions.

3.2 Introduction

The uniquely gold rich Barberton Greenstone Belt of South Africa is one of the oldest and still producing gold regions in the world (Goldfarb, 2017; Altigani et al., 2016). Although many perplexities surround the formation and gold abundance of these ancient orogenic deposits, a further dissection of the mineralizing complexes within these systems have helped to piece together the puzzle on the origin and evolution of the world's orogenic gold systems (Goldfarb, 2017; Tomkins, 2013). The global accepted generic models of orogenic gold deposits remain unanswered; however, the consensus is that metamorphic fluids are responsible for most of the world's orogenic gold endowment (Groves et al., 2018). What is also agreed is that deformation provides permeability's in the otherwise impermeable wall rocks, which allow for the dependent fluid -wall rock interaction that is critical for gold deposition. Models produced by Colvine, (1989) and Groves et al.,(1998) suggest extensive fluid transport distances, that come from great depths, allowing hydrothermal fluids to interact with surrounding wall rock before being halted at more crustal depths. Orogenic gold commonly forms late, in second and third order structures such as compressional zones proximal to major faults and within shear zones (Bierlein and Maher, 2001; Dirks et al., 2013; Altigani et al., 2016; Groves et al., 2018).

As interpreted by Glyon-Jones and Kisters 2018, 2019, the Fairview Mine within the BGB contains a variety of geometrically distinct reefs with different orientations and wall rocks, the most prominent of which are, the Main Reef Complex and the Hope Reef Complex, that underwent multiple large-scale deformational phases which created the ideal environment for fluid flow and gold mineralization as explained by Groves et al., 2018. These two reefs show variations in the overall structure, timing, gold grades, and lithologies.

Gold mineralization within the BGB is relatively late and interpreted by many to be during late D_3 to early D_4 deformation events (Anhaeusser, 1965, 1976a, 1976b; Wigget et al., 1986; De Ronde et al., 1992; Robertson et al., 1994; Otto et al., 2007; Dziggel et al., 2010; Munyai et al., 2011; Dirks et al., 2009, 2013; Gloyn-Jones and Kisters, 2018, 2019). Geochronology analysis previously done by De Ronde et al., 1991 indicate the age of BGB gold mineralization to be 3126 ±26 Ma, with more recent studies (Dziggel et al., 2010) providing ages between 3030 to 3040 Ma. The locality, structural fabrics, lithology, and gold mineralization styles seen within the Fairview Mine make it the ideal place to test the evolution of gold formation in an Archean orogenic deposit.

To better understand the type of fluid and cause of gold mineralization in orogenic systems it is critical to couple structural interpretations with geochemical and isotopic analysis (Goldfarb et al., 1988). Previous fluid inclusion and isotopic studies done by De Ronde et al., 1992, within the BGB at Bellevue, Montrose, Pioneer, Rosetta, Abbotts, Fortuna, Three Sisters and Fairview Mines, lack the structural component necessary to understand fluid pathways and mineralization within structural regimes. No studies have yet attempted to understand the possible variations in the fluid evolution the MRC and HR within the Fairview Mine. This study will utilize the structural analysis previously done by Glyon- Jones and Kisters 2018, 2019 to apply a geochemical and isotopic data set to both the MRC and HR. These data sets will be collected by performing microthermometry experiments, Raman micro-spectroscopy, oxygen stable isotope and scanning electron microscope analysis, which will in turn provide information on the composition and formational conditions of the mineralizing fluids present within quartz and quartz-carbonate views in the MRC and HR.

3.3 Regional geology

The BGB is a multiply deformed NE trending synclinal belt bounded by 3.5-3.1 Ga Tonalite-Trondjhemite-Granodiorite (TTG) and granites centralized to the east of the Kaapvaal Craton (Anhaeusser et al., 1981; De Ronde et al., 1992; Lowe and Byerly 1999; Lowe and Byerly 2007; Gloyn-Jones and Kisters 2018). The Fairview Mine is situated in the BGB, is dominated by the Eureka and Ulundi synforms.

The Barberton Greenstone Belt is comprised of the following stratigraphic units: Mafic-ultramafic volcanic rocks that are interbedded with thin layered chert and felsic volcanics make up the Onverwacht Group (3550-3270 Ma); turbiditic greywacke, chert, mudstone, shale, banded iron formation (BIF) and minor volcanoclastic rocks form the Fig Tree Group (3260- 3225 Ma); the

upper most portion of the stratigraphic sequences is dominated by clastic sedimentary, sub greywacke, quartzose and feldspathic sandstones of the Moodies Group (3225- 3215 Ma) (Lowe and Byerly 1999; Lowe and Byerly 2007). Along the central-southern part of the Eureka and Ulundi Synclines sits the Fairview Mine as seen in Figure 3.1 (Otto et al. 2007). Periods of NW-SE shortening are seen throughout the BGB as upright folds (F3a) trending NE-SW (Gloyn- Jones and Kisters, 2018, 2019). Continuous folding events have resulted in a NW-SE axial plane F3b and a double fold of the Ulundi Syncline (Gloyn- Jones and Kisters, 2018, 2019). These multiple folding events of the Eureka and Ulundi Synclines lead to the multitude of quartz and quartz-carbonate veins seen throughout the mine (Dziggel et al., 2007). The increase in structural porosity through these less competent rocks allowed for gold mineralization within these numerous veins within the Fairview Mine (Hofmann and Harris 2008; Altigani et al., 2016). The Sheba Fault, which acts as a catalyst for most deformational events within the Fairview mining district is made up of various sheared and regressed serpentinites, talc- carbonate schists and cherts all found within the Weltevreden Formation fixed between both the Ulundi and Eureka synforms (Ramsay, 1963; Byerly et al., 1996; Lowe and Byerly 1999; Gloyn-Jones and Kisters 2018). The formation of the HR and the MRC orebodies is predominantly linked to progressive phases of horizontal NW-SE direct shortening which has been correlated to late D_3 deformation, refer to Figure 3.2 (Gloyn-Jones and Kisters 2018).

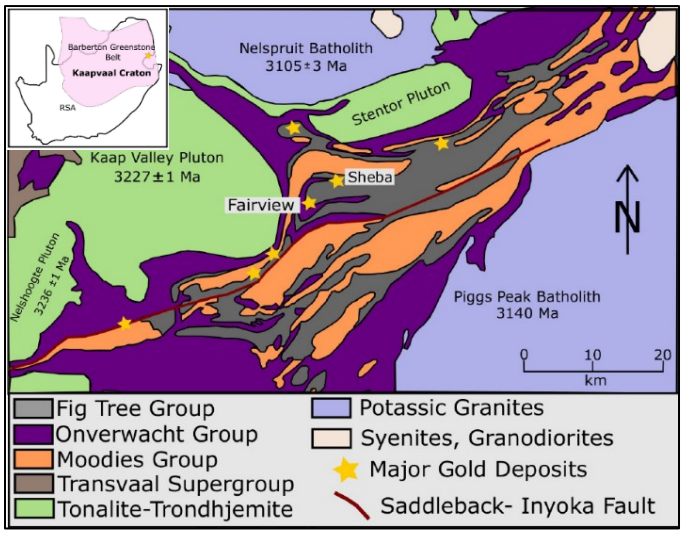

Figure 3.1: Regional map of the Barberton Greenstone Belt illustrating gold mine localities, stratigraphic lithologic groups and surrounding intrusive bodies. The second map shows the locality of the Barberton Greenstone Belt and Kaapvaal Craton (colored light pink) within the Republic of South Africa. Modified from (Anhaeusser et al., 1981; Dirks et al., 2013; Agangi et al., 2014; Gloyn-Jones and Kisters 2018).

3.3.1 Hope Reef Complex (HR)

The HR comprises two high-angle, brittle-ductile shear zones. There are two main mineralized shear zones within the HR that are characterized as sets of high-angled brittle-ductile regions. First being a shallow ESE dipping, slightly undulating NNE trending reef, and several moderate to steeply dipping NW and NE trending structures (Gloyn- Jones and Kisters, 2018). The entirety of the Hope Reef is made up of both shallow and steeply dipping mineralized zones that are confined to the greywacke units of the Fig Tree Group (Gloyn-Jones and Kisters, 2018). The portion of the HR where mineralization and this study is focused is within the shallow reef. Structural analysis from Gloyn-Jones and Kisters, 2018 was done within the Fairview Mine of the Hope Reef complex at level 58. The shallow portion of the reef and shows high grade mineralization with associated quartz veining, sulphide mineralization, and sericite, chlorite, carbonate with minor albite and rutile alteration, all bounded by a SE shallow dipping brittle-ductile shear zone system (Gloyn-Jones and Kisters, 2018). The Hope Reef is situated in the lower portion of the Sheba Formation above the Sheba Fault and Main Reef Complex, composed of mostly a greywacke package (Gloyn-Jones and Kisters, 2018).

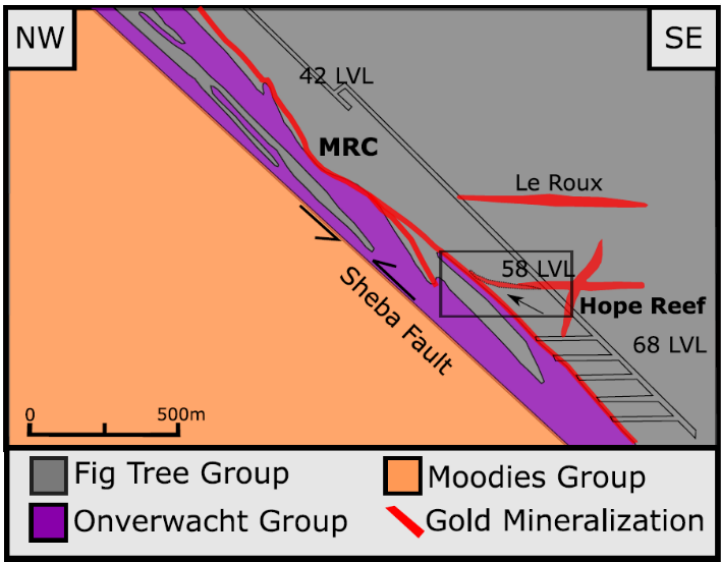

Figure 3.2: Cross section of Fairview Mine geology illustrating the lithologic groups in correspondence to the Sheba Fault and the MRC and HR. The boxed region and arrow indicate an inferred contact between the HR and MRC. Modified from (Anhaeusser et al., 1981; Dirks et al., 2013; Agangi et al., 2014; Gloyn-Jones and Kisters, 2018).

3.3.2 Main Reef Complex (MRC)

The MRC is a moderately- to steeply- SE-plunging orebody governed by a jog-like corridor characterized by a severely mis-orientated brittle-ductile shear zone confined to the immediate hanging wall of the greywacke and shale units along the Sheba Fault zone (Gloyn-Jones and Kisters, 2019). In the MRC of the Fairview Mine, higher gold grades are spatially associated with shale units of the metasediments in the lower Fig Tree Group and gradually terminates along strike (Gloyn- Jones and Kisters, 2019). A graphite-carbonate alteration is seen throughout the sheared margins of the MRC in shale rich regions. There are two distinct forms of mineralization within the MRC; sulphide mineralization that is associated with blackish-grey quartz carbonate veins and mineralization of similar sulphides dominantly in the surrounding shale wall-rocks (Gloyn-Jones and Kisters, 2019). Samples for this study were collected on level 60 of the 25/27 mining block.

3.4 Methodology

3.4.1 Sample description

Sampling took place at Sheba and Fairview Mines in Barberton, South Africa. Structurally oriented quartz veins were sampled from two major mineralizing reef complexes, the Hope Reef Complex and the Main Reef Complex. A total of twelve samples were collected from HR, eleven samples from MRC and two from the Sheba mine. These samples represent the major vein sets that are associated with mineralization and major structural fabrics for both the HR and MRC, refer to Table 1 for more detail. Bulk rock samples were collected in HR (level 58) of both mineralized zones and of the surrounding wall rock alteration. In MRC (stope 195 level 60 mining block 25/27) both black quartz and altered wall rock samples were collected in efforts to compare against the mineralization of HR. Each sample was collected underground from the wall of areas that were previously mapped by Gloyn-Jones and Kisters, 2018. The samples described by Gloyn-Jones and Kisters, 2018, 2019, were taken on different levels of Fairview Mine however the descriptions are similar for this study since the quartz veins types do not vary at each level of the ore bodies. Quartz veins were measured using a meter tape however structural measurements are based off of general trends of veins as samples were not collected in situ. Photographs and notes were also taken at each sample site. Collected samples were further processed into oriented billets

with a main interest in the black quartz veins. These billets were then polished and mounted to be formed into double polished thick sections for further geochemical and fluid inclusion analysis.

3.4.2 Petrography

Petrographic analysis was conducted using a Nikon Eclipse E-200 polarizing microscope and a Zeiss Primotech petrographic microscope and camera for ore microscopy. Through transmitted light, the mineral composition and textural variations of each sample were recorded. Fluid inclusion assemblages (FIA) within quartz grains were identified and mapped. Primary and secondary FIAs were distinguished to focus on samples that were clearly related to the ore veins for further geochemical analysis on liquid and vapor phases.

Reef	Sample	Composition	Orientation
Hope Reef	*H58SQA*	Black quartz, gold, arsenopyrite, pyrite, apatite	High angle steep veins with NE strike and SW dip of about 15° to 55°
	H58PQM7/8	Black quartz minor arsenopyrite, pyrite	Top to NW parallel to lineation
	HB2	Hydraulic breccia, chlorite alteration, arsenopyrite, pyrite, black quartz	Qtz carb hosted sulphide sericite chlorite carbonate alteration
	HRMHB	Hydraulic breccia, chlorite alteration, arsenopyrite, pyrite, black quartz	Hydraulic Breccia with quartz carbonate, sulphide alt., sericite/chlorite alteration
	HRPV6	Black quartz and wall rock	Pinnate quartz vein
	HRPQM	arsenopyrite, pyrite, black quartz, wall rock	Top to NW parallel to lineation, pinnate quartz, NW moderate - shallow dip
	HRCCP	arsenopyrite, pyrite, black quartz, wall rock	Late stage carbonate vein that cross cuts pinnate quartz
	HRFF	Black quartz, arsenopyrite, pyrite, wall rock	N to NE strike, SE dip (10° and 40°)
	HRFP12	Chlorite alteration, black quartz, arsenopyrite, pyrite, wall rock	N to NE strike, SE dip (10° and 40°)
Main Reef Complex	*CFI2*	Quartz carbonate, black quartz, pyrite, arsenopyrite, chlorite alteration	Mineral Cutoff Associated with normal fault, moderate SE dip, related to D4 normal movement
	CFI4	Quartz carbonate, black quartz, pyrite, arsenopyrite, chlorite alteration	Mineral Cutoff Associated with normal fault, moderate SE dip, related to D4 normal movement
	MRC1 25/27	Black quartz with minor arsenopyrite, pyrite, calcite	Foliation parallel Veining S1HW foliation, late D3 top to the NW dextral strike slip, SE dip
	MRC2 25/27	Black quartz with minor arsenopyrite, pyrite, calcite	Foliation parallel Veining S1HW foliation, late D3 top to the NW dextral strike slip, SE dip
	MRCQ 25/27	Black quartz with minor arsenopyrite, pyrite, calcite	Foliation parallel Veining S1HW foliation, late D3 top to the NW dextral strike slip, SE dip
	MRCLAV	Black quartz with minor arsenopyrite, pyrite, calcite	Low angled quartz vein sub horizontal- to shallow NW dips of up to 25°
	MRCBQ	Black quartz with minor arsenopyrite, pyrite, calcite	Black quartz parallel to foliation
	MRCFP	Black quartz with minor arsenopyrite, pyrite, calcite	Foliation parallel relative to shear motion
	MRCCM	Black quartz with minor arsenopyrite, pyrite, calcite	Late stage quartz carbonate located within shear zone below low angled quartz vein

Table 3.1: Sample names, lithological composition and structural orientation from the Main Reef Complex and Hope Reef Complex.

3.4.3 SEM-CL

High resolution optical data was gathered with the use of the Carl Zeiss MERLIN High Resolution Field Emission Scanning Electron Microscope (FE SEM) at the Central Analytical

Facilities at Stellenbosch University. The Cathodoluminescence (CL) Detector and Backscattered Electron Detector (BSD) attachment was also used in conjunction with the petrographic analyses to help located primary FIA in growth zones of quartz grains. SEM was also used to indicate micro cracks within quartz grains to compare the structure features to FIA distribution. For elemental spot analysis the Electron Dispersive X-ray Spectrometer (EDXS) was used. Analytical working distance ranged from 8 to 10mm. A beam current of 10.00nA and an optimum beam acceleration voltage (EHT) of 10.00 to 20.00kV was used to improve image and micrograph quality. Primary zonation patterns in quartz were distinguished using the cathodoluminescence (CL) coupled with a cryo stage in the Zeiss Merlin SEM. Samples were cooled using liquid nitrogen to roughly -180°C for higher resolution and greater luminescence of quartz grains. Magnifications for each spot analyzed and sample, ranged from 30x to 460x. To reduce the presence of charged particles each sample was coated with carbon prior to each analysis.

3.4.4 Microthermometry

Microthermometric analyses were performed on samples containing viewable fluid inclusions and FIAs from double polished thick sections (100µm) at the University of Cape Town and Stellenbosch University. Thick sections were dissolved in acetone for 24 to 48 hours to remove samples from the glass slide. Then each sample was cut in a systematic grid to maintain the orientation. For each thick section, approximately fifteen chips were created. A minimum of five quartz grains from each chip were analyzed in order to sufficiently describe the FIA within each sample. Seven samples from MRC were analyzed including mining block 25/27(MRC25/27), low angled veins (MRCLAV), foliation parallel veins (MRCFP), black quartz (MRCBQ) and carbonate cut- off veins (CF1). From HR five samples were selected including hydraulic brecciated quartz (HB2), foliation parallel veins (HRFP12), and pinnate quartz veins (HRPV6), (HRPQM8), (HRPQM7).

Detailed illustrations were made for each FI and FIA to show relationships between all present fluid generations. Fluid inclusions were described at room temperature based on phase relation characteristics. Microthermometric measurements were conducted using a Linkam THM600/HFS600 temperature-controlled stage with a T95 system controller that was placed on an Olympus BX53 microscope. Calibration was set using H_2O/CO_2 inclusions in quartz against

the melting point of CO_2 (T_m= -56.6°C). These calibrations were set by Linkam and checked by reproducing T_f of two-phase CO_2- H_2O FI.

Secondary and primary fluid inclusions were analyzed strictly excluding decrepitated, reequilibrated or questionable FI. Decrepitated FI were identified as completely black, cracked, or deformed. Phases transitions analyzed were measured at least two times to ensure reproducible results. All freezing experiments were done first using liquid nitrogen at a cooling rate of 15°C/min down to -180°C. Upon heating samples back to room temperature (25°C) the rate was lowered to <5°C/min between -20°C to 0°C to locate ice melting temperatures. For homogenization experiments temperatures were increased in increments of 100°C at a rate of 10°C/min. Temperatures were maximized at roughly 400°C where most FI decrepitated. Salinities for aqueous-rich fluid inclusions were calculated using computer package FLUIDS (Bakker, 2003) as well as the HOKIEFLINCS Excel spreadsheet (Steele-MacInnis et al., 2012). Salinities for CO_2 – H_2O rich fluid inclusions were calculated based on Steele-MacInnis, 2018. All microthermometry data was analyzed through the LINKs program.

3.4.5 Stable isotope

A total of ten samples from the Fairview Mine (five from HR and five from MRC) were tested for $\delta^{18}O$. Black quartz grains from HR and MRC were crushed and isolated at 4g per sample to be analyzed for oxygen isotopes at the stable isotope laboratory of the Department of Geological Sciences, University of Cape Town utilizing the laser method fluorination of Harris and Vogeli, 2010. Oxygen isotope ratios were measured based on the levels of oxygen gas present. All data is given in relation to SMOW and in δ notation. For full fluorination laser methodology refer to Harris and Vogeli, 2010.

3.4.6 Raman spectroscopy

Raman micro-spectrometer analysis were performed in the School of Physics at Witwatersrand University. Representative samples of viewable fluid inclusions from both HR and MRC were analyzed using a Horiba LabRAM-HR Raman spectrometer, mounted to an Olympus BX-41 microscope with a Lexel Model 95 SHG Argon ion laser. The system consists of a liquid nitrogen multi-channel charge-coupled device (CCD) detector which causes backscattered light to spread through a diffraction grating of 600 lines/mm. The green light Ar ion (λ=514.5 nm) source

was used. Spot analysis size was roughly 0.9 numerical apertures when using the 100x magnification objective. The spectrum was calibrated using the silicone peak representative of the quartz host (roughly 520.6cm^{-1}). The dwell time for each sample run was 90sec. The liquid and vapor phases of selected FI were analyzed as well as the quartz host. Vapor phases were analyzed to record the presence of CO_2, CH_4, H_2O, and N_2. All Raman data was quantitatively compared to the data of Frezzotti et al., 2012 as it indicates the Raman spectrum signatures for CO_2, H_2O, CH_4, and more. Spectrum was normalized using both LabSpec v5 and WinXAS v3.x software's.

3.5 Results

3.5.1 Petrography

Petrographic work was performed on 100µm double polished thick sections, resulting in a higher birefringence of quartz. Each thick section was mapped out to identify mineral assemblages and fluid inclusions present to help develop a classification for the types present.

Fluid inclusions were categorized into five separate types as seen in Figure 3.3. Type I and II fluid inclusions were the dominant type found in both the MRC and HR. Both Type I and II occurred as primary and secondary FI. An abundance of Type III mono phase inclusions were also present, however the average ≈1µm size made it impossible to analyze. Several Type IV were found in quartz grains of both HR and MRC samples. These triple phase solid-bearing FI were elongated in shape, with a larger liquid phase, followed by a vapor and an unidentified soild phase of <20%. Type IV did not form as a FIA and therefore were interpreted as Type I FI that aquired a trapped solid at a later stage. Large populations of Type V FI occured within quartz grains and zoned regions in quartz. These were identified by their larger size, whispy shape and complete black color. The distribution of FI types amongst both the MRC and HR are relatively similar, however there are some mineral texture variations between the two.

Type	Physical State		Composition	Examples	Size µm
I	Liquid-rich, two-phase	L + V	L >50%		2-10
II	Vapor-rich, two- phase	V + L	V=50 to 80%		2-8
III	Monophase liquid/vapor	L/V	NA		<2
IV	Multiphase	L+V+S	S<20%	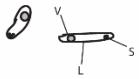	5-12
V	Decrepitate/breached	NA	NA		~8-10

Figure 3.3: Chart illustrating the types of fluid inclusions present in both MRC and HR from selected and examined samples. Chart shows the composition, proportions and gives physical sketches of each fluid inclusions.

3.5.1.a Hope Reef Complex

The mineral composition of the Hope Reef comprises predominantly quartz, carbonate followed by pyrite and arsenopyrite. Minor carbonates are present in areas with recrystallized quartz grains. Samples HRPQM8 and HRPQM7 have metamorphic mineralized regions of acicular apatite crystals that cut through quartz grains (Figure 3.4A). Quartz shows a significant reduction in grain size in regions where sulphides are present and along contacts with the wall rock. Carbonates have a slight optical zonation and are transected by quartz grains; this was seen using SEM-CL imaging.

There is a variance in the population amongst the types of FI, predominantly large amounts of Type III monophase inclusions, which were too small to analyze. Type IV FI were visible in pinnate quartz veins in a very small population. Multiple clusters of FI overlap making it difficult to conclusively distinguish between primary, secondary and pseudosecondary FIA. Secondary FIA have the greatest population, but due to the number of FIA overprints, it is difficult to differentiate one FIA from another. Most secondary FIA are noticeable in quartz grains with a lesser population of FI. Primary FI were more isolated and proportional in their vapor (V) to liquid (L) distribution to that of neighboring FI.

Secondary and pseudosecondary FIA were seen following healed cracks and fractures within quartz grains. Lighter shaded regions of quartz were best for viewing primary FI centralized within quartz grains and on the outer contours of the grains. Type V FI were less prominent in HR compared to the MRC. Type V FI in MRC formed in both trails and as isolated inclusions. Primary, secondary and pseudo secondary FIA form within quartz grains for all analyzed samples in HR and MRC. Type I and type II FI were used in microthermometry and Raman analysis due to their larger size (>6 µm) and the fact they represented distinguishable FIA.

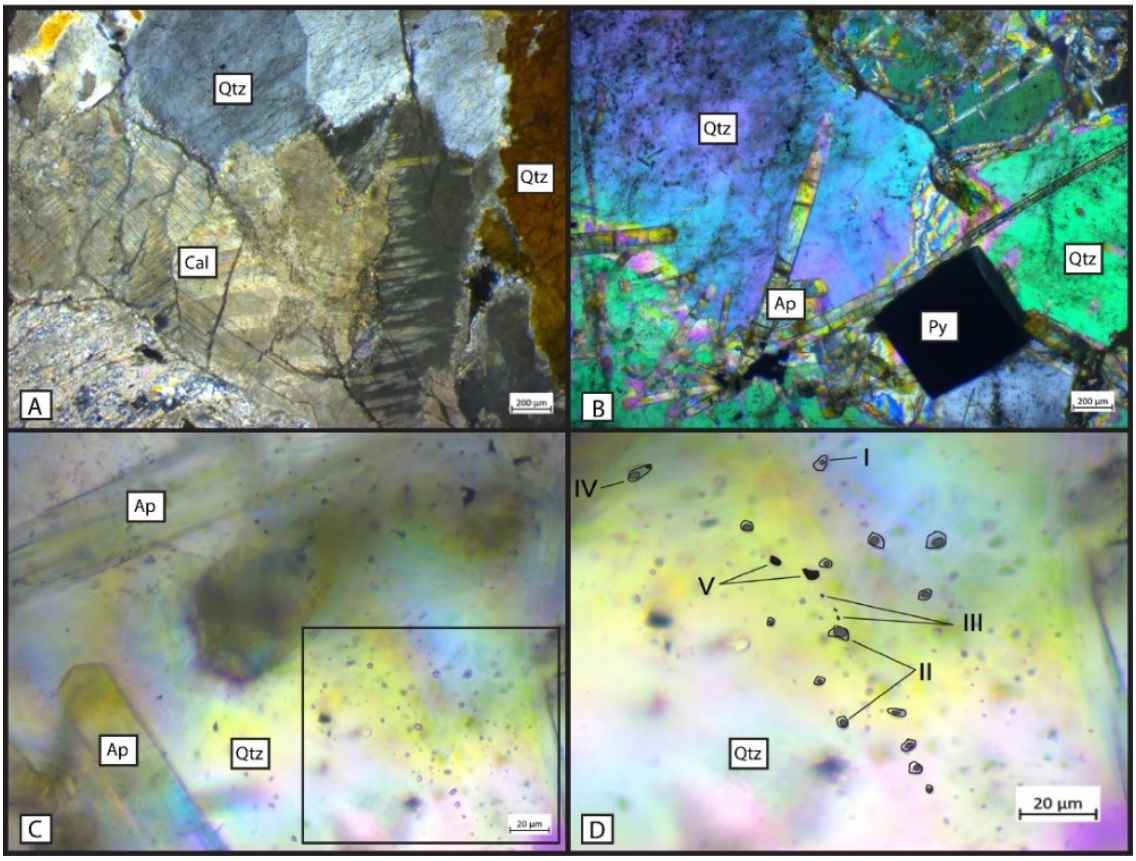

Figure 3.4: A. Carbonate surrounded by whole quartz grains and recrystallized quartz from sample HB2. B. Apatite, pyrite and quartz mineralization within sample HPQM7. C. Secondary fluid inclusion assemblages cross cutting quartz grains and surrounded by elongated apatite crystals from sample HPQM8. D. Zoomed in picture of C showing the types of FI present in quartz grain. Fluid inclusions in this sample show no preferred orientation. All images above taken using a petrographic microscope.

3.5.1.b Main Reef Complex

There are greater amounts of recrystallized quartz and primary zonation in quartz within the MRC. Several quartz grains display a poikilitic texture with porphyroblasts of euhedral pyrite grains (Figure 3.5). More carbonates are present in areas with well-defined mylonitic, metamorphic fabrics in quartz grains then that of the HR. Arsenopyrite and pyrite are seen throughout MRC samples mainly along regions of carbonate and quartz grain contacts, but sometimes within quartz grains. Unlike the HR, there was no presence of apatite within MRC samples; however, there has been evidence of rutile found in previous studies done on MRC samples (Gloyn-Jones and Kisters, 2019). Some thick sections contain fragments of the Fig Tree greywacke wall rock where a reduction in grain size of quartz and quartz carbonate was present. These areas also show a pervasive mylonitic fabric around sulphides and quartz carbonate grains. Smaller quartz grains are seen crosscutting larger quartz grains, which are surrounded by opaque sulphides.

Secondary FIA are clearly seen cutting across crystal grain boundaries of quartz, however, as stated there is a multitude of FIA overprinting. Healed fractures harbor large amounts of secondary and pseudosecondary FIA. Primary FI occur mainly in the growth zones of quartz grains, notably in sample MRC25/27. Type V primary FIA were seen around the growth zones within a quartz grain, however the FIs were decrepitated making them useless for further analysis. A small amount of Type IV FI were found in low-angle quartz veins, but not a large enough population to determine if it was a daughter crystal or trapped solid. Two double bubbles have been observed in larger isolated FI (>8μm), but it was not possible to place them in a definable FIA and they were thus not analyzed further.

The overall morphology of CO_2-H_2O bearing FI is rounded-sub euhedral, classified as both Type I and Type II FI. A small number of carbonic FI contained trapped solids however it is uncertain as to what the composition of the solid phase is. Brownian motion was visible in carbonic FI from MRC as temperatures were increased upon heating. Double bubbles were seen in two FI from the MRC. Large populations of aqueous-rich FI were present in both reefs and were represented mainly as Type I liquid dominate. Morphology of Type I FI was predominantly rounded with some having a less spherical more euhedral shape. Aqueous-rich FI formed as secondary and primary FIA.

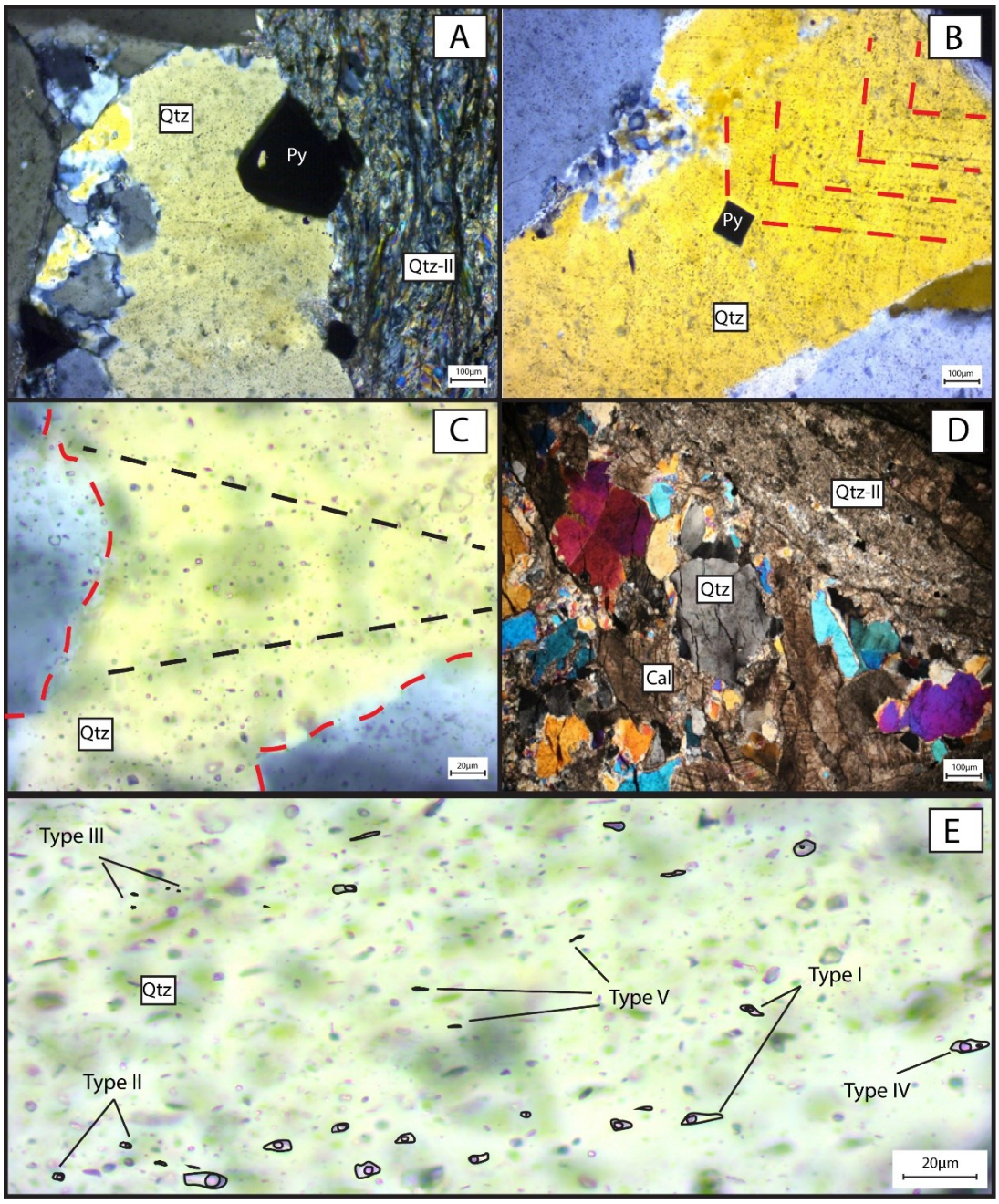

Figure 3.5: A. Recrystallized quartz (qtz-II) forming along quartz with sulphide mineralization forming along contact. B. Quartz grain with primary growth zonation of Type V FI (red dashed line) and cubic pyrite within. C. Quartz grain illustrating secondary FIA (black dashed line) and Type II FIA (red dashed line) forming along grain boundary. D. Quartz, calcite, and recrystallized quartz (qtz-II) forming along contact with wall rock. E. FI types present within MRC quartz showing distribution of FI. All images are from sample MRC 25/27

3.5.1.c Paragenesis of minerals within reef complexes

Reflected light microscopy of both the HR and MRC illustrates the growth habits of sulphides, gold and quartz. There are acicular arsenopyrite grains present within the HR that cut through altered pyrite grains. Gold is found forming within both arsenopyrite and pyrite, and within quartz grains for the HR and MRC. Seen under reflected light, there are zonation patterns within pyrite grains in MRC, but not in HR samples. There are large amounts of altered pyrite and quartz in both reefs and sulphides, which seem to form along contacts of quartz and quartz carbonate as seen in Figure 3.6C. A mineral paragenesis was developed based off analyzed samples, refer to appendix III for interpreted paragenetic model.

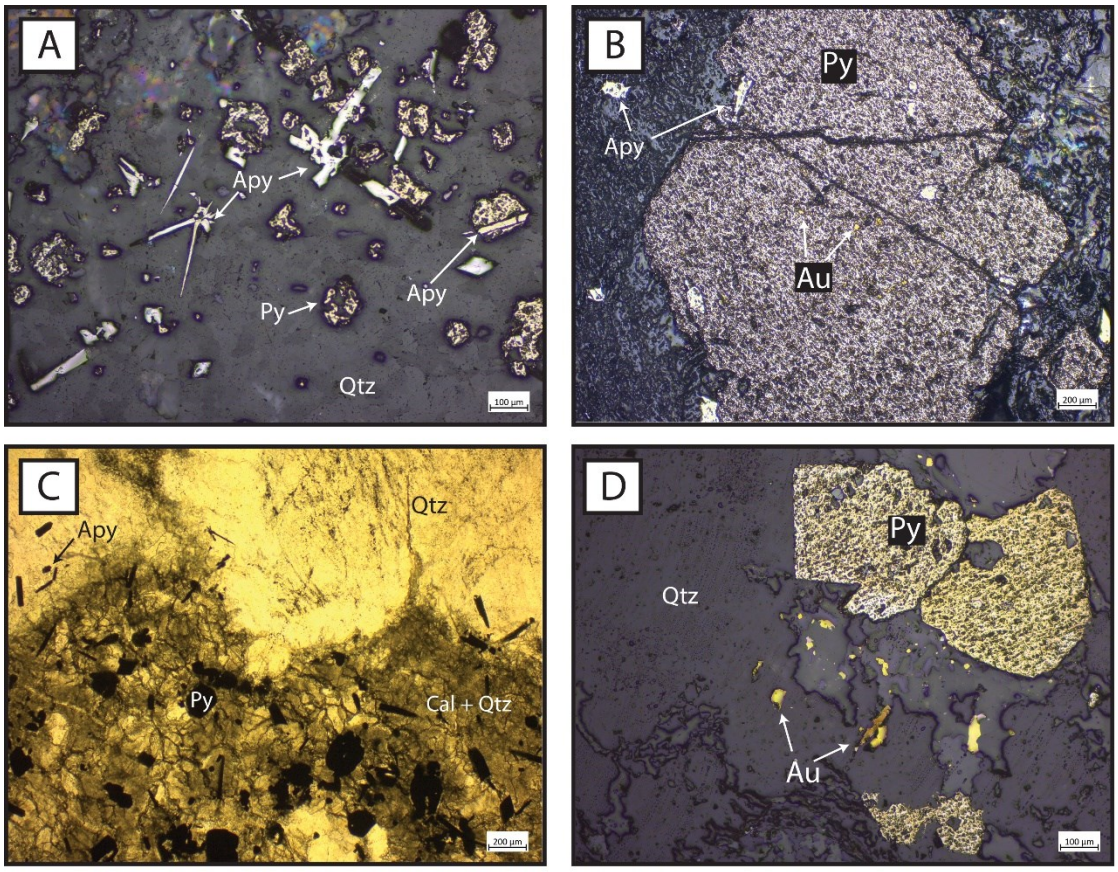

Figure 3.6: A. HR: Quartz hosting both arsenopyrite and pyrite. Arsenopyrite formed in an acicular habit. Image taken through ore microscopy. B. MRC: Quartz grain hosting gold and pyrite hosting zoned arsenopyrite seen through ore microscopy. C. MRC: Mylonitic fabrics in calcite and quartz grains where pyrite is formed along mineral contact, seen through petrographic analysis. Acicular arsenopyrite is throughout the surrounding contact of quartz, calcite and the mylonitic fabric. D. HR: Quartz and quartz carbonate contact where acicular arsenopyrite and euhedral pyrite.

3.5.2 Microthermometric analyses

All fluid inclusions used for microthermometry experiments were hosted in quartz grains to decrease the concern about calcite hosted FI being more easily re-equilibrated (Prezbindowski and Larese, 1987). The distribution of FI types is seen in samples to be highly dependent on the amount of FI overprinting. The effects from the numerous fluid pulses are seen throughout both reefs by the re-equilibration and decrepitation of FI.

Clearly defining primary versus secondary FIA was not always possible due to the overprinting of fluid pulses. Evidence indicates that secondary FI may have more influence on ore mineralization over primary FI, making secondary FI just as important to analyze (Fagereng et al., 2011). Many inclusions follow no preferred orientation, however primary FIAs zonation is visibly present in some quartz grains. Type I and II inclusions were exclusively examined through microthermometry due to the availability in size and population and their clear definition of FIAs. The presence of secondary or pseudosecondary monophase FI may be due to a drastic pressure and temperature change in the environment during a deformational event or influx of fluid. Unfortunately, data from these inclusions is unavailable because of the size limitation.

The abundance of Type V FI was minimal, but when examined petrographically, it was evident that the solid material was randomly trapped during the formation of the FI and did not define any clear FIA. When Type V FI were examined under the Raman micro-spectroscopy, they showed slightly higher levels of graphitic carbon then other FI did, indicating possible trapped solids of graphite. Residual entrapment artifacts such as “necking down” as described by Roedder, 1984, were present in roughly four FI samples but were not included in any analyses.

Liquid-rich FI (Type I) are interpreted as aqueous dominated, alternatively, vapor- rich FI (Type II) are interpreted to be CO_2 – H_2O- CH_4 dominated. Salinities were calculated from carbonic-rich FI using the clathrate melting temperatures after Steele-MacInnis, 2018. Salinities for aqueous-rich inclusions were calculated using equations from HOKIEFLINCS by Steele-MacInnis, et al., 2012 and the FLUIDS 1 package by Bakker, 2003 and inputting Tm_{ice} into calculations for salinity output. Microthermometric results can be seen in Figure 3.7 and in Table 3.2. For all salinity data see Figure 3.8.

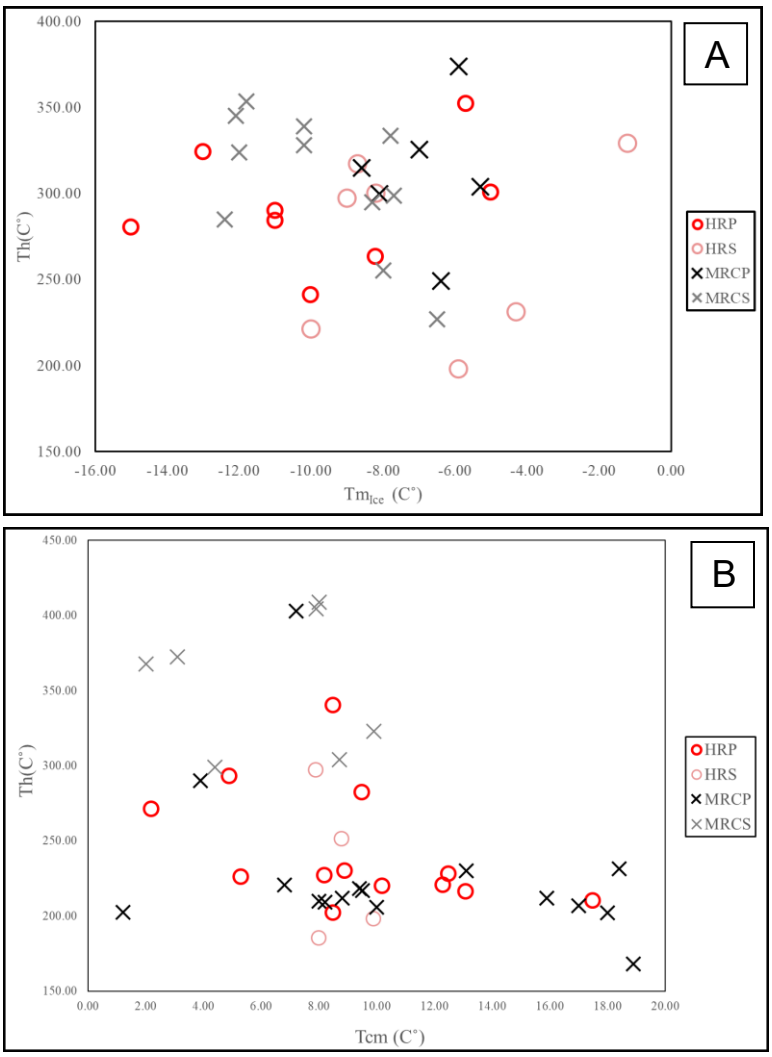

Figure 3.7: Microthermometry data of MRC and HR quartz vein samples from Fairview Mine. A. Scatter plot of homogenization temperatures verse the temperature of ice melt for aqueous-rich inclusions. Black crosses represent data of primary fluid inclusions from the MRC while grey crosses show secondary fluid inclusion data from MRC samples. Red circles indicate primary fluid inclusion values from HR and light red-pink circles represent secondary fluid inclusion data also from HR. B. Clathrate melting temperatures plotted against homogenization temperatures for CO_2-H_2O rich fluid inclusions. The same color and marker type were used for B as explained from A.

The distribution of carbonic-rich fluid inclusions was nearly even amongst both reef complexes. Looking at the data, there is a slight difference in the total homogenization (T_h) and total melting of clathrate (Tcm) values from HR to MRC. Data for carbonic inclusions is separated into primary and secondary for each examined reef, see Table 3.2.

Table 3.2: Microthermometry data for both the MRC (Left) and HR (Right) indicating primary and secondary fluid inclusions. The FI type is indicated by an S (Secondary) or P (Primary). This data represents only the FI that showed visible Tmice, Tcm, and Th temperatures during microthermometry experiments.

Sample	Type	T_{mice}	T_{cm}	T_h
MRCFP22	S	-	9.8	275
	S	-	8	225.6
	S	-	10.5	256.9
	S	-	14.8	337
	S	-12	-	324
	S	-11.8	-	353.6
	P	-12.4	-	284.9
MRC2527	S	-6.5	-	227
	P	-	13.9	290
	S	-7.7	-	298.8
	S	-8.3	-	295
	S	-12.1	-	345.2
MRCLAV18	S	-10.2	-	338.9
	P	-8.6	-	255.4
	S	-10.2	-	328
	S	-7.8	-	333.4
	P	-8.6	-	315
	P	-5.3	-	304
	P	-6.4	-	249
	S	-	10.4	299
	S	-	8.7	304.2
	S	-	9.9	322.9
	S	-	12	367.6
	S	-	13.1	372.5
	P	-8.1	-	299.8
	P	-7	-	325.6
	S	-5.9	-	373.7
	S	-9	-	382.3
	S	-5.5	-	400
MRC Preliminary Data 1	P	-	1.2	202.6
	P	-	8.2	209.3
	P	-	13.1	230
	P	-	9.4	218.2
	P	-	8	210
	P	-	8.8	211.8
	P	-	10	205.9
	P	-	18.9	168
	P	-	6.8	220.7
	P	-	18.4	231.6
MRC Preliminary Data 2	P	-	18	202
	P	-	17	207
	P	-	15.9	212
	P	-	9.5	217
	P	-	11	210
	P	-	10.9	270

Sample	Type	T_{mice}	T_{cm}	T_h
HRPV6	S	-4.3	-	231
	P	-15	-	280.3
	P	-5	-	300.4
	P	-5.7	-	352
	P	-10	-	241
	S	-1.2	-	329
HRFP12	P	-	10.5	340
	P	-8.2	-	263
	P	-11		290
	P	-11	X	284
	P	-13	X	324
	P	-	11.2	271
	-	-14.9	X	312
	P	-	14.9	293
	P	-	19.5	282
	P	-	10.3	226
	S	-1.4	X	249
HRPQM8	S	-	8.8	251
	S	-	7.9	297
	P	-8.2	X	300
	S	-	16	185.1
	S	-5.9	-	198
	S	-10	-	221
	S	-9	-	297
	S	-8.7	-	317
	P	-4.9	-	271.5
	P	-10.1	-	284
	S	-	9.6	281.4
	P	-	10.2	227
	P	-	8.9	230
	S	-	9	266.3
	P	-9.7	-	287
Hope Reef Preliminary Data	P	-	17.5	210
	P	-	12.3	220.5
	P	-	12.5	228
	P	-	8.5	202
	P	-	13.1	216
	P	-	10.2	220

Homogenization temperatures for secondary HR carbonic FI ranged from 185°C to 297°C. Primary FI Th values ranged from 202°C to 340°C. Type I primary and secondary FI homogenized to the liquid phase and Type II FI homogenized to the vapor phase. The temperature of clathrate melt (Tcm) ranged from 7.90°C to 16.00°C for secondary FI and 8.5°C to 19.5°C for primary. Salinities for carbonic-rich FI in HR were quite low, from 2.43 to 9.19 wt. % NaCl. The HR aqueous FI homogenized at 198°C to 329°C for secondary and 241°C to 352°C for primary. Tm_{ice} temperatures for secondary FI were -4.30°C to -10.00°C and slightly higher at -4.90°C to -14.90°C for primary FI. Salinity values for HR aqueous FI calculated based on Tm_{ice} values and Th, were low to moderate at 2.07 to 18.63 wt. % NaCl.

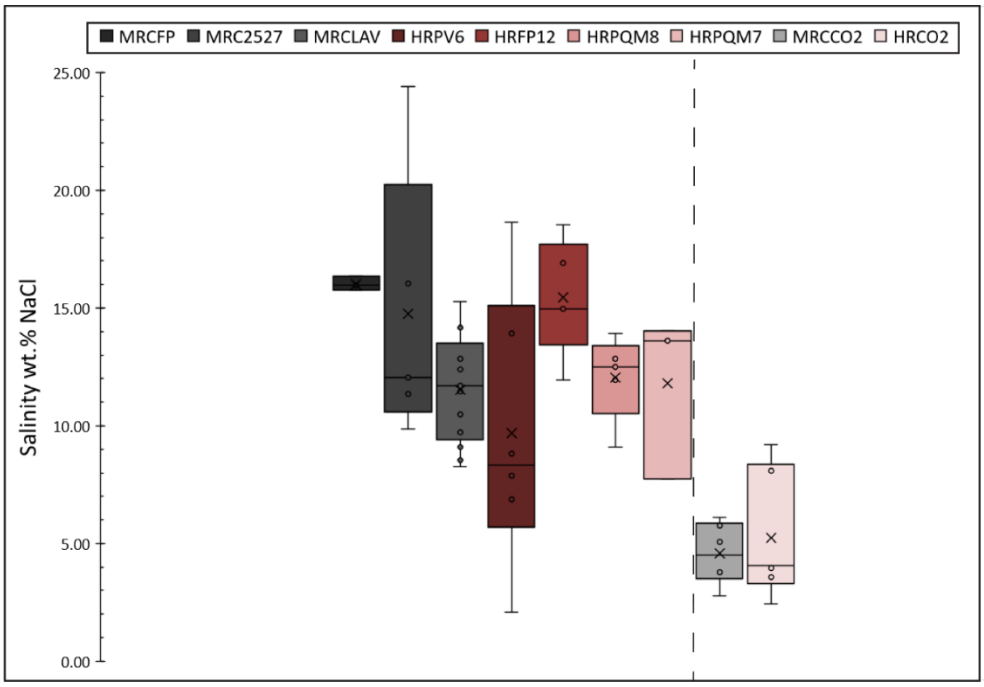

Figure 3.8: Salinity box and whisker plot showing the minimum, maximum and median ranges in NaCl wt. % for selected HR and MRC samples. All MRC samples are indicated by black colors and red colors indicate samples from the HR. The black dashed line separates carbonic-rich and aqueous-rich samples. To the right of the dashed line salinities from MRC and HR were calculated using the clathrate melting temperature (T_{cm}) verse the homogenization temperature (T_h) after Steele-MacInnis, 2018. Plots to the left of the dashed line indicate salinities form both reefs calculated using the temperature of ice melt (Tm_{Ice}) for aqueous-rich FI, verse the homogenization temperature (T_h) after Steele-MacInnis, et al., 2012.

Secondary homogenization temperatures for aqueous dominant FI in the MRC range from 227°C to 400°C and primary FI values range from 249°C to 325.60°C.There is an increase in the temperature of ice melt for the MRC with secondary FI at -5.50°C to -12.10°C and primary FI from -5.30°C to -12.40°C. Salinities are overall higher in the MRC at values 8.28 to 16.34 wt. %

NaCl. A slight increase in Th values seen in MRC carbonic-rich FI samples with temperatures ranging from 225.60°C to 372.50°C for secondary FI and 168°C to 290°C for primary inclusions. Clathrate melting temperatures for secondary FI occurred at 8.00°C to 14.80°C. In primary FI clathrates melted at 1.20°C to 18.9°C. Salinity for carbonic FI in the MRC was a bit higher than HR ranging from 2.76 to 10.67 wt. % NaCl.

3.5.3 Raman spectroscopy

One thin section from both the MRC and HR were analyzed under Raman and approximately 10 FI from each thin section were examined for phases present. Results from micro Raman spectroscopic analysis on Type I and Type II primary FI in the MRC and HR suggested the presence of graphite, methane, water and carbon dioxide within liquid and vapor phases. The liquid and vapor phases of FI from both reefs were analyzed using the green laser to identify CO_2 (1285 and 1388 cm^{-1}), CH_4 (2917 cm^{-1}), N_2 (2331 cm^{-1}), H_2S (2611 cm^{-1}) and H_2O (3000 to 3700 cm^{-1}) (Krolop et al., 2018; Frezzotti et al., 2012). Looking at the short end of the spectrum, mild peaks of graphitic carbon are seen. At the further end of the spectrum, peaks of CO_2, CH_4 and H_2O are prominent (Figure 3.9). It became evident after analyzing the L+V phases of MRC and HR samples through Raman spectroscopy that most FI were CO_2 – H_2O dominant with minor CH_4 and carbon. Raman spectra data from both reefs show similar signatures. Quartz peaks and intensities are based off similar values from Frezzotti et al., 2012. Trace amounts of carbon species were picked up in both MRC and HR within the FI phases and quartz. The disordered induced peak (D), ordered graphite (G) and overtone of disordered graphite (G') bands of carbon values for both reefs are seen in Table 3.3. Values indicate a negative shift in MRC in the D, 19.74 cm^{-1}; G, 3.80 cm^{-1}; and G', 1.06 cm^{-1}.

Table 3.3: Representative disordered (D), ordered graphite (G) and disordered graphite (G') intensities for both the Hope Reef and Main Reef Complexes. Negative shift in MRC is seen in presented values. All Raman spectrometry was performed on Type I and Type II primary FI.

Reef Complex	Disordered-Induced Peak (D)	Ordered Graphite (G)	Overtone of Disordered Band (G')
Hope Reef	1347.88 – 1385.47cm^{-1}	1582.92 – 1600.55cm^{-1}	2690.76 – 2721.62cm^{-1}
Main Reef Complex	1335.91 – 1354.96cm^{-1}	1581.58 – 1587.10cm^{-1}	2698.64 – 2715.94cm^{-1}

Gas phases from HR were analysed and displayed bands of fermi doublet CO_2 at values of 1280.01 to 1280.18 cm^{-1} and 1384.56 to 1384.63cm^{-1}. Bands of CH_4 were present in vapor phases

of FI, showing spectra values of 2903.57 to 2915.3cm^{-1} and 2908.11 to 2911.52cm^{-1}. Unlike the HR, there is a positive shift in first order CH_4 band for MRC and a negative shift in the second order CH_4 band. Limitations with Raman occurred due to the spot size of the laser in relation to the FI size, as well as the over lapping of FI.

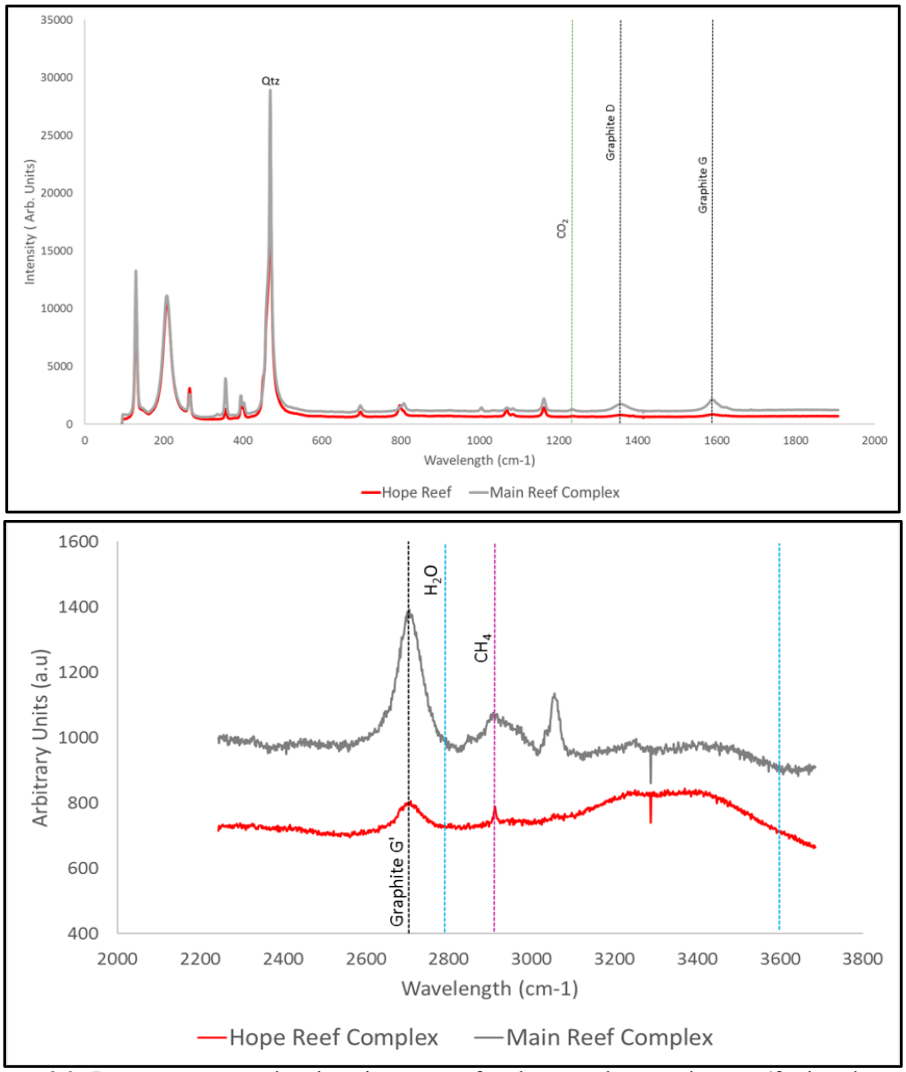

Figure 3.9: Raman spectrum showing signatures of carbon, methane and water (further down the spectrum) in both liquid and vapor phases of fluid inclusions within black quartz veins.

3.5.4 $\delta^{18}O$ stable isotope data

The data from $\delta^{18}O$ stable isotope of both the MRC and HR shows varying ranges. Slightly lower isotopic values are seen in HR, with ranges from 12.85 to 14.30‰. All black quartz samples from MRC show elevated $\delta^{18}O$ values from 14.20 to 14.90‰, with one outlier at 13.75‰. When both the MRC and HR are compared to the Sheba Mine sample, there is a correlation to the values seen at MRC with values ranging in the low to mid-14‰ range. Figure 3.10 shows isotopic values

from this study compared with others in literature at similar deposit types such as (Farber et al., 2016; De Ronde et al., 1992) at the Barberton Greenstone Belt.

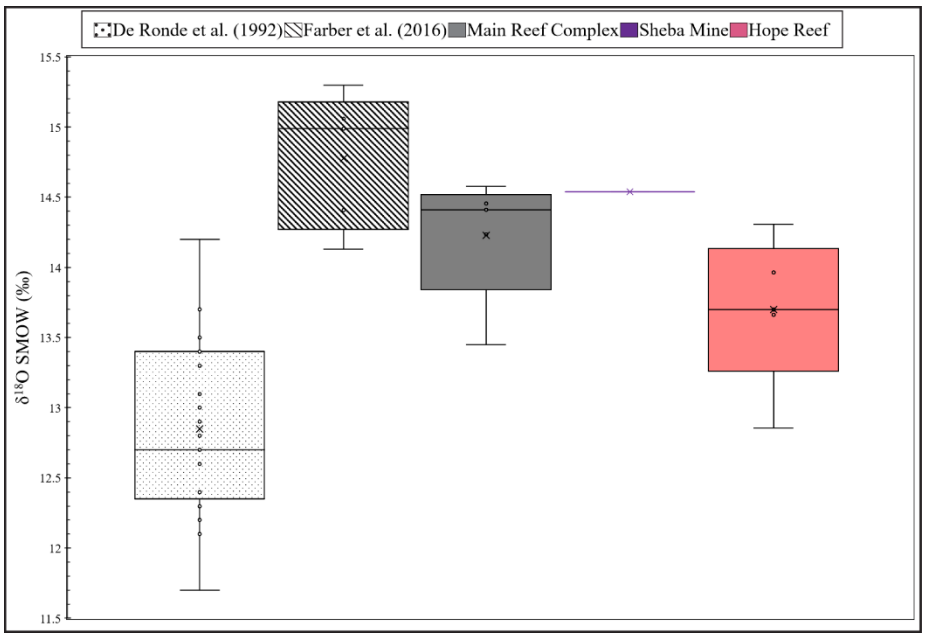

Figure 3.10: $\delta^{18}O$ stable isotope data of samples from this study collected at Sheba/Fairview Mines. MRC and HR compared to other isotopic data collected in similar localities. The data range between 12.85 -14.50‰ for all studies show similar metamorphic signatures for fluid source. For this study the grey box represents MRC samples, light red represents HR and purple indicates samples from the Sheba Mine.

3.6 Discussion

3.6.1 Observed comparisons between the MRC and HR

There are variations seen between the fluids that mineralized the MRC and HR when looking at the data presented in Table 3.4. Primary and secondary fluid inclusions from the MRC and HR display relatively high clathrate melting temperatures (T_{cm}), indicative of a strongly CH_4 enriched fluid (Diamond, 1992; Marshall et al., 2003). Lithological controls are seen in the oxygen stable isotope data showing more elevated values overall in the MRC where graphitic alteration is present in shear zone margins and within the surrounding greywacke-shale units of the Onverwacht and Fig Tree. The presence of graphitic alteration within the MRC is a key difference between the two mineralized reefs.

Table 3.4: Results from both the MRC and HR with listed analytical tests. The structure, lithology, alteration, and gold grade are also incorporated for each reef to represent any similarities or differences that may be present between the MRC and HR.

	Main Reef Complex	**Hope Reef**
Structural Kinimatics	moderate to steeply- SE plunging, characterized by mis-oriented brittle-ductile shear zone within hanging wall	shallow ESE dipping, slightly undulated NNE high-angled brittle-ductile regions
Lithology	Fig Tree and Onverwacht Group	Fig Tree Group
Alteration	graphite-carbonate	sericite-chlorite-carbonate-albite
Gold Grades	>40 to 60g/ton	10 to 20g/ton
Microthermometry		
Primary Fluid Inclusions		
Tm(Ice)	-5.3°C to -12.4°C	-5.0°C to -15.0°C
Th	249°C to 325.6°C(Type I) 168°C to 290°C (Type II)	241°C to 352°C (Type I) 202°C to 340°C (Type II)
Tcm	1.2°C to 18.9°C	8.5°C to 19.5°C
Secondary Fluid Inclusions		
Tm(Ice)	-5.5°C to -12.1	-1.2°C to -10.0°C
Th	227°C to 400°C (Type I) 225.6°C to 372.5°C (Type II)	198°C to 329°C (Type I) 185°C to 297°C (Type II)
Tcm	2.0°C to 14.8°C	7.9°C to 16.0°C
Salinity wt.% NaCl	2.76 to 10.67 wt% (carbonic FI) 8.28 to 16.34 wt% (aqueous FI)	2.43 to 9.19 wt% (carbonic FI) 2.07 to 18.63 wt% (aqueous FI)
Raman Spectroscopy	CH_4,CO_2, H_2O, Graphitic Carbon	CO_2, H_2O, CH_4, Graphitic Carbon
$\delta^{18}O$ Stable Isotope	13.40 to 14.70	12.90 to 14.30

Both reefs show a presence of CO_2, CH_4, H_2O and graphitic carbon, however, there is a stronger elevation and positive shift in the CH_4 and graphitic carbon peaks in the MRC then that of the HR. These Raman differences between the reefs could be due to variations in the oxidation states. The surrounding lithologies of the two reefs could act as a catalyst for graphitization and gold precipitation in the sense of the MRC. In contrast the HR reveals a more oxidized, lower gold grade complex that is devoid of visible graphite. There is also a high degree of disorder within both reefs however, the HR shows a moderately higher degree of disorder then MRC. This disorder difference indicates an overall decrease in the structural disorder and lattice defect in the MRC relative to the HR, however, both reefs show poor crystallinity of graphite. Shifts in the Raman spectrum for quartz bands indicate variations in the mineralizing fluids in both the MRC and HR. Microthermometry experiment results show a similar dataset in the homogenization and freezing temperatures between the MRC and HR; slightly higher homogenization temperatures are present within the MRC in secondary Type I FI, possibly due to an increase in formational

temperatures likely caused by the proximity to the previously active Sheba Fault, rapid faulting and deformational periods.

There are two end-member scenarios that highlight the differences and similarities between the MRC and HR. Firstly, it is possible that there was minimal change in the fluid chemistry throughout the phases of fluid impregnation in both reefs; all variations seen between the MRC and HR would then be a function of variations seen in the wall rock and the reactions between the wall rocks and metamorphic fluids. This scenario can be supported by the differences seen in the lithologies, gold grades, alterations and isotopic values listed in Table 3.4. Fundamental Raman spectroscopy results also support this scenario due to the high degrees of disorder between the MRC and HR that could be a result of P-T variations and carbonic-rich fluid interacting with surrounding host rocks. (Huff and Nabelek, 2007; Hurai et al., 2015; Cloete, 1991; Luque et al., 2014; Wada et al., 1994).

Previous fluid inclusion and isotope work performed on samples from the Fairview Mine by De Ronde et al., 1992 also suggests a low saline, CO_2-H_2O-rich fluid that was likely homogenous throughout the BGB region although may show local heterogeneity within the various BGB mines due to phase separation from fluid wall rock interaction. The structurally bounded HR sits mainly within the Fig Tree with a sericite-chlorite- carbonate-albite-rich alteration; as stated by Goldfarb et al., 2001 when classifying Archean hydrothermal fluids, it is imperative to consider the alteration regimes, the geochemical association of U-Ni-Co-Cr to that of gold, and the relation of gold to mineralized quartz/quartz- carbonate veins. The alteration differences , as mentioned in section 2.4, within the MRC and HR not necessarily a product of heterogeneous fluids, but more likely as a result of fluid and wall rock interaction.

The second scenario is that the observed variations in the MRC and HR are due to physico-chemical differences in the mineralizing fluid as it evolved during the different stages of the late D_3 mineralizing event (i.e., earlier formation of the HR during F_3 folding; later development of the MRC during F_3b folding)(Gloyn-Jones and Kisters, 2018, 2019). It is possible that original mineralizing fluids occurred at slightly lower temperatures, however, the fluid content would have still contained lower salinity, CO_2-H_2O-rich with minor volatiles of CH_4. This can be supported when interpreting microthermometry datasets and fluid inclusions in petrographic analysis. As previously mentioned, primary FIA in MRC samples, form zonation patterns in quartz grain boundaries, however these once primary FIA were previously decrepitated and emptied out. This

skeletal remain of primary FIA could indicate an episodic secondary fluid flow with increased P-T conditions. It is difficult however to conclude the degree of P-T differences between the multiple fluid pulses as the variations in all presented data are minimal. Disordered shifts in the Raman spectroscopy data from both reefs can illustrate the slight variations seen in the MRC verses the HR. This can further be supported from a student t-test of unequal variances. Data from primary and secondary aqueous-rich FI were compared from both reefs based on the temperature of ice melt (Tm_{ice}) and the homogenization temperature (T_h). When comparing secondary aqueous-rich FI from HR to MRC there is a visible difference when testing at a 95% confidence interval. Similarly, secondary clathrate melting and homogenization temperatures tested at 90% confidence presented differences in the data. Lastly, there was a slight increase in the t-critical two- tail value at 90% confidence for primary clathrate melting temperatures when comparing the MRC and HR. All other t-test showed no significant difference when comparing primary and secondary values at 90%, 95% and 99% confidence. Refer to Appendix IV for represented t-test data. This slight variation in secondary FI datasets from the HR and MRC could support the probability for secondary fluids to have much higher P-T conditions and in fact catalyze gold mineralization within the Fairview Mine.

The F_3- F_3b folding event must also be considered when interpreting the possible scenarios that lead to differences seen in the MRC and HR. These late stage folding events, which resulted in a NW-SE trending axial plane F_3b, likely aided in isolating fluid flow up the Sheba Fault to the highly mineralized MRC. This could have deflected fluid supply from the HR and cause part of the NW side of the shallow HR to be pulled up along the MRC (see Figure 3.2).

The probability for the fluids that mineralized the MRC and HR to be meteoric or magmatic is unlikely as the microthermometry and stable isotope data suggest otherwise. Argapami et al., 2018 show slight variations in silver isotopes from the New Consort and Sheba Mine in the BGB and state the unlikelihood those results represent different source fluids, similarly the oxygen stable isotope data in this study is not representative enough to indicate a different fluid source for the MRC and HR.. It is more likely that due to the presence of the Sheba Fault in proximity to the MRC and HR, pervasive hydrothermal fluids pulsated through newly formed fractures giving rise to the mineralized quartz and quartz- carbonate veins seen throughout the two reefs. These fluid pulses with the previously active Sheba Fault exemplify the fault valve model for the Fairview Mine and portions of the BGB (Sibson, 1990; Gloyn-Jones and Kisters, 2018, 2019). Constant

faulting with hydrothermal fluid flow created the series of vein networks that are associated with mineralization (Sibson, 1990). The high-grade envelope at the MRC likely prevailed due to the association between the Fig Trees greywacke and shale to that of the Onverwacht groups talc carbonate schist, serpentinites and intercalated cherts. As suggested in this study, Aragpami et al., 2018 also interprets the contact between the Onverwacht metavolcanics and the Fig Tree metasediments as a dominate pathway for mineralizing fluids to form high grades in the metavolcanics of the Onverwacht and orebody replacements in the Fig Tree metasediments. The formation of large-scale metamorphic mineralizing hydrothermal fluid systems corresponds to dehydration reactions that occur in conditions like those in the transition from greenschist-amphibolite facies, which are remarkably similar to the conditions of gold mineralization (Otto et al., 2007). As stated by Goldfarb, 2017, the more complex and contrasting lithological units, the more ideal of an environment for gold precipitation. High grade regional metamorphism and metasomatism within the surrounding meta-volcanic-sedimentary rocks of the Fig Tree and Onverwacht group would explain how the large volumes of hydrothermal fluids formed (Goldfarb et al., 2001; Altigani et al., 2016). It is determined after interpreting the data from this study there is more plausibility for the fluids that mineralized the MRC and HR to follow the first scenario, that wall rock – fluid interaction are responsible for the gold endowment; however, deformational events, as explained in the second scenario, related to F3 and F3b provided the permeability's for fluid flow. It cannot be explicitly determined whether source of mineralizing fluid and composition is a result of the scenarios separately or a combination of the two. There is not enough detailed high-resolution geochronological data within both the reefs to discredit either scenario.

3.7 Conclusion

Gold mineralization in Archean orogenic gold systems are largely dependent on pervasive fluid flow, the interaction between wall rock and fluid, and the proximity to second and third order structural features (Bierlein and Maher, 2001; Dirks et al., 2013; Altigani et al., 2016). Like the Fairview Mine of the BGB many other orogenic deposits are hosted within quartz and quartz carbonate veins within compressional shear zone regions (Dziggel et al., 2007, 2010; Dirks et al., 2013; Altigani et al., 2016). This study indicates fluids within the MRC and HR to be low to moderate salinity, CO_2-H_2O-CH_4 bearing, and metamorphic fluids, similar to the expected mineralizing fluid types in other orogenic deposits. Pressure and temperature values suggested by

De Ronde et al., 1992 for the Fairview Mine and several other BGB gold deposits range from 300-400°C and approximately 1kbar at depths of 3-4km, which still fall in the overall presumption for gold mineralizing fluids in these deposit types.

It is believed that higher salinities in fluid inclusions likely form as a result of fluid unmixing (Neumayr and Hagemann, 2002; Goldfarb and Groves, 2015), if this is true then it is not plausible that gold mineralization was caused by the mixing and unmixing of two varying fluids within the MRC and HR due to the low salinity values present in the data sets of this study. Even though there are differences mentioned above in the lithologies, gold grades, alterations, and overall timing for both the MRC and HR the data presented in this study supports the idea of a similar parent fluid that has evolved through time during deformational and faulting phases with interaction to the varying wall rocks.

Due to limitations in the sample sets it is not conclusive as to what exactly the gold mineralizing fluids were that mineralized the MRC and HR, nor is it known where the graphitic material, visibly present in the MRC but analytically present in both the MRC and HR through micro Raman spectroscopy, originated. Some of the subtle differences seen in the homogenization temperatures, gold grades, alteration, lithologies, structural fabrics, oxygen stable isotope values, Raman spectroscopy and SEM data are not significant enough to indicate a different parental fluid for the MRC and HR. A larger scale study comparing regions of higher and lower gold grades in surrounding BGB gold deposits will better isolate and understand the fluid types present during the periods of gold mineralization. More detailed analytical test on the graphite present in the MRC shear zones and molecularly in the HR will help delineate how the carbonaceous material came to rise.

3.8 References

Altigani, M., Merkle, R. and Dixon, R., 2016. Geochemical identification of episodes of gold mineralisation in the Barberton Greenstone Belt, South Africa. Ore Geol. Rev. 75, 186-205.

Anhaeusser, C.R., 1976a. The nature and distribution of Archaean gold mineralization in Southern Africa. Miner. Sci. Eng. 8, 46–84.

Anhaeusser, C.R., 1976b. The geology of the Sheba hills area of the Barberton mountain land, South Africa, with particular reference to the Eureka syncline. Trans. Geol. Soc. South Africa.

Anhaeusser, C.R., 1965. Wrench faulting and its relationship to gold mineralization in the Barberton Mountain Land. Inform. Circ. Econ. Geol. Res. Unit, Univ. Witwatersrand, Johannesburg, 24, 25

Anhaeusser, C.R., Robb, L.J., Viljoen, M.J., 1981. Provisional geological map of the Barberton Greenstone Belt and surrounding terrane, eastern Transvaal and Swaziland scale 1: 125,000. Geol. Soc. South Africa.

Argapadmi, W., Toth, E. R, Fehr, M. A., Schönbächler, M., Heinrich, C. A., 2018. Silver Isotopes as a Source and Transport Tracer for Gold: A Reconnaissance Study at the Sheba and New Consort Gold Mines in the Barberton Greenstone Belt, Kaapvaal Craton, South Africa. Econ.Geol. 113(7): 1553–1570. https://doi.org/10.5382/econgeo.2018.4602

Bakker, R.J., 2003. Package FLUIDS 1. Computer programs for analysis of fluid inclusion data and for modelling bulk fluid properties. Chem. Geol. 194, 3-23.

Bierlein F. P., Maher S., 2001. Orogenic disseminated gold in Phanerozoic fold belts: examples from Victoria, Australia and elsewhere. Ore Geol Rev. 18, 11.

Byerly, G., Kröner, A., Lowe, D., Todt, W., Walsh, M. 1996. Prolonged magmatism and time constraints for sediment deposition in the early Archean Barberton greenstone belt: evidence from the Upper Onverwacht and Fig Tree groups. Precambrian Res. 78(1-3), 125-138.

Cloete, M., 1991. Two Cratons and an Orogen. Excursion Guidebook and Review Articles for a Field Workshop through Selected Archaean Terranes of Swaziland, South Africa and Zimbabwe. Department of Geology, University of Witwatersrand, Johannesburg.

Colvine, A.C., 1989. An empirical model for the formation of Archean gold deposits Products of final cratonization of the Superior Province, Canada. Econ. Geo. Monogr. 6, 37-53.

De Ronde, C.E.J., Spooner, E.T.C., De Wit, M.J., Bray, C.J., 1992. Shear zone-related, Au quartz vein deposits in the Barberton Greenstone Belt, South Africa: Field and petrographic characteristics, fluid properties and light stable isotope geochemistry. Econ. Geol. 87, 366–402.

Diamond L. W., 1992. Stability of CO2 clathrate hydrate 1 CO2 liquid 1 CO2 1 aqueous KCl-NaCl solutions: Experimental determination and application to salinity estimates of fluid inclusions. Geochim. Cosmochim. Acta. 56, 273–280.

Dirks, P.H.G.M., Charlesworth, E.G., Munyai, M.R., 2009. Cratonic extension and Archaean gold mineralisation in the Sheba-Fairview mine, Barberton greenstone belt, South Africa. South African J. Geol. 112, 291–316. https://doi.org/10.2113/gssajg.112.3-4.291

Dirks, P.H.G.M., Charlesworth, E.G., Munyai, M.R., Wormald, R., 2013. Stress analysis, post-orogenic extension and 3.01Ga gold mineralisation in the Barberton Greenstone Belt, South Africa. Precambrian Res. 226, 157–184. https://doi.org/10.1016/j.precamres.2012.12.007.

Dziggel, A., Otto, A., Kisters, A.F.M., Meyer, F.M. 2007. Chapter 5.8 Tectono-Metamorphic Controls on Archean gold mineralization in the Barberton Greenstone Belt, South Africa: An Example from the New Consort Gold Mine. Dev. Precambrian Geol., 15, 699-727. https://doi.org/10.1016/s0166-2635(07)15058-1

Dziggel, A., Poujol, M., Otto, A., Kisters, A., Trieloff, M., Schwarz, W., Meyer, F., 2010. New U–Pb and 40Ar/39Ar ages from the northern margin of the Barberton greenstone belt, South Africa: Implications for the formation of Mesoarchaean gold deposits. Precambrian Res. 179(1-4), 206-220.

Fagereng, Å., Remitti, F., and Sibson, R.H., 2011. Incrementally developed slickenfibers—Geological record of repeating low stress-drop seismic events?.Tectonophysics. 510, 381–386. https://doi.org/10.1016/j.tecto.2011.08.015.

Farber, K., Dziggel, A., Meyer, F., Harris, C., 2016. Petrology, geochemistry, and fluid inclusion analysis of altered komatiites of the Mendon Formation in the BARB4 drill core, Barberton greenstone belt, South Africa. South African Journal of Geology. 119. https://doi.org/10.2113/gssajg.119.4.639.

Frezzotti, M., Tecce, F., Casagli, A., 2012. Raman spectroscopy for fluid inclusion analysis. Journal of Geochemical Exploration. 112, 1-20.

Gloyn-Jones, J.N., Kisters, A.F.M., 2018. (in press). Ore-shoot formation in the Main Reef Complex of the Fairview Mine: multiphase gold mineralization during regional folding, Barberton greenstone belt, South Africa. Mineralium Deposita.

Gloyn-Jones, J., Kisters, A., 2019. Ore-shoot formation in the Main Reef Complex of the Fairview Mine—multiphase gold mineralization during regional folding, Barberton Greenstone Belt, South Africa. Mineralium Deposita. https://doi.org/10.1007/s00126-019-00865-9

Goldfarb, R.J., 2017. Gold deposits in metamorphic rocks – what we do know and what still confuses us in 2017. Soc. Of Econ. Geologists Presentation.

Goldfarb, R.J., Groves, D.I., 2015. Orogenic gold: Common or evolving fluid and metal sources. Lithos 233, 2–26.

Goldfarb, R., Groves, D., Gardoll, S., 2001. Orogenic gold and geologic time: A global synthesis. Ore Geology Reviews. 18, 1-75.

Goldfarb, R.J., Leach, D.I., Pickthorn, W.A., Paterson, C.J., 1988. Origin of lode- gold deposits of the Juneau gold deposit, southeast Alaska. Geology 16, 440-443.

Groves, D.I., Goldfarb, R.J., Gebre-Mariam, M., Hagemann, S.G., Robert, F. 1998. Orogenic gold deposits: A proposed classification in the context of their crustal distribution and relationship to other gold deposit type. Ore Geol. Rev. 13, 7-27.

Groves, D., Santosh, M., Goldfarb, R., Zhang, L., 2018. Structural geometry of orogenic gold deposits: Implications for exploration of world-class and giant deposits. Geoscience Frontiers. 9.
https://doi.org/10.1016/j.gsf.2018.01.006.

Harris, C., Vogeli, J., 2010. Oxygen isotope composition of garnet in the Peninsula Granite, Cape Granite Suite, South Africa: Constraints on melting and emplacement mechanisms. South African Journal of Geology. 113.
https://doi.org/10.2113/gssajg.113.4.401.

Hofmann, A., 2005. The geochemistry of sedimentary rocks from the Fig Tree Group, Barberton greenstone belt: Implications for tectonic, hydrothermal and surface processes during mid-Archaean times. Precambrian Res. 143(1–4), 23-49.
https://doi.org/10.1016/j.precamres.2005.09.005.

Hofmann, A., Harris, C., 2008 Silica alteration zones in the Barberton greenstone belt: A window into subseafloor processes 3.5–3.3 Ga ago. Chem. Geol. 257(3–4), 221-239.
https://doi.org/10.1016/j.chemgeo.2008.09.015.

Huff, T.,Nabelek, P., 2007. Production of carbonic fluids during metamorphism of graphitic pelites in a collisional orogen—An assessment from fluid inclusions Geochim. Cosmochim. Acta. 71(20), 4997-5015.

Hurai, V., Huraiová, M., Slobodník, M., Thomas, R., 2015. Raman and Infrared Spectroscopic Analysis. Geofluids, 231–279.

Krolop, P., Burisch, M., Richter, L., Fritzke, B., Seifert, T., 2018. Antimoniferous vein-type mineralization of the Berga Antiform, Eastern-Thuringia, Germany: A fluid inclusion study. Chem. Geol.
https://doi.org/10.1016/j.chemgeo.2018.02.034.

Lowe, D.R., and Byerly, G.R., 1999, Stratigraphy of the west-central part of the Barberton greenstone belt, South Africa, in Lowe, D.R., and Byerly, G.R., eds., Geological Evolution of the Barberton Greenstone Belt, South Africa: Geological Society of America Special Paper. 329, 1–36.

Lowe, D.R., Byerly, G.R. 2007. An Overview of the Geology of the Barberton Greenstone Belt and Vicinity: Implications for Early Crustal Development. Precambrian Geol. 15, 481-526.

Luque, F., Huizenga, J., Crespo-Feo, E., Wada, H., Ortega, L. Barrenechea, J., 2014. Vein graphite deposits: geological settings, origin, and economic significance. Mineralium Deposita. 49(2), 261-277.

Marshall D., Groat L., Giuliani G., Murphy D., Mattey D., Ercit T.S., Wise M.A., Wengzynowski W., Eaton W.D. 2003. Pressure, temperature and fluid conditions during emerald precipitation, southeastern Yukon, Canada: fluid inclusion and stable isotope evidence. Chem. Geol. 194:187-199.
https://doi.org/10.1016/ S0009-2541(02)00277-2

Munyai, M.R., Dirks, P.H.G.M., Charlesworth, E.G., 2011. Archaean gold mineralisation during post-orogenic extension in the New Consort gold mine, Barberton greenstone belt, South Africa. South African J. Geol. 114, 121–144.
https://doi.org/10.2113/gssajg.114.2.121

Neumayr, P., and Hagemann, S., 2002. Hydrothermal fluid evolution within the Cadillac tectonic zone, Abitibi greenstone belt, Canada: Relationship to auriferous fluids in adjacent second and third-order shear zones. Econ. Geol. 97, 1203–1225.

Otto, A., Dziggel, A., Kisters, A. and Meyer, F. 2007. The New Consort Gold Mine, Barberton greenstone belt, South Africa: orogenic gold mineralization in a condensed metamorphic profile. Mineralium Deposita. 42(7), 715-735.

Prezbindowski, D., Larese, R., 1987. Experimental stretching of fluid inclusions in calcite---Implications for diagenetic studies. Geology. 15.
https://doi.org/10.1130/0091-7613(1987)15<333: ESOFII>2.0.CO;2

Ramsay, J.G., 1963. Structural investigations in the Barberton Mountain Land, Eastern Transvaal. Trans. Geol. Soc. South Africa 66, 353–401.

Robertson, M.J., Charlesworth, E.G. and Phillips, G.N. (1994). Gold mineralization during progressive deformation at the Main Reef Complex, Sheba Gold Mine, Barberton Greenstone Belt, South Africa. Exploration and Mining Geology, 3, 181–194.

Roedder, E., 1984. Fluid inclusions. Rev. Mineral. 12.

Sibson, R.H., 1990. Rupture nucleation on unfavorably oriented faults. Seis. Soc. Am., 80, 1580-1604.

Steele-MacInnis, M., 2018. Fluid inclusions in the system H2O-NaCl-CO2: An algorithm to determine composition, density and isochore. Chem.l Geol. 498, 31-44. https://doi.org/10.1016/j.chemgeo.2018.08.022

Steele-Macinnis, M.J., Bodnar, R.J., Naden, J., 2011. Numerical model to determine the composition of H2O–NaCl–CaCl2 fluid inclusions based on microthermometric and microanalytical data. Geochim. Cosmochim. Acta. 75, 21–40.

Steele-MacInnis M.J., Lecumberri-Sanchez P., Bodnar R. J., 2012. HOKIEFLINCS-H2O-NACL: A Microsoft Excel spreadsheet for interpreting microthermometric data from fluid inclusions based on the PVTX properties of H2O–NaCl. Comput. Geosci. http://dx.doi.org/10.1016/j.cageo.2012.01.022.

Tomkins, A.G., 2013. A biogeochemical infl uence on the secular distribution of orogenic gold: Econ. Geol. and the Bull.of the Soc. of Econ.Geol. 108, 193–197. doi:10.2113/econgeo.108.2.193

Wada, H., Tomita, T., Matsuura, K., Tuchi, K., Ito, M., Morikiyo, T., 1994. Graphitization of carbonaceous matter during metamorphism with references to carbonate and pelitic rocks of contact and regional metamorphisms, Japan. Contributions to Mineralogy and Petrology. 118(3), 217-228.

Wiggett, B.S.C., Brink, W.C.J., Vorster, M.A., 1986. The Fairview gold mine, Barberton greenstone belt, in: C.R. Anhaeusser and S. Maske (Eds.). Miner. Depos. South. Africa 1, 169–179.

Chapter 4: Technical aspects and methodology for conducting fluid inclusion research in the new Microthermometry Lab at Department of Earth Science, Stellenbosch University

This chapter includes a suggested methodology for fluid inclusion studies as well as a laboratory manual, an effort on how to conduct freezing and homogenization experiments using the Linkam THMS600 stage. The methodology included has been modified from a basic fluid inclusion study. More precautionary steps have been added in the early stages of sample collecting, sample cutting and preperation of chips for microthermometry experiments. These added steps are suggested in efforts to reduce mishandling of samples and losing sample orientation. The modified methodology also focuses on detail of FIA mapping, observations, and notes taken during microthermometry experiments to ensure accurate data is collected. The methodology explained in this chapter was utilized in the study from Chapter 3. The laboratory manual was developed to guide those who are uninformed but are interested in performing freezing and homogenization experiments. This chapter takes the place of a methodology section seen in a traditional thesis. The reader is referred to Roedder, 1984; Bodnar, 1994; Bakker and Thiery, 1994; Roedder and Bodnar, 1997; Bodnar, 2003, for a more in-depth description of fluid inclusions, analysis techniques and to assist with making interpretations with microthermometry data.

4.1 Introduction

Fluid phases present during the time of crystal growth may become trapped imperfections which form small vacuoles termed fluid inclusions (FI) (Bodnar, 2003). Unveiling the history of fluids in geologic systems is essential for understanding the types of fluids responsible for ore formation. Through studying fluid inclusions, made up of a combination of liquid, vapor, and solid phases, light can be shed on the composition of these mineralizing fluids. This provides insight into the conditions of formation, including the temperature of fluid systems, pressure of the systems, salinity of aqueous fluids and the composition of gas in the fluids. All in all, studying such microscopic time capsules presents us with a better understanding of the development of similar ore-forming systems worldwide. The use of various geochemical analytical techniques such as microthermometry, Raman micro spectroscopy, laser ablation inductively coupled mass spectrometry (LA-ICPMS), acoustic decrepitation and crush leach, all provide answers to the composition of constituents present within fluid inclusions.

4.2 Sample preparation

4.2.1 Selecting samples

When conducting a fluid inclusion study, it is imperative to understand the samples you are working with and to ensure they contain visible fluid inclusions. Several rock-forming minerals are particularly suited to preserve fluid inclusions, such as, quartz, fluorite, halite, calcite, apatite, dolomite, sphalerite, barite, topaz, and cassiterite, to name but a few. Thin sections (30µm) used for routine petrographic analysis are also suitable for identifying the presence of fluid inclusions in selected samples. However, for further advanced inclusion studies, it is essential to have samples prepared into double polished thick sections, with thicknesses of about 100µm. This thickness can vary depending on the opacity of the sample. The clarity of fluid inclusions when evaluating them petrographically is only as good as the polishing job done to make them into thick sections, therefore it is crucial to assure a proper polishing technique is used. Refer to (Goldstein, 2003) for further information on double polished thick section procedures.

Non-foliated, igneous rocks in some cases make it challenging, or impossible, to collect oriented samples. However, it is still crucial to document any structural features and rock fabrics that may help with understanding geochemical and structural relations for the study area (Lespinasse and Pecher, 1993). Geometrical information collected at sample sites provide a bigger illustration to microstructures that may be present in fluid inclusion planes adding evidence to "fluid inclusion association" as termed by (Goldstein, 2001). Fluid inclusion generations are sometimes comparable to rock evolution because FI usually form around the same time as the host lithologies (Van den Kerkhof and Hein, 2001).

When collecting samples such as drill cores or other in situ-oriented samples, maintain orientation direction by marking it on the sample with a marker and photograph the sample in place with an object for scale it with. These marked orientations will come in handy later when cutting samples into billets for thick sections. If samples cannot be oriented, e.g. samples are in a vein on the roof of an underground mine, then mark the general trend of the feature and take orientations of nearby features. Keeping the original orientation of samples is critical, due to these structural features being indicative directions of flow through veins and such (Touret, 2001).

4.2.2 Thin sections

Preparing samples into thin sections is one of the most important parts of any fluid inclusions study. After samples are selected, they need to be cut into billets (2-5cm thick). Photographs should be taken of the sample, also indicating the orientation of any structural features, before cutting any sample. Samples should be cut following structural features while maintaining orientation of the respective cuts. If working with a whole rock, e.g. bull quartz, locate any crystal faces in the sample and cut perpendicular to the c-axis of the crystal boundaries. A perpendicular cut on the c -axis allows for a better visibility of primary fluid inclusions (see Figure 4.1).

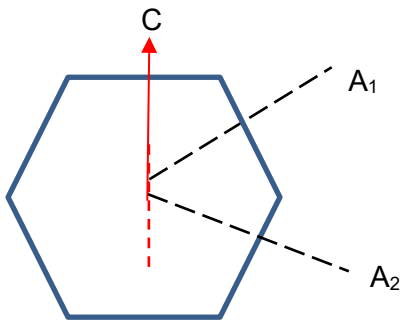

Figure 4.1: Illustration of a perpendicular cut on the C-axis of a quartz crystal. This dissects the crystal exposing primary inclusions that may be present along the A_1, A_2 and A_3 faces.

After cutting samples into desirable billets, double polished thick sections can be made. Double polished thick sections range from 50-600µm in thickness. The double polished sides allow for optimal viewing through samples. It is important that when samples are prepared, they are glued to glass slides with an acetone removable glue.

4.2.3 Petrography

Petrography is the most critical part of a fluid inclusion study. Mineral assemblages need to be identified along with any clues to help develop a paragenetic sequence for mineral formation. Furthermore, the types of FI presence in each thick section must be identified and mapped. It has been stressed by Roedder and Bodnar, 1997 to assume all fluid inclusions are secondary until further evidence proved otherwise. When attempting to find FI in a sample it is best to look within grains of the analyzed mineral. It may be challenging to locate FI in low magnification, however,

always start at a lower magnification to find a mineral grain then increase the microscope magnification. At a high magnification you may be able to start seeing FI in clusters within a mineral grain. These clusters are usually made up of fluid inclusion assemblages (FIA). A FIA is a lineation or trail of FI that have formed at a similar time. There are three different types of FIA; primary, secondary, and pseudo secondary.

Primary fluid inclusions occur at the time the crystal grain has formed and can be seen outlining the crystal growth boundaries. Primary inclusions can also appear as zoned regions in a mineral grain or as isolated inclusions. In some cases, primary FI will be irregular in shape or decrepitated or breached making them not viable for further analysis, this can however be true for all three FIA types. It is debated that primary fluid inclusions represent the main mineralization events in ore deposits, however contrary to that belief, all inclusion types are important to note in a study.

Secondary inclusions occur after the growth of the crystal during a remobilization or secondary fluid phase event. These inclusions can be seen cutting completely across a crystal grain

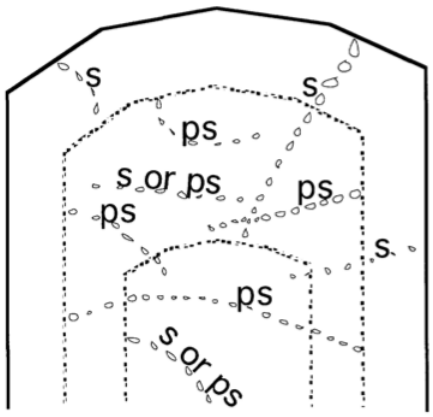

Figure 4.2 : This is an example of primary, secondary and pseudo secondary fluid inclusions and where they form in a crystal. Image was taken from Bodnar, 1994.

boundary. In some cases, secondary fluid inclusions are more representative to ore mineralization due to metamorphic, deformation and alteration events (Fagereng et al., 2011). The third type of fluid inclusions are pseudo-secondary fluid inclusions, which occur during primary crystal growth, during an altering event that may cause fracturing within a primary crystal grain. Pseudo secondary FI are usually not analyzed by researchers due to the controversy of their time frame of origin. See Figure 4.2 for examples of all three fluid inclusion types.

Type	Physical State		Composition	Examples	Size µm
I	Liquid-rich, two-phase	L + V	L >50%		2-10
II	Vapor-rich, two- phase	V + L	V=50 to 80%		2-8
III	Monophase liquid/vapor	L/V	NA		<2
IV	Multiphase	L+V+S	S<20%	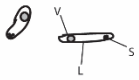	5-12
V	Decrepitate/breached	NA	NA		~8-10

Table 4.1: Shows the type of fluid inclusions present in a study and distinguishes the physical states, volumetric proportion for each phase and provides examples on the morphology of each type.

Proper petrographic analysis includes sketching the mineral grain that harbor the studied fluid inclusions. The first recommendation would be to use a slide scanner or camera to take a photo of the double polished thick section in order to map out desired FI. Note the minerals associated with the FI and the types of FI present (primary, secondary, or pseudo-secondary). Make notes on what you are seeing. Explain what morphology the FI have, the orientation of an FIA trail (if there is any), the abundance of FI in a grain, and the physical state of each FI. Table 4.1 illustrates the types of inclusions seen in the previous chapter. This table is a good example on how to categorize FI. Look for any unique features that may be present in FI and FIA such as necking down, daughter crystals, trapped solids, Brownian motion or decrepitation.

As it is important to photograph the petrographic observations, the same goes for FI studies. Photomicrographs at different magnifications and of any present anomalies will help form a more detailed argument for the overall research question. Take images of thick sections on the microscope of minerals, textural variations of minerals, fluid inclusion types and FIA trails. Be sure to incorporate a scale bar in all selected images. See Figure 4.3 for an example layout of petrographic images showing important features present within a thin section.

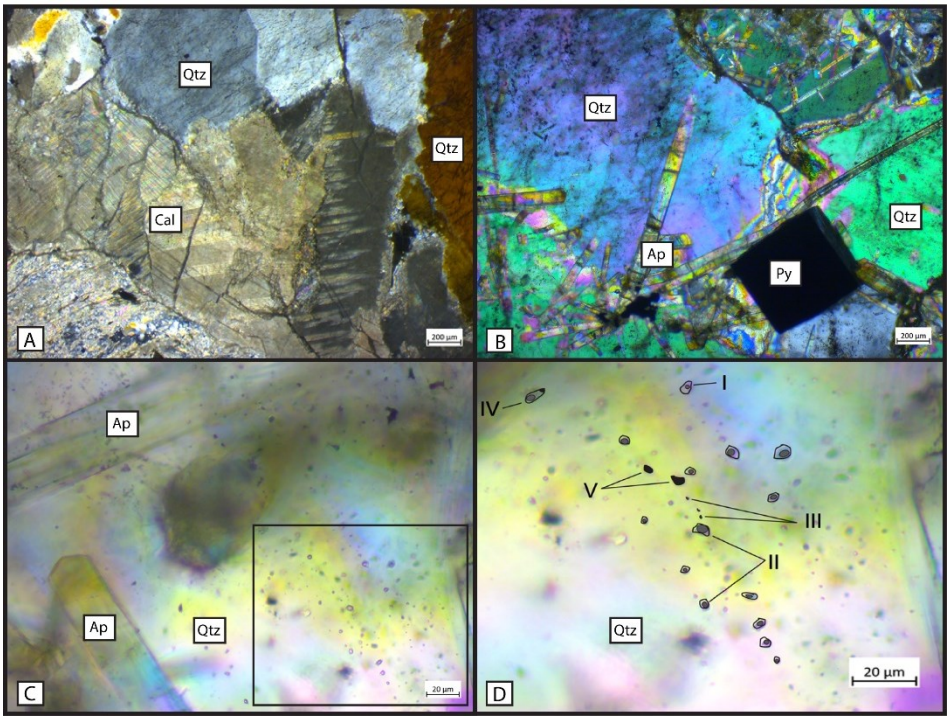

Figure 4.3: Example of petrographic images with labeled mineral assemblages and outlined fluid inclusion types with scale bar.

4.2.4 Detaching sample

Once all petrography has been completed and fluid inclusions have been observed in thick sections, the sample can be prepared for microthermometry experiments. The sample must be separated from the glass in order to conduct heating and freezing experiments. Allow thick sections to be submerged in acetone for 24-48 hours to remove the sample from the glass slide

The following step requires carefully breaking the detached sample into chips to fit into the sample holder on the Linkam stage (see Figure 4.5 C). The smaller the sample the more ideal, as it is **a smaller surface area for the stage to heat and cool, making temperature readings more accurate**. Label chips and samples with noted orientation by tracing the sample. Using a tungsten carbide scriber, gently etch the desired region of the sample to form into a chip. After each chip has been made it is beneficial to map out FIA for each chip to assist with microthermometry experiments. Chips that contain enough fluid inclusions for further analysis should be separated from the main sample and properly label, Figure 4.4A.

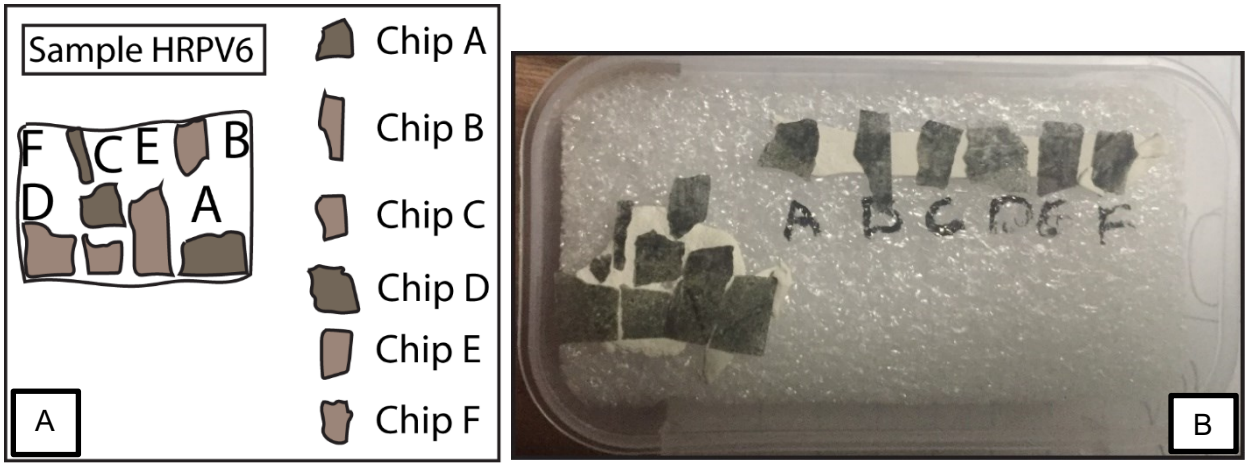

Figure 4.4: A) Double polished thick section prepared for dilution with ethanol. B) To reduce the evaporation rate of the ethanol the samples were placed in a plastic resealable bag. C) The outline for the desired chips to be made from the detached sample after it has been saturated in ethanol.

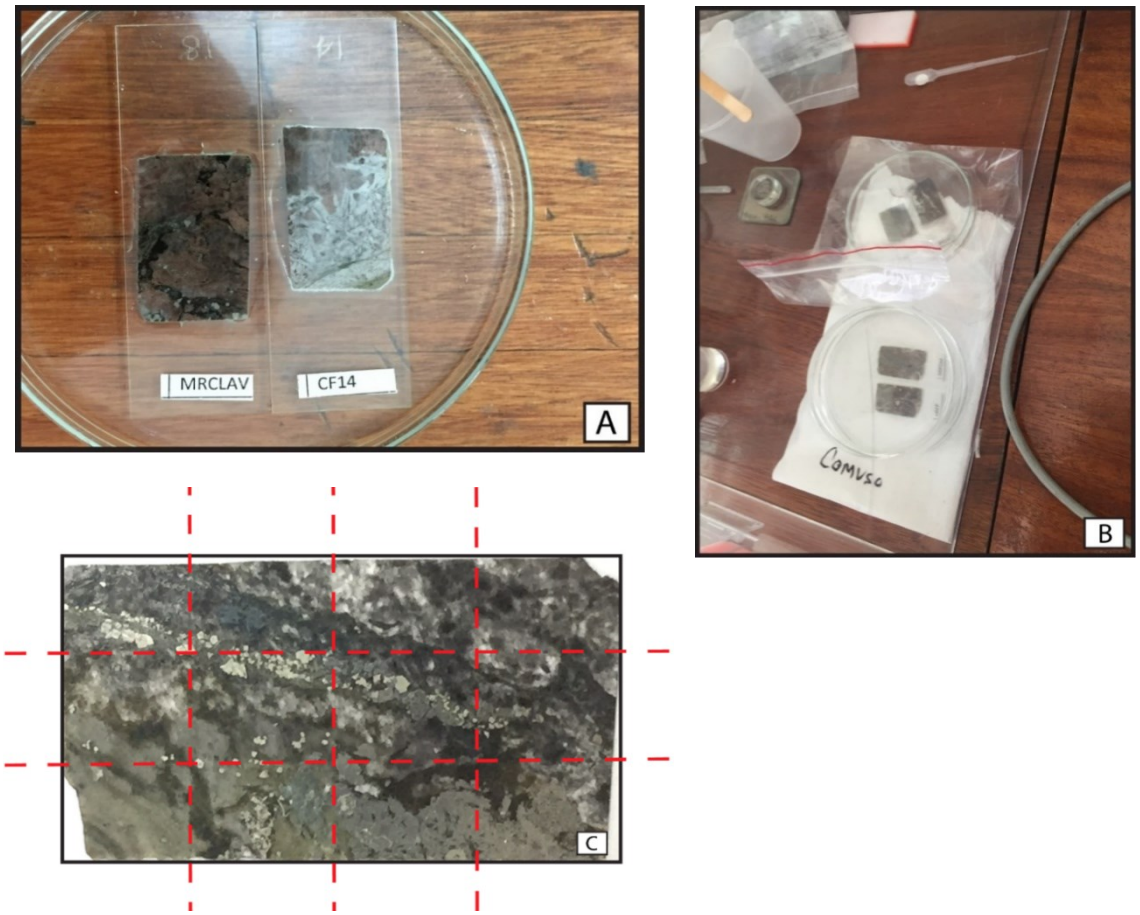

Figure 4.5: A. Schematic drawing of sample chips in orientation as whole sample. B. Structurally oriented samples should be stored in a container to protect from debris and in such a way that will preserve the orientation of the precut thick section.

4.3 Microthermometry experiments

4.3 Equipment

Room 2021 is equipped with a Linkam THMS600 stage with a T95 Controller and LNP95 liquid nitrogen cooling pump. This temperature controlling system allows for precise thermal measurements for fluid inclusion studies. The Linkam THMS600 stage can reach a maximum temperature of 600˚C with a maximum heating rate of 150˚C/min. Freezing experiments are preformed using the T95 Controlling System and the LNP95. This can reach a minimum temperature of -196 ˚C.

Liquid nitrogen is used to cool the stage and the sample within the thermal block. The liquid nitrogen is held in a 1-liter dewer (00) that feeds to the liquid nitrogen cooling connecter (11). N_2 gas is fed through the stainless-steel cooling tube (13) and then into a plastic tube where it is clipped to the top of the stage window (17). This reduces condensation that forms during freezing experiments.

The heating element carrier assembly (2) is connected to the heating element wires (12) where it directs the heat to the 22mm diameter pure silver heating block (14). The platinum temperature sensor (16), located on the side of the silver heating block, registers the current

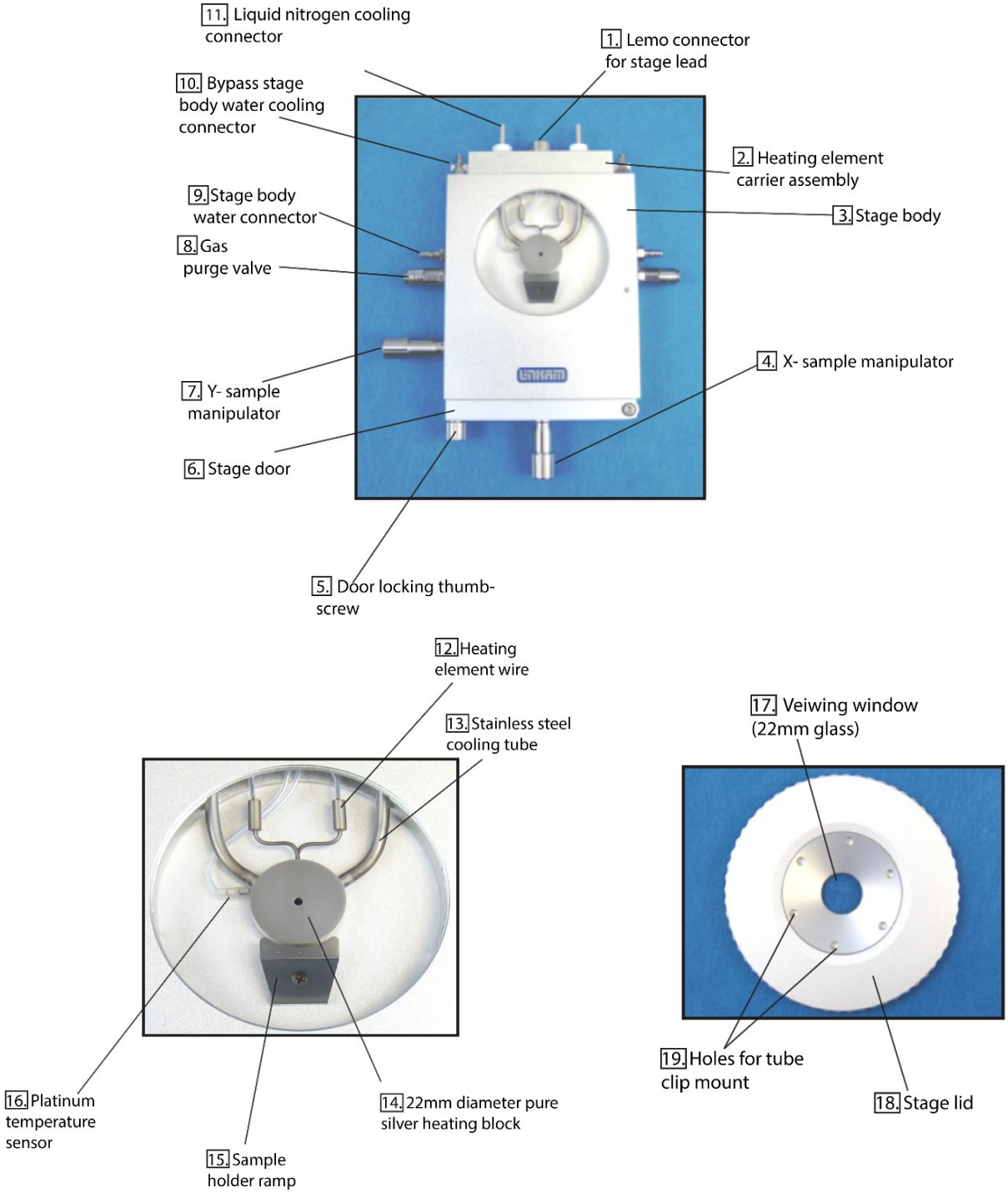

Figure 4.6: Labeled parts of the Linkam THMS600 stage. Image has been modified from the Linkam instruments owner's manual.

temperature of the sample chamber. The heat is sourced from the stage lead and the lemo connector (1). The THMS600 stage is mounted to an Olympus BX53 halogen light microscope with long working distance plan fluorite lens in 10X, 50X, and 100X**. Setting the stage to a microscope is done by a trained technician to ensure all connections are correct**. Attached to the eye piece is a 2x magnifier which allows for double the zoom for each lens when the lever is engaged. The polarizer was removed in order to attach the double magnifier to allow for better visual of small fluid inclusions. The stock condenser was switched with a long working distance condenser. After swapping out the Uplan lens that came with the scope for the long working distance fluorite lens, both the stock and long working condenser ended up being suitable for working with fluid inclusions on this setup. Figure 4.7 illustrates the working distance of the stage to the lens and shows how the long working distance lens are important for viewing samples due to the various glass layers the light must penetrate before being seen through the optics.

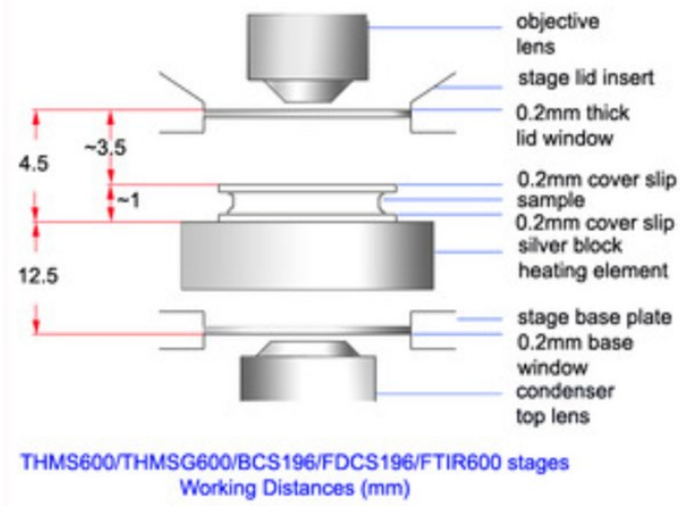

Figure 4.7: Working distance of the THMS600 Linkam stage. This illustrates the layers of the stage and components that make it up. Image provided by Linkam Instruments owner's manual.

A C-mount camera is attached to the top of the eye piece where it then connects to the computer for live footage of the image seen through the scope. Heating and freezing experiments, as well as camera visual, are completed through the LINKS package which is issued with every Linkam stage purchase. The LINKS software also provides real time temperature charts that record every temperature fluctuation with its corresponding rate. Pictures have a scale bar that must be programed in correspondence to the lens on the microscope. Experiments and photos can be saved and exported.

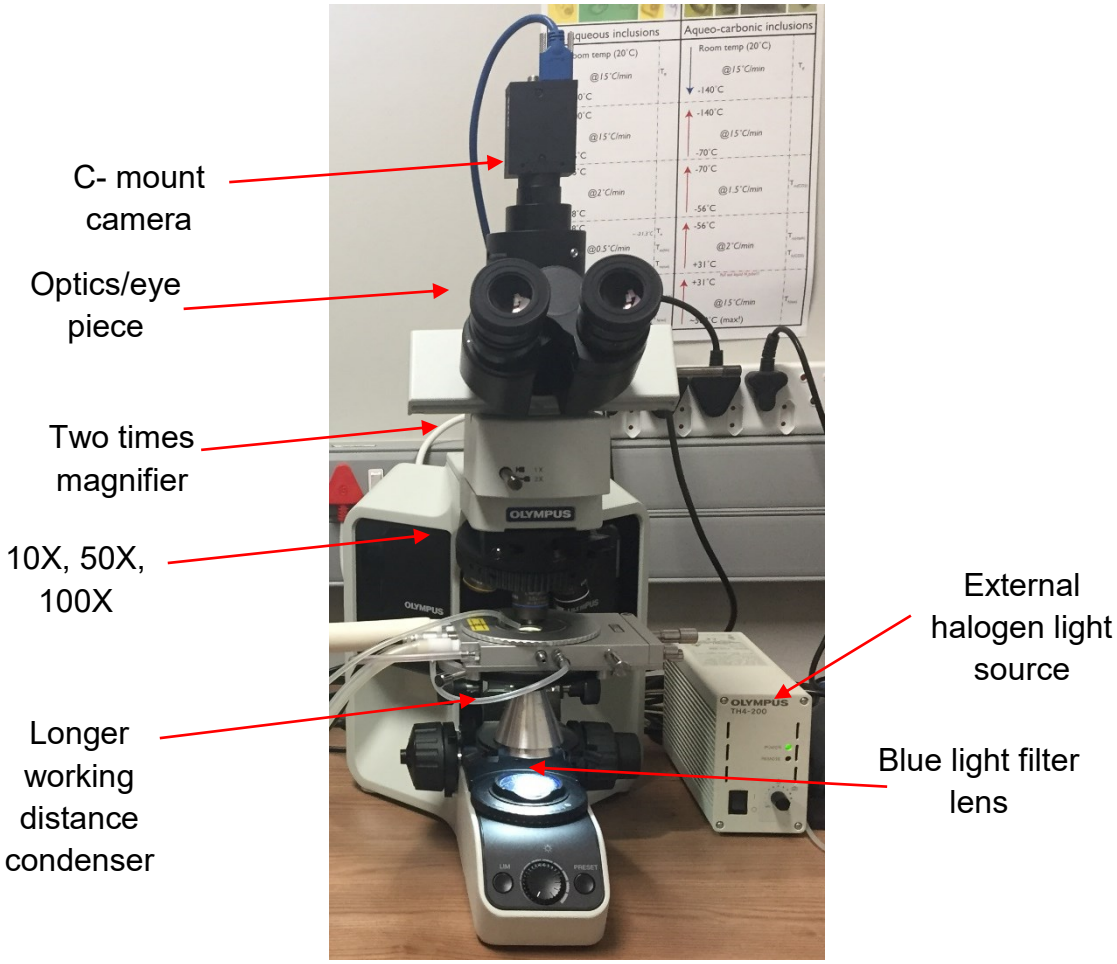

Figure 4.8: Labeled parts of the Olymphus BX53 petrographic microscope for which the Linkam stage is attached.

4.3.1 Setup

Liquid nitrogen can be collected from the chemistry department with the one-liter Nalgene dewer. (**Never use the Linkam dewer to collect liquid nitrogen!**) The glass barrier within the Linkam dewer is fragile, therefore, it should never be used for transporting liquid nitrogen. After collecting the liquid nitrogen, detach the Linkam dewer lid and remove the hose line from the stage to reduce stress on the lines and tubing on the dewer lid. Carefully lift the Linkam dewer off the table and gently place it on the floor to load with liquid nitrogen. (**Never fill Linkam dewer on the table near the Linkam system!**) If there are residual water droplets in the bottom of the Linkam dewer, wipe them out with a clean cloth. (**Never tip or hold the Linkam dewer upside down, as the inner glass will fall out and break!**)

Once the Linkam dewer lid is detached and the dewer is placed safely on the floor, the liquid nitrogen can now be poured into the Linkam dewer. Fill the Linkam dewer up to the groove within the glass barrier. **Do not fill above this line,** as it will make closing the dewer difficult and may damage the setup. Allow the excess gas to evaporate and wait till the liquid is no longer bubbling intensely. The dewer can then be carefully placed back on the table near the stage. Check the screen on the tip of the metal siphoning tube connected under the dewer lid before placing it into the liquid nitrogen. Sometimes debris can gather and clog the line which will put strain on the liquid nitrogen pump. Refer to Figures 4.8 and 4.9 for labeled parts of the Olympus BX53 microscope and the Linkam heating and freezing stage.

4.3.2 Starting the machine

To start up the machine, be sure the liquid nitrogen dewer is filled, with all lines properly connected and the computer turned on. Next, turn on the top Linkam power supply box till the light in the front turns on blue. Then turn on the bottom box which is the pump that feeds the liquid nitrogen and heat to the stage. After both boxes have been turned on, open the LINKS software on the computer. Look for the controller icon at the top left of the screen, scroll to devices then over to “USB device”, (See Figure 4.10). At this point you should see the temperature of the system pop up on the control panel. To connect the camera, go to the icon at the top left and select camera then on the drop down select the preferred camera source.

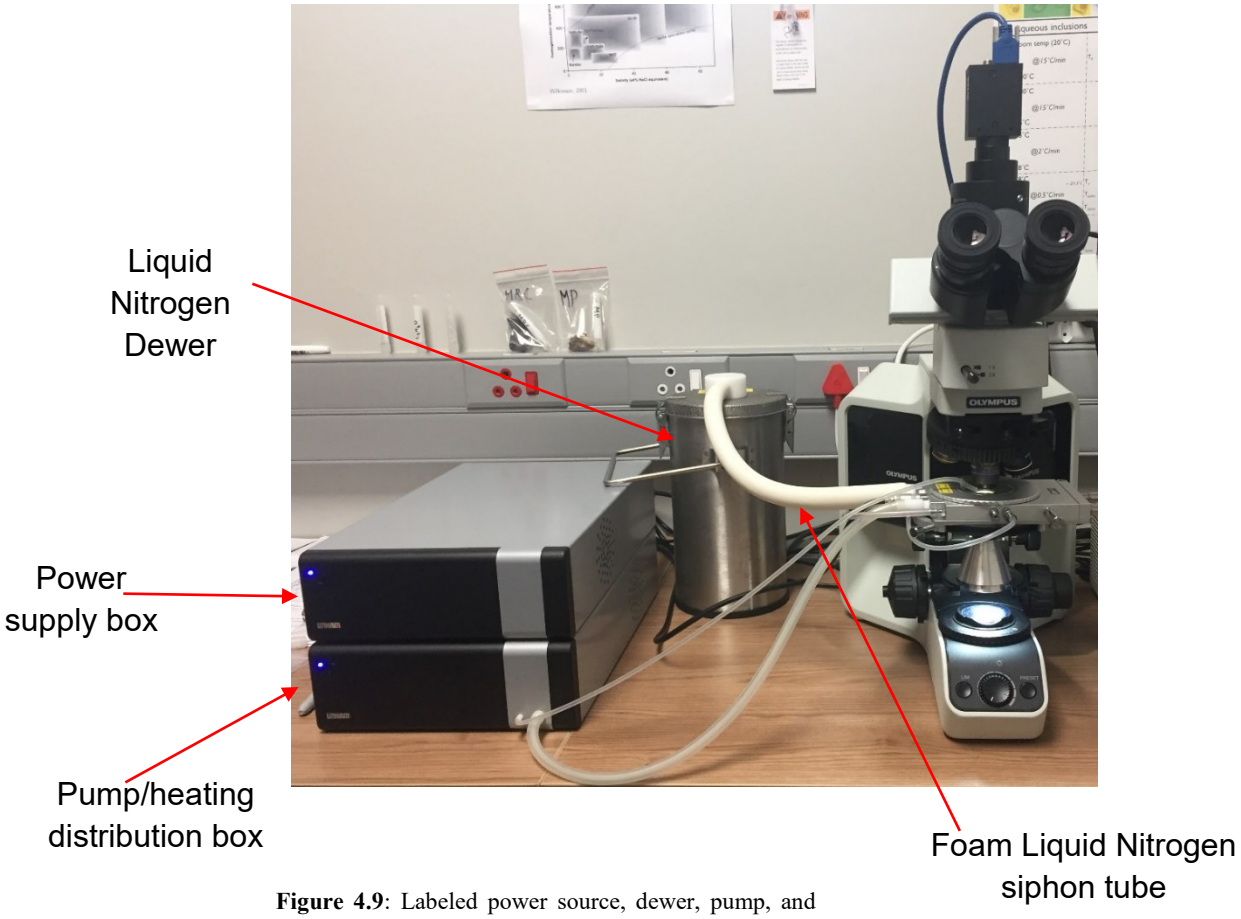

Figure 4.9: Labeled power source, dewer, pump, and dewer line of setup.

Before preforming any experiments record name, date, amount of liquid nitrogen collected, the first temperature displayed on the screen when the system is connected, and any issues that occur with the machine during the time of use. Keep a detailed log of all occupants in the fluid inclusion laboratory, this acts as a reference in the future in case there are any issues with the systems or if the researcher needs to refer to their experiments.

Once the system is turned on, the sample can be prepared for loading in the stage chamber. There are various types of sample holders; one is a 16mm quartz crucible, which is used for liquid or powder samples. There is also a 13 mm quartz cover and a smaller 7mm quartz cover slip, which is ideal for heating experiments since it allows the silver heating cap to cover the sample.

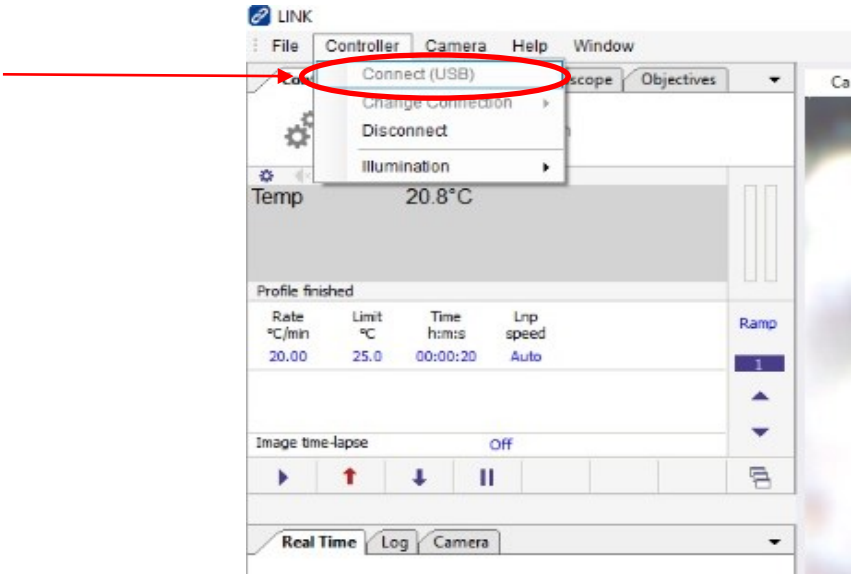

Figure 4.10: Starting the system using the LINKs software. In order to connect the stage to the computer software the system needs to be connected.

To load the sample, gently unscrew the top stage cover (18) (see Figure 4.6). Do not touch the glass with your fingers. Place a clean sample chip on the glass coverslip and make sure it is centered with the light and the metal sample holder ring. Oils from the skin can cause issues during experiments, such as poor visibility and skewing temperatures. The sample chips can be cleaned by using a cotton swab and diluted ethanol. Look through the optics to see that the chip is viewable before closing the silver chamber cover and the stage lid.

If the sample chip is viewable, place the silver temperature regulator cover over the sample and glass coverslip assuring the side of the cover with a gap is aligned with the heating/freezing arm. This will assure you can move the sample freely around with the X and Y axis manipulators (4 & 7) (see Figure 4.6), while the chamber is closed. Once the sample is loaded correctly, locate an area of interest for running analysis and carefully note and map visible FI and FIA.

If the chip has been previously mapped before preforming microthermometry experiments, then the desired areas with fluid inclusions can be navigated to using the X and Y axis sample manipulators. It is in best practice to examine each chip to insure there are plenty of visible fluid inclusions for proposed experiments. The ideal size for microthermometry work is with fluid inclusions roughly 15µm or greater; however, in most cases fluid inclusions will be 5µm or less. These size limitations make it very difficult to see the phase changes during freezing and homogenization experiments, which is why samples should be chosen carefully.

There are never too many fluid inclusions to analyze, however the accuracy of data is more important than an abundance of varying data points. A good sample size to aim for when examining fluid inclusions is at least one hundred FI. This can heavily depend on the size of the inclusions, as with larger inclusions, more data will be available over smaller inclusions where the phase's changes may be difficult to see.

4.3.3 Interpreting sample chips

Before preforming freezing and homogenization experiments locate all prospective fluid inclusions in each chip. Using the grid made from the sample chipping process, proper note taking should be completed to illustrate areas on each chip that fluid inclusions were examined, see Figure 4.11. This will make it easier to refer back to for further analysis.

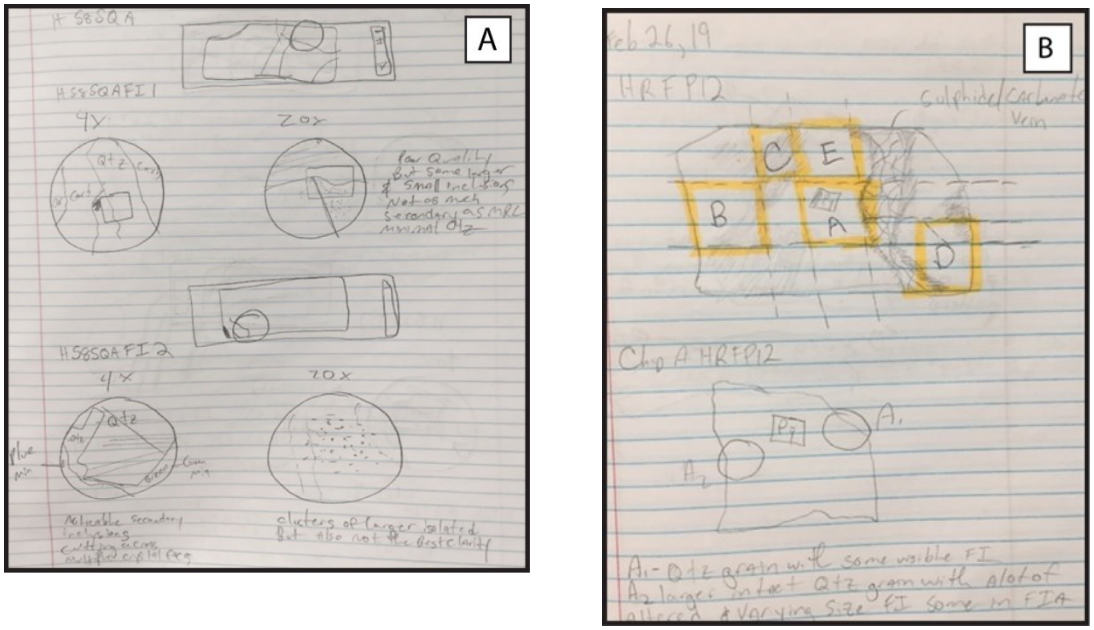

Figure 4.11: A. Example of notes during thin section mapping before detached from glass slide.
B Sketch's and notes for oriented chips from detached sample. Regions of viable FI are circled and documented.

When microscopically evaluating FI and FIAs it is essential to assess the physical states present in each. Using the volumetric estimation chart from Roeddar, 1984 (Figure 4.12), the average percent for each phase can be interpreted. This value will be useful when calculating for density and salinity.

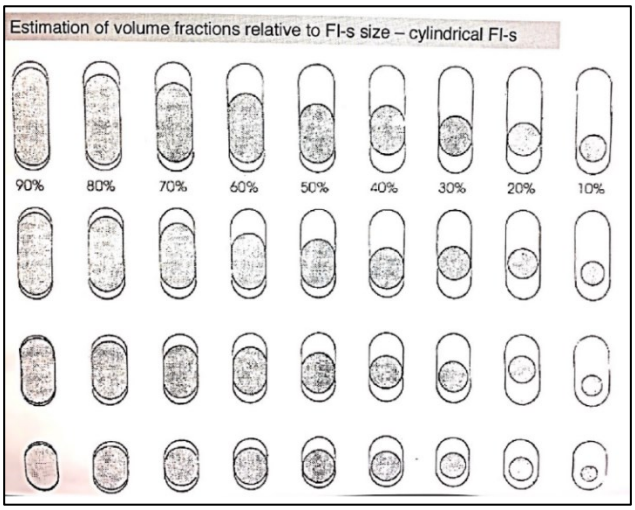

Figure 4.12: Chart of the estimated volume fractions related to the size of examined fluid inclusions and the shape. This image is used to note the liquid to vapor proportions of fluid inclusions. Image provided by Roedder, 1984.

4.4 Performing Experiments

4.4.1 Freezing experiments

Before running any sample, it is important to have a spreadsheet set up to record data in a well-organized manner, as seen in Figure 4.13. More importantly, remember that **freezing experiments are always to be performed first**. This will reduce the chances of re-equilibration, decrepitation, or emptying out of the fluid inclusions that may occur if homogenization experiments are done first. To start with freezing experiments the Rate (˚C/min), Temperature Limit (˚C), and Time (hh:mm:ss) needs to be manually inputted (Figure 4.14).

Sample	Chip	Inclusion Type	Primary/ Secondary	Size (µm)	Vapor volume (%)	T_e	$T_{m(hh)}$	$T_{m(ice)}$	T_d	$T_{m(clath)}$	$T_{h(CO2)}$	$T_{h(CO2)\ phase}$	$T_{h(Total)}$	$T_{h(Total)\ phase}$	Salinity (wt.% $NaCl_{equiv.}$)	Density (g/cm^3)	Notes

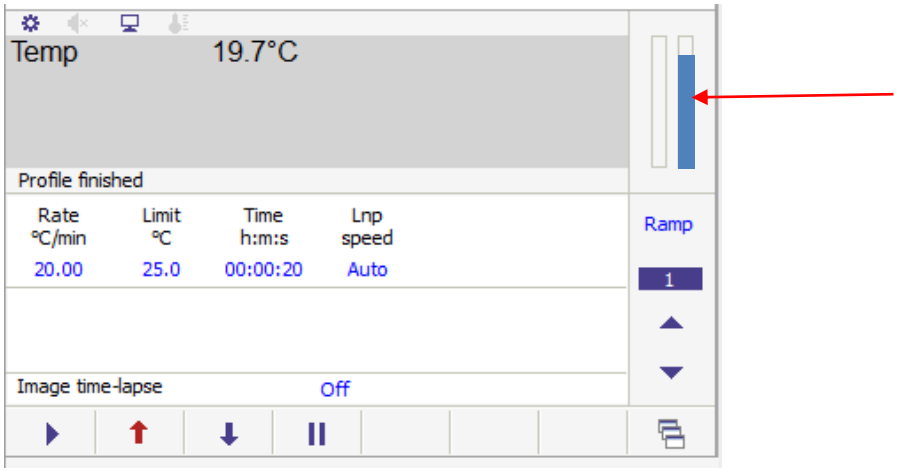

Figure 4.15: The blue bar indicates a liquid Nitrogen pump working too hard, potentially damaging the system.
.

You will see when the FI sample is frozen because it will become sharper around the liquid and vapor bubble; refer to Figure 4.16 as an example of the outline of a FI sharpening when freezing. Another sign which indicates the sample has frozen, is the presence of ice crystals or newly formed solids. Once the max freezing temperature has been reached, the sample will now have to slowly be heated to room temperature to get the first melting temperature (T_mI), temperature of final melting (T_mice), eutectic melting (T_e), and the clathrate melting temperature (T_{cm}). As mentioned during freezing, fluid inclusions may form solid crystals such as halite or ice crystals. Upon reheating to room temperature, ice crystals will melt. The temperature at which ice crystals melt T_mice is a critical data point, because it is used to find the salinity of the solution. This temperature will mainly be found in aqueous-rich inclusions with low amounts of complex volatiles. A trick to help indicate the Tm_{ice} is to slow the rate on the controller down to 2 ˚C/min when you reach -20˚C. If ice melts are present, they will usually occur at temperatures between -20 ˚C and 0 ˚C. The eutectic melting temperature is the point at which any mixed solution is at its lowest melting temperature, it is however difficult to identify. The melting of a clathrate is also an essential reading to get as it will also help determine salinity and density of more carbonic-rich FI. Clathrates are ice like solid phases that form on the molecular interface of two varying substances, for instance, CO_2 and H_2O (Bakker and Thiery, 1994). These clathrate solids appear during cooling at temperatures between 0 ˚C to 20˚C.

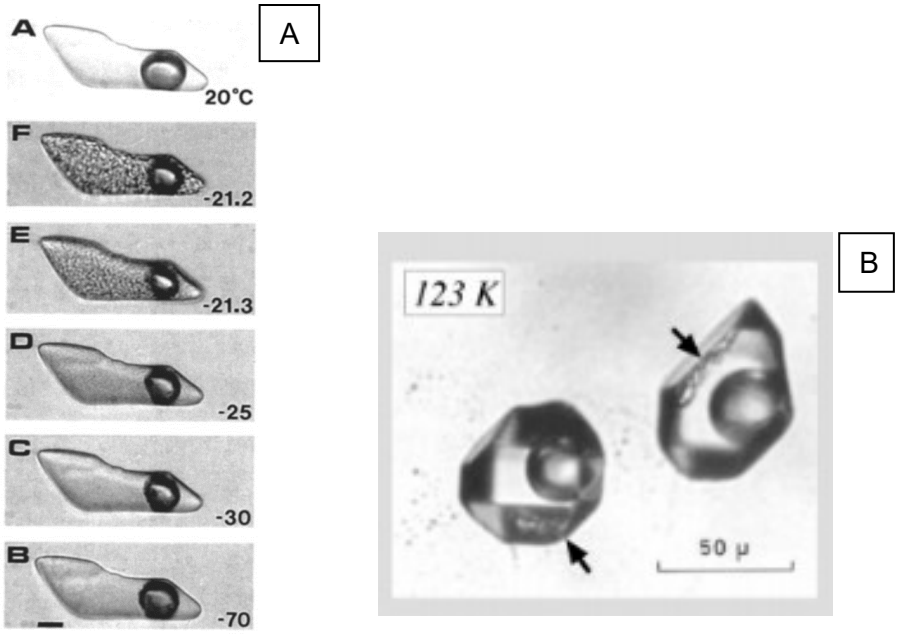

Figure 4.16: A. Example illustrating the stages of freezing in a carbonic rich fluid inclusion. Image provided by Goldstein and Reynolds, 1994. B. A two phase (liquid and vapor) fluid inclusion with nucleated clathrate indicated by the arrows by Bakker and Thiery.

4.4.2 Homogenization Experiments

Heating experiments work very similarly as freezing, except there are a few steps that need to occur before a sample is heated. Firstly, after freezing experiments are finished allowing the dewer hose that is connected to the stage to heat up to room temperature. This hose will need to be detached before heating the stage. If the line is left in, you risk melting it inside the stage which will break the stage entirely. Once the line is no longer frozen gently pull out the white foam dewer line and the inner black hose from the stage. There still may sound like there is air coming from the hose, this is normal and do not be alarmed. Next set the rate, temperature limit and hold time for homogenization experiments. See Table 4.3 for an example on the temperature ranges for heating samples.

Linkam recommends attaching the water-cooling system for homogenization experiments as with excessive heat through the stage, the stage can get very hot and cause injuries. However, this system is not equipped with the water-cooling system and is not necessary for lower temperature homogenization experiments.

Table 4.3: Examples of temperatures and rates used for homogenization experiments.

Rate ˚C/min	Limit ˚C	Time h:m: s
20.00	25.0	00:05:00
15.00	150	00:05:00
15.00	250	00:05:00
10.00	300	00:05:00
10.00	350	00:05:00
10.00	400	00:05:00
10.00	550	End Run

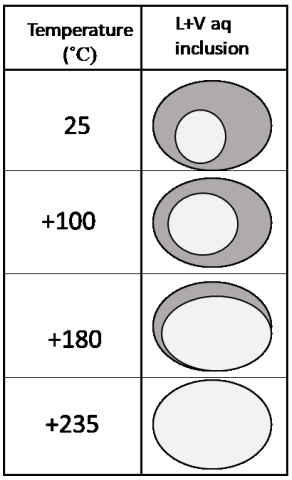

Figure 4.17: Example of a two-phase aqueous fluid inclusion homogenizing at +235 ˚C to the vapor phase.

You never want to heat a sample up to quick and from this point further the liquid nitrogen will no longer be used. Once a temperature max has been reached the stage must cool to room temperature on its own. To witness homogenization, slowly increase the temperature by intervals of 50 ˚C or 100 ˚C. Notice the size of the fluid inclusions and the phase proportions. Upon heating, for two phase FI, the vapor bubble will either shrink or expand. If the vapor bubble shrinks till you can only see one phase, then the inclusion has homogenized. If the vapor bubble expands till you see one phase, then the inclusion has homogenized. The phases at which the inclusion homogenizes to, indicates the dominate phase present at the time the FI formed. Note that if you see a FI turn dark it most likely decrepitated, meaning it was heated to quickly or to high causing the inclusion to explode so to speak. See Figure 4.17 for an example of what homogenized fluid inclusions look like.

A key thing to remember is that you want to try and homogenize the same fluid inclusions that you preformed freezing experiments on. This is because in order to illustrate the characteristics of suspected ore forming fluids both freezing and heating data needs to be collected. It is, however, good practice to get a wide variety of data points in all inclusion's types, i.e. primary, secondary

and pseudo-secondary to see if there are any differences amongst the FIA. This can also help indicate if any various fluid mixtures are present.

4.5 Summary

Proceeding microthermometry analysis there are several external calculations that need to be performed in order to find the salinity (wt. % NaCl), density, mole volume etc. for all analyzed FI. There are numerous calculations (e.g. Darling, 1991; Diamond, 1993) that can be done by hand; however, newly developed software's make it easier to input microthermometry data to retrieve salinity values. Bakker, 2003 developed one of the first computer software's (FLUIDS 1) which contains five programs that calculate a range of fluid properties using microthermometric data, micro-Raman spectroscopic data, cation ratios, volumetric ratios. The HokieFlincs Microsoft Excel spread sheet which was developed by Steele-MacInnis et al., 2012, can be used to interpret Microthermometric data and other microanalytical data providing you with density, salinity and so forth. Refer to Steele-MacInnis, 2018 for a program that uses equations of state to determine composition, density and isochore for carbonic baring FI. In previous years some researchers (Mernagh and Wilde, 1989; Crawford, 1981) would use strictly Raman spectroscopic data to interpret and calculate the salinity for FI, however, there is much controversy based of the uncertainties in these calculations. To which ever method one decides to use to calculate and interpret data, always compare methods to assure there is a reproducibility in your results.

Microthermometry is a very time consuming yet extremely useful analytical technique. Working with microscopic fluid inclusion samples deems many issues sometimes hindering data and sample sizes. It is important to put much effort into the early petrographic stages of a fluid inclusion study to thoroughly develop a cohesive understanding for the samples at hand. When running both freezing and homogenization experiments be sure to note all visible changes in FI and mineral grains. The more information you include in your observations allows for more precise interpretations when going through the results.

4.5.1 Other Analytical Techniques

Although microthermometry is a good analytical tool used to understand more about fluid inclusions, it alone does not provide any geochemical data. Microthermometry must be couple with other analytical tools such as Raman micro spectroscopy, laser ablation inductively coupled

mass spectrometry, acoustic decrepitation and crush leach. With properly preformed microthermometry analysis along with one of the above mention geochemical analysis fluid inclusion data can provide valuable insights to fluid systems that resulted in mineralization.

4.6 References

Bakker, R.J., 2003. Package FLUIDS 1. Computer programs for analysis of fluid inclusion data and for modelling bulk fluid properties. Chem. Geol. 194, 3-23.

Bakker, R.J. and Thiery, R., 1994. Application of clathrates to fluid inclusions studies. In B. de Vivo and M.L. Frezzotti, Eds., IMA '94 Short Course on Fluid Inclusions in Minerals. Virginia Tech, Blacksburg, 191–208.

Bodnar, R.J., 2003. Introduction to fluid inclusions. In I. Samson, A. Anderson, & D. Marshall, eds. Fluid Inclusions: Analysis and Interpretation. Mineral. Assoc. Canada, Short Course. 32, 1-8.

Crawford, M.L., 1981. Phase equilibria in aqueous fluid inclusions. In Fluid Inclusions: Applications to Petrology (L.S. Hollister & M.L. Crawford, eds.). Mineral. Assoc. Can., Short Course Handbook 6, 75-100.

Darling, R.S., 1991. An extended equation to calculate NaCl contents from final clathrate melting temperatures in H2O-CO2-NaCl fluid inclusions: Implications for P-T isochore location. Geochim. Cosmochim. Acta. 55, 3869-3871.

Diamond L. W., 1992. Stability of CO2 clathrate hydrate 1 CO2 liquid 1 CO2 1 aqueous KCl-NaCl solutions: Experimental determination and application to salinity estimates of fluid inclusions. Geochim. Cosmochim. Acta 56, 273–280.

Diamond, L.W., 1994. Salinity of multivolatile fluid inclusions determined from clathrate hydrate stability. Geochim. Cosmochim. 58(1),19-41. https://doi.org/10.1016/0016-7037(94)90443-X.

Fagereng, Å., Remitti, F., and Sibson, R.H., 2011. Incrementally developed slickenfibers—Geological record of repeating low stress-drop seismic events?.Tectonophysics. 510, 381–386.
https://doi.org/10.1016/j.tecto.2011.08.015.

Goldstein, R.H., 2001. Fluid inclusions in sedimentary and diagenetic systems. Lithos 55, 159–192.

Goldstein R., 2003. Petrographic analysis of fluid inclusions. In Fluid Inclusions: Interpretations. Mineral. Assoc. Canada, Short Course. 9-55.

Lespinasse, M., Pecher, A., 1993. Microfracturing and regional ´ stress field: a study of preferred orientation of fluid inclusion planes in a granite from the Massif Central, France. J. Struct. Geol. 8, 169–180.

Mernagh, T.P., Wilde, A.R., 1989. The use of the laser Raman microprobe for the determination of salinity in fluid inclusions. Geochim. Cosmochim. Acta. 53(4), 765-771.

https://doi.org/10.1016/0016-7037(89)90022-7.

Roedder, E., 1984. Fluid inclusions. Rev. Mineral. 12.

Roedder, E., Bodnar, R. J., 1997. Fluid Inclusion studies of hydrothermal ore deposits. Fluid inclusion studies of hydrothermal ore deposits. In: Barnes HL (ed) Geochemistry of hydrothermal ore deposits, 3rd edn. Wiley, New York. 657–698

Steele-MacInnis, M., 2018. Fluid inclusions in the system H2O-NaCl-CO2: An algorithm to determine composition, density and isochore. Chem.l Geol. 498, 31-44. https://doi.org/10.1016/j.chemgeo.2018.08.022

Steele-MacInnis M.J., Lecumberri-Sanchez P., Bodnar R. J., 2012. HOKIEFLINCS-H2O-NACL: A Microsoft Excel spreadsheet for interpreting microthermometric data from fluid inclusions based on the PVTX properties of H2O–NaCl. Comput. Geosci. http://dx.doi.org/10.1016/j.cageo.2012.01.022.

Touret, J.L.R., 2001. Fluids in metamorphic rocks. Lithos, 55,1–27.

Van den Kerkhof, A.M., Hein, U. F., 2001. Fluid inclusion petrography. Lithos. 55, 27–47.

Chapter 5: Conclusion

This thesis explored Archean orogenic gold systems, the mineralizing fluids present in these systems, gold complexing and transport mechanisms and a brief history on gold mining in the BGB, in Chapter 1. Two mineralizing reefs within the Fairview mining district were dissected geochemically, in attempt to determine the origin, composition and variations in the mineralizing fluids. Readdressing the primary research aims of this thesis:

I. What is the nature and source of the gold-forming fluids throughout the Main Reef Complex and Hope Reef within Fairview mining district?

Low salinity and $\delta^{18}O$ values indicate a metamorphic origin for the mineralizing fluids. The metavolcanics of the Onverwacht and metasediments of the Fig Tree Group are ideal corridors for fluid to interact with and leach out gold. Data limitations hindered the ability to find what fluids were responsible for gold mineralization with in the MRC and HR, however, new light has guided the way for further sampling and analysis in both reefs by other researchers in hopes to pinpoint gold mineralizing fluid in the BGB, but more importantly in worldwide Archean orogenic systems.

II. Does the fluid inclusion and isotopic data from the Main Reef Complex compare or contrast to the Hope Reef and what does this state about the mineralizing fluids?

Although challenges were present when preforming microthermometry experiments on FI due to the abundance of FIA and inadvertently the microscopic size of studied FI, data that was collected indicates a possible evolution in mineralizing fluids. Oxygen stable isotope data from quartz veins shows that slight variations exist between the fluids that mineralized the MRC (higher oxygen isotope values) and HR (lower oxygen isotope values). Textural similarities within the MRC and HR also show abundant recrystallization in quartz grains and microthermometry results indicate a likely higher trapping temperature for secondary FI. Overall the analytical tests performed in this study have illustrated the differences and similarities in the wall-rock, alteration and gold grades within MRC and HR.

Working from the structural kinematics from Gloyn-Jones and Kisters, 2018, 2019 has proved to be critical in making this study possible. Although perplexities remain on the origin of gold producing fluid, graphitic alterations in the MRC and the timing of gold. The fluid

geochemistry for both the MRC and HR are reflected by the structural positioning of the two reefs in relation to the Fig Tree Group and Onverwacht Group, as well as the multitude of deformational phases and faulting events from the Sheba Fault. The student t-test conducted on primary versus secondary FI of aqueous and carbonic FI types for the MRC and HR show a possible heightening in P-T conditions for secondary FI. It is possible and likely that as described in scenario two, progressive deformation, faulting and the F3- F3b folding events acted as the driving forces for higher volumes of metamorphic fluid as well as the P-T increase that was likely present during the time of secondary mineralizing events. This will need further exploration with a larger samples size and more structural parameters in regions closer to the Sheba Fault.

5.1 Overview of geochemical analysis in the MRC and HR

The MRC and HR are proxies for other Archean orogenic systems that have similar formational and structural characteristics. To more widely understand the evolutionary timeline of fluid flow and the development of these two gold complexing reef structures further structural and geochemical data must be done. Recommendations for future work on this region would be to: sample closer to the Sheba Fault, to test isotopic values and gold grades; conduct more fluid inclusion and isotope analysis in quartz veins proximal and distal to high gold graded regions; preform carbon and hydrogen isotope analysis on quartz veins and on the surrounding greywacke and graphitic-rich shale.

5.2 Prospect for Stellenbosch University fluid inclusion laboratory

The addition of the fluid inclusion laboratory in the Earth Science department has elevated the availability for current students and faculty to expand analysis on projects they may be conducting. This relatively inexpensive, easy to maintain piece of equipment, is a great tool for young and seasoned scientist alike, to venture into the realm of fluid inclusions. It is my hope that this fluid inclusion laboratory is used for training those who are interested in microthermometry analysis and producing quality fluid inclusion research. Also, this is now a pivotal chance for the Earth Science department at Stellenbosch University to form national and international collaborations with other institutes and researchers that may be interested in using the newly purchased equipment.

5.1 References

Gloyn-Jones, J.N., Kisters, A.F.M., 2018. (in press). Ore-shoot formation in the Main Reef Complex of the Fairview Mine: multiphase gold mineralization during regional folding, Barberton greenstone belt, South Africa. Mineralium Deposita.

Gloyn-Jones, J., Kisters, A., 2019. Ore-shoot formation in the Main Reef Complex of the Fairview Mine—multiphase gold mineralization during regional folding, Barberton Greenstone Belt, South Africa. Mineralium Deposita.
https://doi.org/10.1007/s00126-019-00865-9

Appendix I

Fluid inclusion analysis and isotopic investigation of two structurally constrained gold mineralization in the Fairview mining complex, Barberton, South Africa

Christina M. Comuso, Bjorn P. von der Heyden
University of Stellenbosch

Matthew Severs
Stockton University

Chris Harris
University of Cape Town

Abstract: The Barberton Greenstone Belt (BGB) in South Africa hosts numerous lode gold deposits in several lithologies and structural settings. The goal of this project is to characterize and understand the nature/source of the gold-transporting fluids in the Sheba/Fairview mining district. To achieve this, a comprehensive fluid inclusion (FI) and δO^{18} investigation of black quartz veins present within the Hope Reef (HR) and Main Reef Complex (MRC) at the Fairview mine is being conducted. The formation of both orebodies is related to progressive phases of horizontal NW-SE directed shortening correlative to D_3 deformation. Preliminary petrographic work shows that the samples contain primary and secondary FI assemblages containing liquid and vapor phases. Fluid inclusions revealed freezing temperatures between -55° to -56°C, indicating a CO_2 rich fluid. Clathrate melting temperatures ranged from 8° to 18.9°C suggesting a thin liquid or vapor film may exist within the FI and the fluids are a H_2O-CO_2 mixture. Finally, homogenization temperatures ranged between 202°C to 231.6°C, suggesting the mineralizing fluids to be similar in composition and in P-T conditions. Further geochemical analytical work, based on a structurally constrained and larger sample set, will better characterize the fluids responsible for Au mineralization in the HR and the MRC.

1 Introduction

There is a lack of understanding on the dominant factors that lead to gold mineralization in the Barberton Greenstone Belt. The global accepted generic models of orogenic gold systems remain unanswered; however, the consensus is that metamorphic fluids are responsible for most of the world's orogenic gold deposits (Groves et al. 2018). What is agreed however, is that structural kinematics provide the necessary features to facilitate fluid flow, and the siting of gold mineralization commonly depends heavily on fluid interaction with the surrounding wall rock. Models produced by Colvine, (1989) and Groves et al. (1998) suggest transport distances are extensive, coming from great depths, allowing hydrothermal fluids to interact with surrounding wall rock before being halted at more crustal depths. At the Sheba/Fairview mining district in the BGB, one of the oldest running gold mines in the world, over 345t of Au have been produced since 1883 (Dirks et al., 2009). The current values of gold production could be much higher with a better understanding of the geochemistry of the mineralizing fluids to target exploration.

2 Regional geology

The BGB is a NE trending synclinal belt bounded by 3.5-3.1 Ga Tonalite-Trondjhemite-Granodiorite (TTG) and granites centralized to the east of the Kaapvaal Craton (Anhaeusser, C.R et al. 1981; De Ronde et al. 1992; Lowe and Byerly 1999; Lowe & Byerly 2007; Gloyn-Jones & Kisters 2018). The Sheba/Fairview mining district, situated in the BGB, is dominated by the Eureka and Ulundi reclined synforms. Multiple phases of deformation (D_1-D_4) including accretion, shortening, regional folding, and extension have affected the regional geology of the BGB.

Three main stratigraphic units make up the BGB, which include, starting with the base and moving upward: (1) The Onverwacht Group (ca. 3.57 – 3.30 Ga), composed of mostly mafic and ultramafic volcanic lithologies, interbedded with thinly layered chert and felsic volcanics; (2) the Fig Tree Group (3.259-3.298 Ga), consisting of turbiditic greywackes, chert, mudstone, shale, banded iron formations and some volcaniclastic rocks; and (3)

the Moodies Group (3.226 -3.16 Ga), mainly clastic sedimentary rocks, sub greywacke, quartzose, and feldspathic sandstones (De Ronde et al. 1992; Lowe and Byerly 1999; Lowe & Byerly 2007). Along the central-southern part of the Eureka and Ulundi Synclines sits the Fairview Mine as seen in Figure 1 (Otto et al. 2007). Over time the Eureka and Ulundi Synclines were refolded leading to the multitude of quartz-carbonate veins seen throughout the mine (Dziggel et al. 2007). The increase in structural porosity through these less competent rocks allowed for Au to be hosted in these numerous veins within the Fairview Mine (Hofmann and Harris 2008; Altigani et al. 2016). The Sheba Fault, which acts as a catalyst for most deformational events within the Fairview mining district is made up of various sheared and regressed serpentinites, talc-carbonate schists and cherts all found within the Weltevreden Formation fixed between both the Ulundi and Eureka synforms (Ramsay 1963; Byerly et al.1996; Lowe and Byerly 1999; Gloyn-Jones & Kisters 2018). The formation of the HR and the MRC orebodies is predominantly linked to progressive phases of horizontal NW-SE direct shortening which has been correlated to late D_3 deformation (Gloyn-Jones & Kisters 2018).

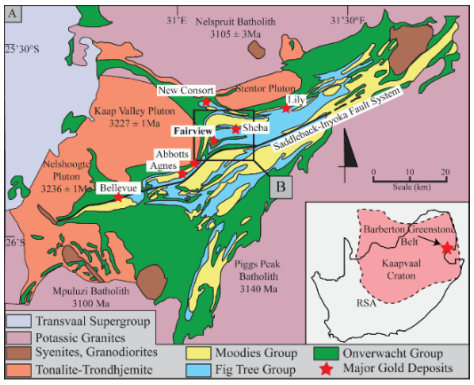

Figure 1. Regional map of the Barberton Greenstone Belt illustrating gold mine localities, stratigraphic lithologic groups and surrounding intrusive bodies (Anhaeusser et al. 1981; Dirks et al. 2013; Agangi et al. 2014; Gloyn-Jones & Kisters 2018).

3 Mineralizing reef complexes

3.1 Hope Reef Complex (HR)

There are two main mineralized shear zones within the HR that are characterized as high-angled sets brittle ductile regions. First being a shallow ESE dipping, slightly undulated NNE trending reef, and several moderate to steeply dipping NW and NE trending structures (Gloyn- Jones & Kisters, 2018). The more imperative portion of the HR where mineralization and this study is focused is within the shallow reef. Structural analysis from Gloyn-Jones & Kisters (2018) was done within the Fairview Mine of the Hope Reef complex at level 58. This level of the mine is the shallow portion of the reef and shows high grade mineralization with associated quartz veining, sulphide mineralization, and fuschite/sericite rich alteration, all bounded by a SE shallow dipping brittle-ductile shear zone system (Gloyn-Jones & Kisters 2018). The Hope Reef is situated in the lower portion of the Sheba Formation above the Sheba fault and Main Reef Complex, composed of mostly a greywacke package (Gloyn-Jones & Kisters 2018). The entirety of the Hope Reef is made up of both shallow and steeply dipping mineralized zones that are confined to the greywacke units of the Fig Tree Group (Gloyn-Jones& Kisters 2018).

3.2 Main Reef Complex (MRC)

The MRC is moderately- to steeply- SE-plunging orebody governed by a jog-like corridor characterized by a severely mis-orientated brittle-ductile shear zone confined to the immediate hanging wall greywacke and shale units along the Sheba fault zone (Gloyn-Jones & Kisters 2019). In the MRC of the Fairview Mine, higher gold grades are spatially associated with shale units of the metasediments in the lower Fig Tree Group and gradually terminates along strike (Gloyn- Jones & Kisters 2019). There are two distinct forms of mineralization within the MRC; sulphide mineralization that is associated with blackish-grey quartz carbonate veins, and mineralization of similar sulphides dominantly in the surrounding shale wall-rocks (Gloyn-Jones & Kisters 2019). Samples were collected from level 25/27 for this study.

4 Preliminary data

4.1 δO18 stable isotope data

Black quartz grains from both HR and MRC were crushed and isolated at 4g per sample to be analyzed for oxygen isotopes at the stable isotope laboratory of the Department of Geological Sciences, University of Cape Town utilizing the laser fluorination method of Harris and Vogeli 2010. A total of twelve samples were tested for δO_{18} signatures, ten samples from Fairview Mine (both of HR and MRC) and two from Sheba were analyzed. Figure 2 shows the samples from this study have similar isotopic compositions compared with others in literature at similar deposit types such as K. Farber et al. 2016; De Ronde et al. 1992 study at the Barberton Greenstone Belt, and Beaudoin & Pitre 2005 at the Val-d'Or vein field, Abitibi, Quebec, Canada.

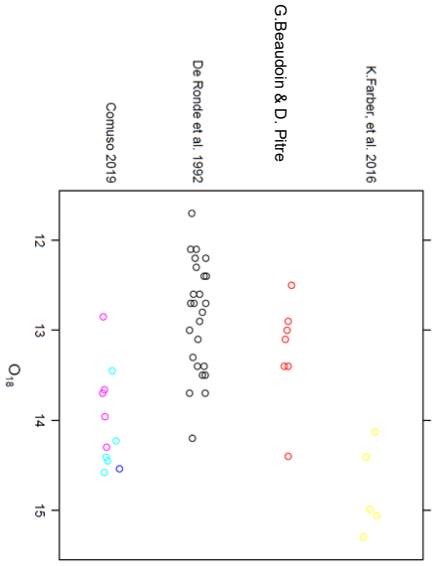

Figure 2. δO_{18} stable isotope data of samples from this study collected at Sheba/Fairview Mines MRC and HR compared to other isotopic data collected in similar localities. The data range between 12-14.5 for all studies show similar metamorphic signatures for fluid source. For this study the purple points represent MRC samples, light blue is from HR and dark blue are samples analyzed from Sheba mine.

4.2 Microthermometric analyses

Microthermometric analysis were performed on samples containing viewable fluid inclusion assemblages. Freezing and homogenization measurements were done using an Olympus BH-2 microscope equipped with a Linkam THM600/HFS600 temperature-controlled stage with a T95 system controller. Calibration was set using H_2O/CO_2 inclusions in quartz against the melting point of CO_2. The results suggest an H_2O-CO_2 dominated composition that homogenized between 202-231.6°C.

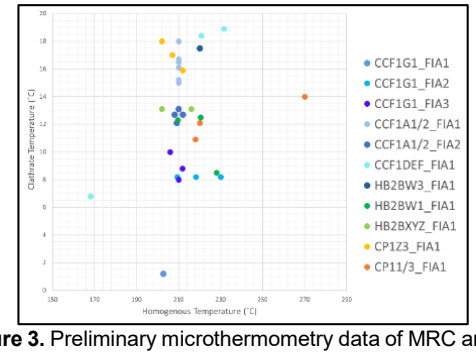

Figure 3. Preliminary microthermometry data of MRC and HR quartz vein samples from Fairview Mine. Homogenizing temperatures were plotted against clathrate melting temperatures. Both sampled areas show similarities in average freezing temperatures, clathrate melting temperatures, and homogenization temperatures.

4.3 Raman spectroscopy

In order to better understand the composition of the liquid and vapor phases for selected fluid inclusions, the Raman spectrometer (Witwatersrand University, School of Physics) was used. Representative samples of viewable fluid inclusions from both HRC and MRC were analyzing using a Horiba LabRAM-HR Raman spectrometer, mounted to an Olympus BX-41 microscope with a Lexel Model 95 SHG Argon ion laser. Preliminary results suggested the presence of graphite, methane, water and carbon dioxide within the inclusions.

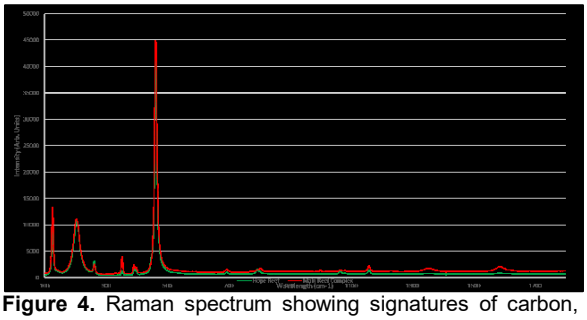

Figure 4. Raman spectrum showing signatures of carbon, methane and water (further down the spectrum) in both liquid and vapor phases of fluid inclusions within black quartz veins.

4.4 Scanning electron microscope (SEM)- cathodoluminescence (CL)

SEM-CL was used to better identify quartz grain boundaries to locate primary FI and to analyze mineral compositions within each sample. Various textures of quartz can be seen with zonation and secondary sulphide mineralization.

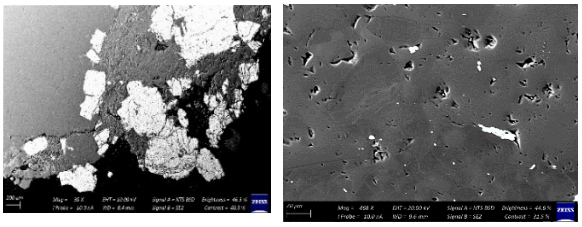

Figure 5. Left image: SEM images with backscattered light indicates zonation in quartz grains and secondary rutile mineralization (represented in white). Right image: Unaltered quartz grain with secondary sulphide mineralization along grain boundary with primary altered quartz and sulphide grains.

5 Discussion

The variable amounts of gold mineralization in the BGB represents the multiple fluid pulses, the differences in structural kinematics, and the fluid to

wall rock interactions that can be seen in both Sheba and Fairview Mines (Bierlein and Maher 2001; Altigani et al. 2016). Combining the geochemical data from this study to the structural studies done by Gloyn-Jones & Kisters in 2018 and 2019 it is evident that both the MRC and HR vary, structurally, lithologically and temporally. These differences, however, do not reflect the fluid phases that have flowed through both the HR and MRC. Utilizing the structural kinematics from Gloyn-Jones & Kisters 2018 and 2019 for sample collecting in this study and running preliminary fluid inclusion and isotope analysis it is more plausible that the fluids that mineralized both the HR and MRC at Fairview Mine originated from a similar source. After the F_3 folding event of the Ulundi Syncline, the "fluid valve" that percolated fluid to HR was closed off. The presence of the Sheba Fault allowed fluid flow to be centralized up the fault through the MRC. The clustering of isotopic data and microthermometric data supports the idea that fluids that mineralized both the MRC and HR could be similar in origin. It is essential to understand the role the wall rock and ligands play when interacted with fluid phases. Whether gold mineralization is sourced from fluid transport or as a result of precipitation remains enigmatic. More geochemical analytical work is being done at both mineralizing reefs at Fairview Mine to further support the theory that mineralizing fluids could have originated from the same or very similar sources.

Acknowledgements

This study was made possible through support from NRF grant 106006 with additional funding from DST-NRF CIMERA and the Society of Economic Geologist. Thank you, Mark Evans at Central Connecticut State University, for allowing me to run preliminary microthermometry experiments, Rudolph Erasmus at the University of Witwatersrand for Raman spectroscopy analysis and the CAF lab at University of Stellenbosch for assistance with SEM-CL analytical data.

References

Agangi, A., Hofmann, A., & Przybyłowicz, W. (2014). Trace element zoning of sulfides and quartz at sheba and fairview gold mines: Clues to mesoarchean mineralisation in the barberton greenstone belt, south africa. Mineralium Deposita, 56: 94–114.

Agangi, A., Hofmann, A., Eickmann, B., Marin-Carbonne, J., Reddy, S.M. (2016). An atmospheric source of S in Mesoarchaean structurally-controlled gold mineralisation of the Barberton Greenstone Belt. Precambrian Res. 285: 10–20.

Anhaeusser, C.R., Robb, L.J., Viljoen, M.J. (1981). Provisional geological map of the Barberton Greenstone Belt and surrounding terrane, eastern Transvaal and Swaziland scale 1: 125,000. Geol. Soc. South Africa.

Barberton Mines (Pty) (2013). Mineral Resource and Mineral Reserve Report 2013.

Beaudoin, G., & Pitre, D. (2005). Stable isotope geochemistry of the Archean Val-d'Or (Canada) orogenic gold vein field. Mineralium Deposita. 40: 59-75.

Bierlein, F. & Maher, S. (2001). Orogenic disseminated gold in phanerozoic fold belts - Examples from Victoria, Australia and elsewhere. Ore Geology Reviews. 18: 113-148.

Byerly, G.R., Kröner, A., Lowe, D.R., Todt, W., Walsh, M.M. (1996). Prolonged magmatism and time constraints for sediment deposition in the early Archean Barberton Greenstone Belt: evidence from the Upper Onverwacht and Fig Tree groups. Precambrian Res. 78: 125–138.

Colvine, A.C. (1989). An empirical model for the formation of Archean gold deposits: products of final cratonization of the Superior Province, Canada. In: Keays RR, Ramsay WRH, Groves DI (eds) The geology of gold deposits: the perspective in 1998. Econ Geol Monogr 6:37–53

De Ronde, C.E.J., Spooner, E.T.C., De Wit, M.J., Bray, C.J. (1992). Shear zone-related, Au quartz vein deposits in the Barberton Greenstone Belt, South Africa: Field and petrographic characteristics, fluid properties and light stable isotope geochemistry. Econ. Geol. 87: 366–402.

Dirks, P.H.G.M., Charlesworth, E.G., Munyai, M.R. (2009). Cratonic extension and Archaean gold mineralisation in the Sheba-Fairview mine, Barberton greenstone belt, South Africa. South African J. Geol. 112: 291–316.

Dirks, P.H.G.M., Charlesworth, E.G., Munyai, M.R., Wormald, R. (2013). Stress analysis, post-orogenic extension and 3.01Ga gold mineralisation in the Barberton Greenstone Belt, South Africa. Precambrian Res. 226: 157–184.

Dziggel, A., Otto, A., Kisters, A.F.M., Meyer, F.M. (2007). Chapter 5.8 Tectono-Metamorphic Controls on Archean gold mineralization in the Barberton Greenstone Belt, South Africa: An Example from the New Consort Gold Mine. Dev. Precambrian Geol. 15: 699–727.

Farber, K., Dziggel, A., Meyer, F.M., & Harris, C. (2016). Petrology, geochemistry, and fluid inclusion analysis of altered komatiites of the Mendon Formation in the BARB4 drill core, Barberton greenstone belt, South Africa. South African Journal of Geology. 119.

Gloyn-Jones, J., & Kisters, A. (2018). Regional folding, low-angle thrusting and permeability networks: Structural controls of gold mineralization in the Hope reef at Fairview Mine, Barberton Greenstone Belt, South Africa. Ore Geology Reviews. 102.

Gloyn-Jones, J., & Kisters, A. (2019). Ore-shoot formation in the Main Reef Complex of the Fairview Mine—multiphase gold mineralization during regional folding, Barberton Greenstone Belt, South Africa. Mineralium Deposita.

Groves, D.I., Goldfarb, R.J., Gebre-Mariam, M., Hagemann, S.G., & Robert, F. (1998). Orogenic gold deposits: A proposed classification in the context of their crustal distribution and relationship to other gold deposit types. Ore Geology Reviews. 13(1–5): 7-27.

Groves D.I., Goldfarb R.J., Santosh M., Zhang L. (2018). Structural geometry of orogenic gold deposits: Implications for exploration of world-class and giant deposits. Geosci Front.

Harris, C., & Vogeli, J. (2010). Oxygen isotope composition of garnet in the Peninsula Granite, Cape Granite Suite, South Africa: Constraints on melting and emplacement mechanisms. South African Journal of Geology. 113.

Hofmann, A., & Harris, C. (2008). Silica alteration zones in the Barberton greenstone belt: A window into subseafloor

processes 3.5-3.3 Ga ago. Mineralium Deposita, 257(3–4):224–242.

Lowe, D.R., Byerly, G.R., Heubeck, C. (1999). Structural divisions and development of the 70 west-central part of the Barberton Greenstone Belt, South Africa. Geol. Soc. Am. Spec. Pap. 329: 37–82.

Lowe, D.R., Byerly, G.R. (2007). An Overview of the Geology of the Barberton Greenstone Belt and Vicinity:

Ramsay, J.G. (1963). Structural investigations in the Barberton Mountain Land, Eastern Transvaal. Trans. Geol. Soc. South Africa 66: 353–401.

Implications for Early Crustal Development. Dev. Precambrian Geol. 15: 481–526.

Otto, A., Dziggel, A., Kisters, A. F. M., & Meyer, F. M. (2007). The New Consort Gold Mine, Barberton greenstone belt, South Africa: Orogenic gold mineralization in a condensed metamorphic profile. Mineralium Deposita, 42(7): 715–735.

Appendix II

Preliminary data collection of microthermometry analysis at Central Connecticut State University of samples for this study.

Sample	Chip	Type	T_{ff}	T_m	T_{cm}	T_h
MRC	CF1a	P	-60	-56.6	1.2	202.6
	b	P	-56	X	8.2	209.3
					13.1	230
					9.4	218.2
	c	P	X	-54	8	210
					8.8	211.8
					10	205.9
	d	P	-59	-55	15.7	210
					15.2	210
					16.5	210
					18	210
					15	210
					16.1	210
	e	P	-55	-51.2	18.9	168
					6.8	220.7
					18.4	231.6
MRC	CP1a	P	-52.8	-51	18	202
					17	207
					15.9	212
					9.5	217
	b	P	-49.6	-53.7	11	210
	c	P	-54.9	-58.8	12.1	210
					10.9	>270
					14	210
Hope Reef	HB2Ba	P	X	-56.7	17.5	210
	b	P	-54.4	-55	12.3	220.5
					12.5	228
	c	P	X	X	8.5	202
					13.1	216
					10.2	220

Appendix III

Scanning Electron Microscope analysis of thin section samples from the MRC and HR. Data was not used in the bulk of the thesis. Figure below indicates the variations in quartz grain textures in relation to sulphides.

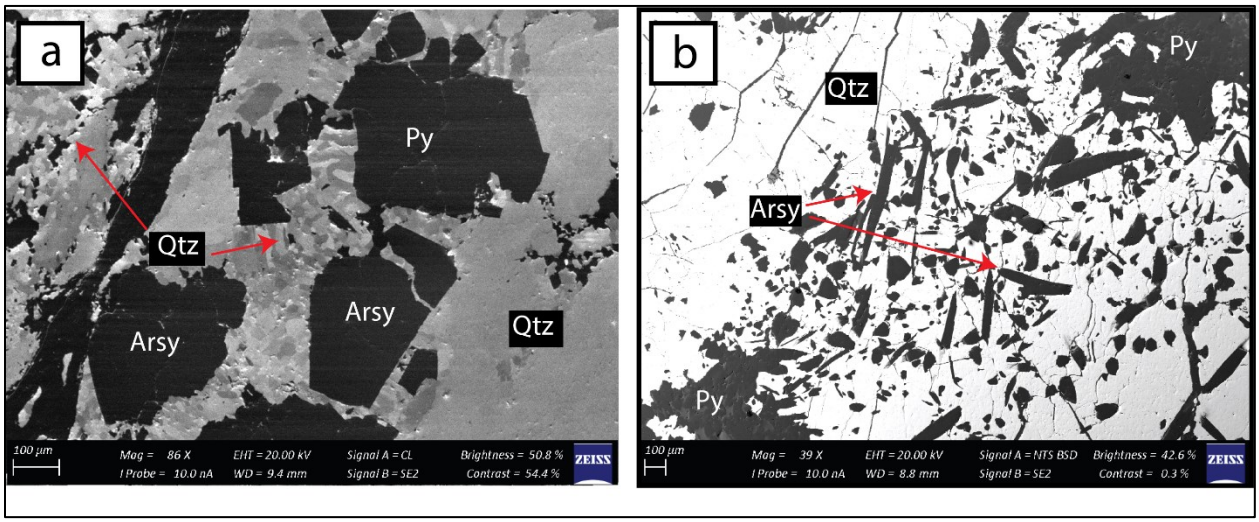

Paragenetic model developed based off mineralogical interpretation during petrographic and ore microscopy analysis from this study.

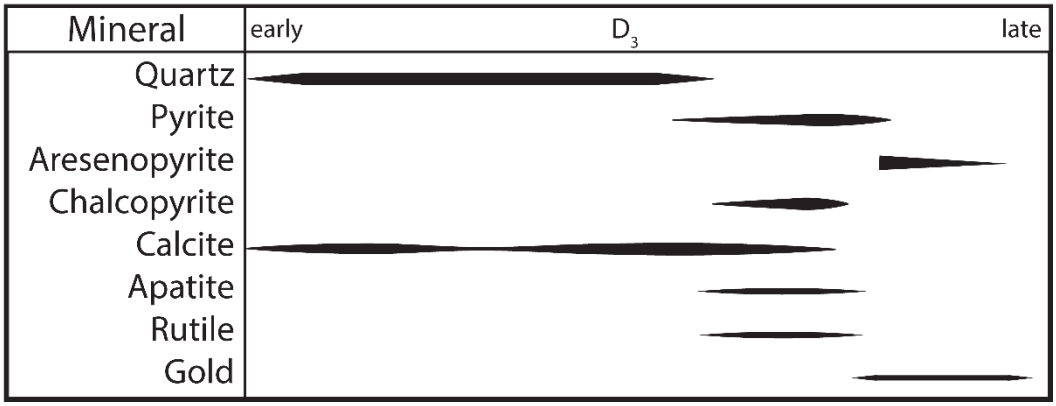

Table comparing preliminary microthermometry results of this study to fluid inclusion data in similar deposit types from literature.

Author	Location	Ore /Mineral Type	Inclusion Type	Tm range (˚C)	Tm	NaCl range	NaCl	Th* range (˚C)	Th* average (˚C)
Vries S. & Touret J, 2006	BGB, RSA	Quartz veining/Banded Chert/Breccias of Buck Ridge Chert	H_A	-18.8 to -8.4	-12.2	21.5 to 12.2	16	115.7 to 199.8	153.9
			M_A	-8.3 to -4.1	-6.7	12.1 to 6.6	10.1	96.0 to 160.0	130
			L_{A-I}	-4.2 to -1.4	2.9	6.7 to 2.4	4.7	140.9 to 216.1	182.2
D. D. van Reenen et al. 1993	**Hout River Shear Zone Limpopo Belt, RSA**								
	Fumani	Quartz veining from lode gold deposits	I	-22 to +1	-3.6	na	5	81.5 to 239.8	152
	Osprey		I	-60.5 to -56.6	-56.9	na	25	115.8 to 208	164
	Louis Moore			na	-57.3	na	na	-4 to 12	3.7
	Klein Letaba		I	-56.8 to -57.7	na	na	na	-23 to 23	-10 and 18
	Birthday			na	-56.9	na	na	-21 to 16	-11 and 6
De Ronde et al. 1992	**BGB, RSA**								
	Abbot Mine	Gold bearing Quartz-Carbinate veins	I	-57.2 to -56.5	-56.8	4.1 to 8.6	6	242 to 319	282
	Pioneer Mine		I	-57.5 to -56.4	-56.8	1.8 to 8.5	5.7	195 to 307	257
	Bellevue Mine		I	-57.3 to -56.3	-56.8	3.8 to 6.8	4.8	233 to 314	277
This Study	**BGB, RSA**								
	Fairview Mine								
	Main Reef Complex								
	CCF1	Quartz-Carbonate Cut off Veins	II	-51.3 to -56.6	-54.2	na	na	202.6 to 230	212.6
	CPI	Sericite alteration, quartz- carbonate veining, sulphides	II	-51 to -58.8	-51.5	na	na	202 to 270	221.8
	Hope Reef					na	na		
	HB2B	Hydraulic Breccia/ Sulphide bearing	I	-55 to -56.7	-55.9	na	na	202 to 228	215.3

Appendix IV

Results of a Student t- test Assuming unequal Variances of MRC and HR. Both reefs were tested for the following: Type I- primary Tm_{ice} for each reef, primary Th for each reef, secondary FI $T_m$ice for each reef, secondary Th for each reef. Type II- primary Tcm for each reef, primary Th for each reef, secondary Tcm for each reef, secondary Th for each reef.

TmIce Primary FI (HR &MRC)								
	HR	*MRC*		*HR*	*MRC*		*HR*	*MRC*
Mean	-9.75	-8.39	Mean	-9.74615	-8.3875	Mean	-9.75	-8.39
Variance	11.27	5.75	Variance	11.27103	5.752679	Variance	11.27	5.75
Observations	13.00	8.00	Observations	13	8	Observations	13.00	8.00
Hypothesized Mean Difference	0.00		Hypothesized Mean Difference	0		Hypothesized Mean Difference	0.00	
df	18.00		df	18		df	18.00	
t Stat	-1.08		t Stat	-1.07881		t Stat	-1.08	
t Critical two-tail	2.10		t Critical two-tail	1.734064		t Critical two-tail	3.92	
95%	Accept		90%	Accept		99%	Accept	
Th(aq) Primary FI (HR & MRC)								
	HR	*MRC*		*HR*	*MRC*		*HR*	*MRC*
Mean	291.48	290.46	Mean	291.4769	290.4625	Mean	291.48	290.46
Variance	775.93	726.69	Variance	775.9286	726.6941	Variance	775.93	726.69
Observations	13.00	8.00	Observations	13	8	Observations	13.00	8.00
Hypothesized Mean Difference	0.00		Hypothesized Mean Difference	0		Hypothesized Mean Difference	0.00	
df	15.00		df	15		df	15.00	
t Stat	0.08		t Stat	0.082683		t Stat	0.08	
t Critical two-tail	2.13		t Critical two-tail	1.75305		t Critical two-tail	4.07	
95%	Accept		90%	Accept		99%	Accept	
Tm Ice Secondary FI (HR & MRC)								
	HR	*MRC*		*HR*	*MRC*		*HR*	*MRC*
Mean	-5.79	-8.92	Mean	-5.78571	-8.91667	Mean	-5.79	-8.92
Variance	13.18	5.54	Variance	13.1781	5.543333	Variance	13.18	5.54
Observations	7.00	12.00	Observations	7	12	Observations	7.00	12.00
Hypothesized Mean Difference	0.00		Hypothesized Mean Difference	0		Hypothesized Mean Difference	0.00	
df	9.00		df	9		df	9.00	
t Stat	2.04		t Stat	2.04479		t Stat	2.04	
t Critical two-tail	2.26		t Critical two-tail	1.833113		t Critical two-tail	3.25	
95%	Accept		90%	Reject		99%	Accept	
Th (aq) Secondary FI (HR & MRC)								
	HR	*MRC*		*HR*	*MRC*		*HR*	*MRC*
Mean	263.14	333.33	Mean	263.1429	333.325	Mean	263.14	333.33
Variance	2606.14	2103.50	Variance	2606.143	2103.502	Variance	2606.14	2103.50
Observations	7.00	12.00	Observations	7	12	Observations	7.00	12.00
Hypothesized Mean Difference	0.00		Hypothesized Mean Difference	0		Hypothesized Mean Difference	0.00	
df	12.00		df	12		df	12.00	
t Stat	-3.00		t Stat	-2.99913		t Stat	-3.00	
t Critical two-tail	2.18		t Critical two-tail	1.782288		t Critical two-tail	4.32	
95%	Reject		90%	Reject		99%	Accept	
Tm Clathrate Primary FI (HR& MRC)								
	HR	*MRC*		*HR*	*MRC*		*HR*	*MRC*
Mean	12.28	11.71	Mean	12.27692	11.70588	Mean	12.28	11.71
Variance	10.80	23.23	Variance	10.79859	23.23184	Variance	10.80	23.23
Observations	13.00	17.00	Observations	13	17	Observations	13.00	17.00
Hypothesized Mean Difference	0.00		Hypothesized Mean Difference	0		Hypothesized Mean Difference	0.00	
df	28.00		df	28		df	28.00	
t Stat	0.39		t Stat	0.385237		t Stat	0.39	
t Critical two-tail	2.05		t Critical two-tail	1.701131		t Critical two-tail	3.67	
95%	Accept		90%	Accept		99%	Accept	
Th Clathrate Primary FI (HR & MRC)								
	HR	*MRC*		*HR*	*MRC*		*HR*	*MRC*
Mean	243.50	218.59	Mean	243.5	218.5941	Mean	243.50	218.59
Variance	1640.33	734.87	Variance	1640.333	734.8743	Variance	1640.33	734.87
Observations	13.00	17.00	Observations	13	17	Observations	13.00	17.00
Hypothesized Mean Difference	0.00		Hypothesized Mean Difference	0		Hypothesized Mean Difference	0.00	
df	20.00		df	20		df	20.00	
t Stat	1.91		t Stat	1.913532		t Stat	1.91	
t Critical two-tail	2.09		t Critical two-tail	1.724718		t Critical two-tail	3.85	
95%	Accept		90%	Reject		99%	Accept	
Tm Clathrate Secondary FI (HR & MRC)								
	HR	*MRC*		*HR*	*MRC*		*HR*	*MRC*
Mean	10.63	10.80	Mean	10.65	10.8	Mean	10.63	10.80
Variance	13.34	4.63	Variance	13.15667	4.63	Variance	13.34	4.63
Observations	4.00	9.00	Observations	4	9	Observations	4.00	9.00
Hypothesized Mean Difference	0.00		Hypothesized Mean Difference	0		Hypothesized Mean Difference	0.00	
df	4.00		df	4		df	4.00	
t Stat	-0.09		t Stat	-0.07691		t Stat	-0.09	
t Critical two-tail	2.78		t Critical two-tail	2.131847		t Critical two-tail	8.61	
95%	Accept		90%	Accept		99%	Accept	
Th Clathrate Secondary FI (HR & MRC)								
	HR	*MRC*		*HR*	*MRC*		*HR*	*MRC*
Mean	249.85	306.74	Mean	249.85	306.7444	Mean	249.85	306.74
Variance	2229.20	2418.33	Variance	2229.203	2418.33	Variance	2229.20	2418.33
Observations	4.00	9.00	Observations	4	9	Observations	4.00	9.00
Hypothesized Mean Difference	0.00		Hypothesized Mean Difference	0		Hypothesized Mean Difference	0.00	
df	6.00		df	6		df	6.00	
t Stat	-1.98		t Stat	-1.97961		t Stat	-1.98	
t Critical two-tail	2.45		t Critical two-tail	1.94318		t Critical two-tail	5.96	
95%	Accept		90%	Reject		99%	Accept	

Appendix V

Sample	$\delta^{18}O$	$\delta^{18}O$ H_2O Qtz(Alpha) - H_2O (Clayton, et al. 1972)
H58SQA	13.96	5.76
H58PQ	12.85	4.65
HRPV	13.70	5.5
HRFF	14.30	6.1
HRFP	13.66	5.46
CFI4	13.45	7.55
MRC2 25/27	14.23	8.33
MRCQ 25/27	14.41	8.51
MRCLAV	14.45	8.55
MRCBC	14.58	8.68
S27BQ	14.54	8.64

Alpha delta fractionation calculation based off quartz (alpha) ⇔ H2O (Clayton et al., 1972) of selected quartz samples from MRC, HR and Sheba Mines.

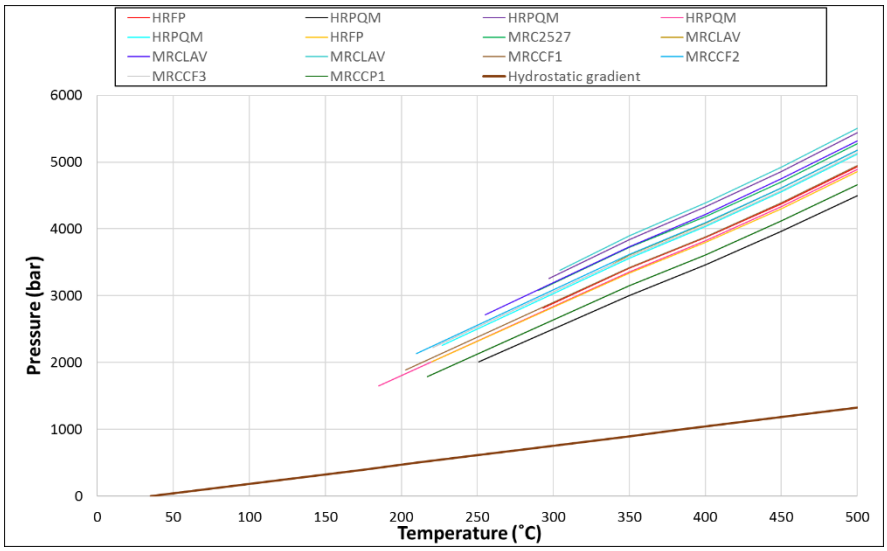

Isochore plot from homogenization temperatures of samples listed in key. The calculations assume 40% vapor phase and that the fluids trapped at around 1.6 to 3.5 kbar. These calculations are based off of minimum P –T formational conditions.

Appendix VI

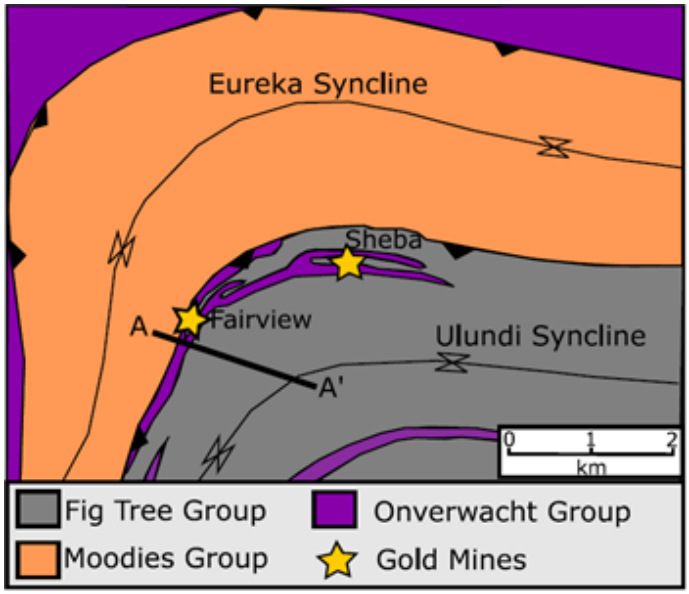

A to A' transect of cross section in figure 2.2. Here the location of Fairview and Sheba Mines are indicated along with the lithological groups.

Appendix VII

Sample	Chip	Type	T_{fi}	T_m	Tmice	T_{cm}	T_h	T_d	T_n	Salinity wt %	Notes
MRCFP22	5	P	-41.3	-66.5							FI is larger than surrounding ones with an oblong shape. There is about 35%V with the rest Lphase. The edges of the FI got darker upon freezing point.
	2	S	-36	-22		9.8	275				Irregular shaped with large V at 40% to L phase. At 9.4 the V bubble started to move along with surrounding V bibbles in FI.
	3	S	-40	-54		8	225.6				Upon heating to room temp the vapor bubble did not fully go back to original shape
				-48.5		10.5	256.9			-1.0686	
	E1			-59.2							Chip does not have many FI but there are many small monophase inclusions
	B1										
	2	S	-32.5	-54.4		14.8	337			-11.69	6.6 the FI V nbubble began to move. The V bubble changed shape at what looked to by the mentioned Tm temps however the size of the FI made it difficult to properly see at 210 the V bubble moved wthn the L . The FI did not homogenize so much . Temp was increased to 360 and the qtz cracked but not many FI homogenize. Why could this be? Could be the density of the FI and that the internal pressure of the FI is too high to be influenced by the heat . THe temp may have to go higher for it to homogenize the smaller FI.???
				-59.5			335.4				
	C1	S		-57.5	-12		324				Much larger FI about 8-10 UM the vapor bubble is about 45% to the L phase. Laarger FI are rounded while smaller are more boxy. There are some FI that are streched out. At 8.1 the V bubble began to move . There are several FI that have smaller V bubbles within the V phase and begin to move at 1.0 other FI appeared againart - 12 at 7.1 the V bubbles began to move again . t tlooks as though tthere are trapped solids in the FI. The L phase is dominate in most of the FI about 70-75% At 11.1 the V starts to move around . There is a mixture of monophase FI with two phae and some FI with what could be a trapped solid. This sample has a variable and recognizable amount of different FI types
			-40.3	-35	-11.8		353.6				This chip was heated to 370 and no FI homogeniezdddddd . At temps around 300 some V bubbles moved around..
	D1		-38.9	-52.3							Irregular shaed with a small tail large vapor phase more isolated with mono phase small FI about 2-4 um surrounding. At 11.8 thr V bubble began to move
				-41							
			-34.9	-12.4							This FI looked to melt around -12.4 and could have a clathrate in it but it is difficult to indicate.
		P	-60.8	63	-12.4		284.9				At 101 a FI whch looks to have two V bubbles the small inner Bubble began to move
MRC2527	A1	S		-23.1			312				Larger irregular inclusion which vapor bubble moves at STP FI is about 6-7 um with a V to L porpotion about 30% to 70% L. There are other inclusions in the area which are a lot smaller but there are also others that look the same in size therefore this FI is interpretted as secondary. At -21.2 at the top of the V it looks as if either a clathrate formed or the V bubble started to freeze? The FI got very dark but it was difficult to catch the first freeze. At about -23.1 the inclusionbegan to melt. At 10.5 the V bubble began to move again.
					-23.1						Smaller FI about 5 um with 25%V and 75% L. Roundd shape. At -6.5 the V bubble was fully visivle again. At about -54.7 the V bubble began to show
	2	S	-38.8	-54.7	-6.5		227				
	3	P		-51		13.9	290			-9.24	Larger I solated FI irregular rounded shape with a small V bubble that moves a lot at STP there looks as thought there could be a trapped solid within. At 13 the V bubbe stoped moving. The sample was heating to 310 in increments of 20 degrees from 180 at a rate of 10c/min. THe vapor bubble grew but it did not fully homogenize when temperatures were set to 310
	4	S	-31.2	-53.6	-7.7		298.8				Cluster of FI with varying size and shapes. V-L is about 20-35V to 80-70 L. No change was indicated when temperature was dropped. Ice formed on the top of the sample making it difficult to see FI. The ice melts at around -7.7 on the surface of the sample.
	5	S									
	6	S									
	B1	S		-53.1	-18						Rounded oblong FI with about 40%V to 60% L two phase in line with another FI that has a 35%V and 65%L there are toher FUI surrounding the area that are showing brownian motion. At 18 the main FI began to move
	2	S	-44.3								A lot of altered FI that are stretched out all followijng the same trend.
	3	P	-13								This chip has the primary zoned quartz grain where most of the primary FI are decrepitated and emptied out leaivng them looking dark and black. The first samples FI is rounded about 6-7 um and has a 40%V- 60%L porportion
	C1	S	-47.3	-50.2	-8.3		295				Cluster of FI about 5-7um one showing motion at abpit 13.2 . The L-V porportionsare about 30-35% V to 70-65%L. Ice formed on the surfacec of the sample making it hard to see inclusions but at -50.2 the V bubble took normal shape. At 8.3 the V bubbles began to move again.
		S									
		S									
	2										
	D1	S	-41.7		-12.1		345.2				Clusters of 2nd FI in no prefered orientation as there is multiple over prints of FI, some of which have been emptied and decrepitated out. All round shaped about 4-6um with a two phase about 30-35% V and 70-65% L there are also Monophase FI which are much smaller around 2-4um. At 12.1 the V bubble beganto have motion
	2		-30.3								
MRCLAV18											
	A1	S	-49	-61							FI is rounded slightly irregular with a 40%V phase to the rest L. there are many difformed and empties out FI in the area and through out the sample. There is no prefered orientation to this FI but it is more isolated than other nearby FI.Multiple FIA are present containinf secondary FI which also are seen clustering in areas causeing a black or shadowed apreance in the sample. At 7.4 the V bubble began to move again
		S		-61.2							
		S		-56	-10.2		338.9				At 10.2 the FI began to move again
				-19.8							
				-8.4							
			-29.5								
			-42.7								
			-58.7								
		P	-63.8	-51.8	-8		255.4				at -8 th FI all began to move again and at 10.2 all FI moved more
		S	-33.7		-10.2		328				At 70 the FI (smaller onse about 2-4 um) began to move at 189 a v bubble began to mover
		S	-37.2	-22.1	-7.8		333.4				
MRCLAV18	B1	P	-53.6	-48.7							The FI are overlapped with multiple fluid generations. It is difficult to indiccate Primary vs secondary. Clusters are larger inclusions are about 6um but are still difficult to see.
			-69								
			-36.7	-59.9							
	B2	P	-28								Clusters of secondary FI . It is not easy to indicate if there are any Primary inclusions due to the clustering and the lack of orientation. The area around alteration bearing regions and sulphide bearing within the sample show more barren FI over areas where there is minimal alteration and more qtz rich. It is likly that these secondary growths and alteration frophases "washed away" preexisting FI. Most FI show very similary physical features and size with two phases. Most homogenize around the same temp ranges ect.
		P	-30.6								
		S		6.8							
		P	-35.2	-18							FI are both larger than surrounding FI with about 6-8um and a V phase of about 25-30% and the rest L. These are indicated as primary cause they are more isolated and are not oriented like the smaller about 2-6 um FI in the surrounding qtz. There are small cubic sulphides near by with some minor rutile grains about 20-25um big, within the qtz.
		P	-33	5.4	-8.6		315				Rounded FI about 6-8 um more isolated than smaller fias. At about 7 degrees the V bubble began to move. At 8.6 the V bubbke began to move again. It was difficult to catch the melting temp of the two chossen FI . These inclusions will be homogenized to see if they are similar to others.
		P	-34.5	10							
				-49							
	C1	P		-62.6	-5.3		304				FI are a lot larger than surrounding more oriented FI . These are about 6-10um and have a larger V phase about 60-65%. At about 5.3 degrees the V bubble began to mve. Some of thes FI that are believed to be Primary have been stretched ut and have bent tails.
		P									
		P			-6.4		249				
MRCLAV18											
	D1	S	-36.3								There are several different shaped FI a few which look to have two v bubbles a small within a lrger one. This FI follows a qtz grain and at 6.4 the V bubble begins to move. It is about 75%V and 25%L Smaller secondary FI surround throughout the qtz grain. Two seperate chips were tried and no melting temperatures were found.
		P	-39.7								
		P	-32.6								
			-39.5								
	D1	P									There is a healed fracture that have larger FI and smaller secondary ones surrounding (2-4um). Picture MRCLAV18D2 is a heal fracture with secondary and primary inclusion.
		S									THIS SAMPLE SUCKS
		S									
	D2										
		P	-54.3	-68.5							Larger Fi that is about 8um . Shows motion around -5 to -20 and froze around -54.3. About 45% V and the rest L
	D3	P	-33.5	-52.6		7.2	403	403		5.41	
		P			-11.3		402	402			Large FI Aabout 8-10umwith 35-40%V . 11.3 moving in V bubble
	D4	S		-54.9							between 80-40 the V bubbles be gan to move. The V bubble got bigger at 200 the V bubbles began to move again but gotsamller and it continues to
		P									Type 1 inclusions at room temp. This looks to be a primary FI surrounded by other smaller 4um FI . This has about 25-30%V and the rest L
		S	-45.7			10.4	299				
		S	-35.8			8.7	304.2				ALL VAPOR BUBBLES GROW AND FI HOMOGENIZE TO THE VAPOR PHASE
		S				9.9	322.9				
		S				12	367.6				
		S				13.1	372.5				
		S				7.9	404.5	404.5			Dcrepitated!
		P				8	408.7	408.7			
	E	P	-39.3		-8.1		299.8				Primary FI ALONG RECRYSTALIZED Qtrz grain boundary. There are other two phase FI in the area of smaller size about 4 um this one analysised is about 6 um with a V phase of about 60%Smaller FI V p is about 40 %
		P			-7		325.6				
		S			-5.9		373.7				
		S			-9		382.3				
		S			-5.5		400				

Appendix VIII

Sample	Chip	P/S/PS	T_{fi}	Type	Tmice	T_m	T_e	T_{cm}	T_h	ThCO2	T_d	T_n	Salinity wt%	Pressure Correction Mpa	Notes
HRPV6	A1	P	-55.6					X	X		X	X			Glass window keeps frosting up when max freezing temp is reach and system begins to heat up to room temp. This limits visibility of inclusion during warming up.
	A2	P	-56.9			X		X	X		X	X			FI is at the edge of qtz grain and larger than all other nearby FI
	A3	P	-57.2			X		X	X		X	X			FI along edge of qtz grain with approx. 30%v-70%L phases. Circular in shape with a slight boxiness to its outer bubble. Near a black shape that looks almost like a bird/eagle...
	A4	P	-58.9			X		X	X		X	X			FI in close proximity to A3 but not apart of the same FIA. Also along qtz boundary with a larger L phase than V about 75-80%L - 25-20%V
	A5	P	-58.7			X		X	X		X	X			
	A6	P	-54			X		X	X		X	X			Larger FI about the same size as A3-4 has a smaller V phase about 25%.
	A7	P	-55.5			X		X	194		X	X	29.0396	5.72859	Smaller irregular FI more boxie with a larger V phase about 50-60%. L phase mor difficult to see. Pump could not lower anymore than -58 (I believe cause it is low on N2 and there are little crystals that formed at the bottom of the dewer so this may also have got caught in the screen.
	A8	P	-57.3			X		X	197		X	X			FI showed motion at room temp. with a 30%V -70%L phase. There were other smaller FI nearby that were also showing motion @ STP. The LPN could not cool lower than -58 due to low levels. LNP speed is set to 50 auto causes too much stress for the pump...
	B1	P	X			-58.9	X	15.7					-14.856		Large rounded FI with about 30%V to 70%L there are other FI in the area that have a larger V phase and are smaller.There seems to e a small black clathrate perhaps that formed at about -15 At about -58.9 the FI became less dark and the bubble was more visible. At 15.9 the two phases werer promenant and the clathrate that could have been there was gone.
	B1	P/S	-51.02												Large FI that is a bit elingated on one side with a larger L phase than V . This is about 8um big this inclusion. You can see others that are also large. There are lots of FI in trails but may are over printed and emptied out. This is indicated by the large amount of black specs in the Qtz that once were FI but due to furhter deformationa dn fluid pulses through the veins these older FI have been altered and distorted. FI is moving when temperature decreases ata bout -5. At -5.7 the FI began to take shape in V phase. At 2.2 the v MOVED TO THE TOP OF THE FI AND at 10.2 the V moved to the bottom and returned to shape at STP.
											10.2				
		S	-33.1	I											This sample entierly has much overpronting and very small FI makain g very difficult to inducate the phases differences and F/H data. Note the abundance of decrepitated and emptied FI and ones that lok black and glassed over. There are very small trails of FI that seem to be Monophase but it is difficult to tell due to lack of magnification. This sample is not hte best representation but there are some larger FI in the chips selected.The saple contains alteration zone with some minor sulphides present it could be that this area that was blended witht he alteration untit got heavelly altered by the interaction of fluids to wall rock hence creating the ateration we see.
		S			-4.3				231						
									273						
	AS	P			-10				280.3						
					-5				300.4						
					-5.7				352						
					-10				241						
	A7	S													Small about 5 um FI that has smaller fi in the surrounding area. There is no prefered orientation to this FIA. The V-L % ia bout20-25%V the rest L. secondary FI homogenized to the Vapor state
					-1.2				329						
HRFP12		P						10.5	340						
	F1	P		I	-8.2				263						Lots of monophase FI in this sample.... Lots of recrystalized quartz as well...
	E1a	P	-27		-11	-59.6		X	290		X	X			two phase inclusion 60 TO 40 VL, vapor bubble atarts to move at about -11
	b	P	-28.9		-11	-56.1		X	284	-11.2	X	X			sample with trapped solid 30 to 70 VL, sample also moves around -11 and also between -13 to -28
	c	P	-31.04		-13	-52		X	324		X	X			small two phase inclusion about 60-40% VL
	d	P	-18			X		X	194.5		X	X			at about -18 the FI formed what looks like a clathrate and around -58.3 the chip looked to freeze completely, looks like there was a solid that formed or dissolved at about -11.2to -12. Sample has not homo even at 270 but vapor bubble did move to the other side of FI and got larger until it was about 60 to 40 percent VL. other fi nearby homo at 194.5 at 30 to 70 VL
		P	-20			-58.3		11.2	271		X	X			
	D1a	P	-34.5			-54.2		X			X	X			Elongated shaped inclusion with 40%V to 60%L
	b	S	X			-42.8		X			X	X			
	c	S	X			-48.7		X			X	X			
	d	P	-27.5		-14.9	X		X	312	14.9	X	X			elongated FI frozen around -27.5. Ice crystals formed on sample and dissapeared around 0.1 . The bubble was visible around 14.9 about 30% V to 70% L
			X			X		14.9	293		X	X	-11.97		
	C1a	P	-36.7			-39.4		19.5	282		X	X	-26.63		inclusions did not homogenize even at 300...
	b	P	-31.2			-35		10.3	226	14	X	X	-2.846		more boxy shaped inclusion with about 40%v to 60% l
	B1a	P	-37.3			-54		X			X	X			inclusions are various one is elongate which froze at about -37 and the other is larger boxy rounded and looks to have a small trapped solid
		S	-56.3			-47.2		X			X	X			
	A1a	S	-53		-1.4	1.4		X	249		X	X			Round inclusion 40%V to 60% L josh veiwed this data set and believes he saw the inclusions bubble moving at about 1.4
								X			X	X			
HRPQM8	B1a	S	-31.3			-58.2		8.8	251		X	X	2.4		FI is oblong and round with about 30%V to 70% L at -10.1 the vapor bubble began to show motion and move. These three inclusions are interpreted as secondary as they follow the same assemplage and are thought to be of CO2 rich components as they all lunfroze at about -56 at -44.6 the vapor bubbles begion to move
	b	S	-94.7			-57.5		X	257.3		X	X			
	c	S	X			-56.7		X			X	X			FI are round with about 35%V to 65% L . The vapor bubble is promanaent in most inclusions and there is motion at temperatures less than -10 and upon heating to room temp. These inclusions are seen within quartz near elingated rutile grains. Monophase inclusions are very abundant in this sample maybe indicating a very rapid drop in P-T conditions during the time fluid passed which in turn allowed th e rutile to grow.
	d	S	-41.3			-59.8		X	269.9	21	X	X			
	e	S	-90.3			-52.1		X			X	X			
								X			X	X			
	A1a	P	-31.4			-66.3	-51.9	16.3	X		X	X	-16.05		Elongated FI with about 35%V and 65%L . It looks to have some trapped solids within but the inclusion is too small to truly tell at about 5-6 um. This FI sits along rutile grains and is seen being larger than surrounding secondary FIA with inclusions that look monophase in nature.
		S	X			X	X	X	X		X	X			
	C1a	P	X		21	-58	X	X	X		X	X			elongated rectangular FI with about 30%V to 70%L this is a much larger inclusion then the other ones present as it is about 10um big and the others are 5<. At aroubd -37.5 both inclusions seemed to get darker and lost original shape. Around 21-23 both inclusions original shape with two phases apeared. These einclusions are small about 5-8 um and are round but irregular in shape.
	b	S	-35			X	X	X	X		X	X			
	c	S	-38.2			X	X	X	X		X	X			
	d	P	-58.8			X	X	X	X		X	X			
	e	S	-47.9			X	X	X	X		X	X			four small (about 5<) are isolated in a small cluster. There arre etwo phases seen with about 25%V to 75%L in some and a bit more vapor than liquid in one. The first freeze was not indicated and hard to see but the FI look darker in color.
	D1a	P	-40.7			-56.3	X	X	X	8.2	X	X			isolated primary inclusion within quartz, irregular lobed shape with about 30%V to 70%L At about -440.7 the V bubble shrunk and a small "clathrate formed". At 8.2 the V bubble shrunk and moved
	b	S	X			-52.2	X	X	X		X	X			
	c	S	-32			-56.7	8	X	128.9	12.9			29.0396	5.72859MPa	larger FI with about 60%V to 40%L a large V bubble and irregular round shape inclusions at 9.2 a small bubble apeared within the larger vapor bubble and at 8.3 another small V bubble formed within a separate inclusion . This second FI is a quarter of the size as the first one. Small bubbles in each FI larger vapor bubble started to move again around 7.9-8 the small vapor bubbles disapeared around 12.9-13
											X	X			
	d	S	-31.6			X		X	147		X	X			
		S	X			X	X	7.9	297		X	X			
		P	X		-8.2	X	X	X	300		X	X			
			X			X	X	X	289		X	X			
	E1a	P	-38			X		X	X	16	X	X			at 10.6 a small v bubble formed and moves the FI seem to stop moving around -38 and the small v bubble reapeared at 8.9and disappeared again at 16.0
	b	S				-58.2		8 to 16	185.1						
	c	S				-57.1									
	d	S			-5.9	-46.7			198						Small secondary FI have about 40%CV to 60%L phases and are less than 5um big . A single isolated irregular shaped larger inclusion about 8 um has a V bubble about 30% and L at 70%. At 5.9 the smaller FI began to move around
	E	S		I	-10				221						
															This sample seems to have a variety of FI mainly monophase and two phase but there are FIA of secondary FI that looked to have three phases, Perhaps two liquid and one gas... The FI are quite small aboutS um making it difficult to see the third phase if it is present. Most FI are rounded with abput 35-45% V and the rest being L.. There are multiple secondary FIA cutting through the qtz grains surrounded by elongated apatite grains. There are grains pf rutile and apatite both seen within qtrz in this samle.
	F1	S			-9				297						
		S			-8.7				317						
															At-102 the V bubble began to move again. This FI is irregular boxy round... with a 20-25%v bubble
HRPQM7	A1a	P	X			X	X	X	X		X				Ice formed on sample as freezing experiment was done so could not see inclusions
	b	P	-63.4		-4.9	-61			271.5						there are lots of secondary FIA in qrtz and elongated rutile grains through out chip. This sample however has not shown promonent inclusions that are visile enough to indicate phase changes. Small inclusions look to be mono phase, the same as in sample HRPQM8
	c	P			-10.1	-46.5			284						
	d	S	-52.6			-50.7		9.6	281.4						At about -43 vapor bubble begins to move again. The V is about 20% and 80%L most of the inclusions are small in size about 5um or less
	C1a	P	-27.7			-68.5		10.2	227						P FI with 35%V and 65%L it has an irregular shap but a bit oval formed. Surrounding FI are secondary and much smaller than this selected one. It looks to be about 8 um big and the others are < 5um At o.6 the V bubble began to move
	b	P	-30.8		-11.2	-27									
	c	P						8.9	230						Several larger FI mixed with smaller ones. The larger di nit seem to follow any perfered orientation and the small are secondary FIAs The large FI have irregular shapes with somi whisp tails and the small secondary ones are roundf with about 45%V and the rest L the larger have about45% to 50% V and the rest L. The small are amout 30% V to L too.
	d	S						9	266.3						
	e	S				-51.6									Five FI in a cluster that look a bit larger then the surrounding FI that are <5um . These large FI have two phases and are about 35%V and 65% L
						-46.7									
	f	S	-33.8						492.6						
			-35.5												
	g	S	-35.7												Small round elongated FI with about 45%V at STP some have about 55% V Two phase FI for both. The smaples homogenized to the vapor phase
	H	P	-47	I	-9.7				287	X	X	X	13.62	12.7	Type I FI two phase with a v bubble about 45% round elngated, around -26 the FI formed a salt solid around the V bubble. This is an aqueous FI around -24.5 ice crystals formed and hydrohalites formed around the vapor bubble. This looks to be primary FI that was later overprinted with more carboic rich fluids.

T_{fi} = temperature of first freeze of vapor and or liquid phase(s)
T_m = first melting temperature
T_e = temperature of eutectic point (when both the V & L phases unfreeze)
T_{cm} = clathrate melting
T_h = homogenization tmeperature
T_d = temperature of decrepitation
T_n = temperature of nucleation
Salinity wt % = the recorded salinity of NaCl in fluid inclusion

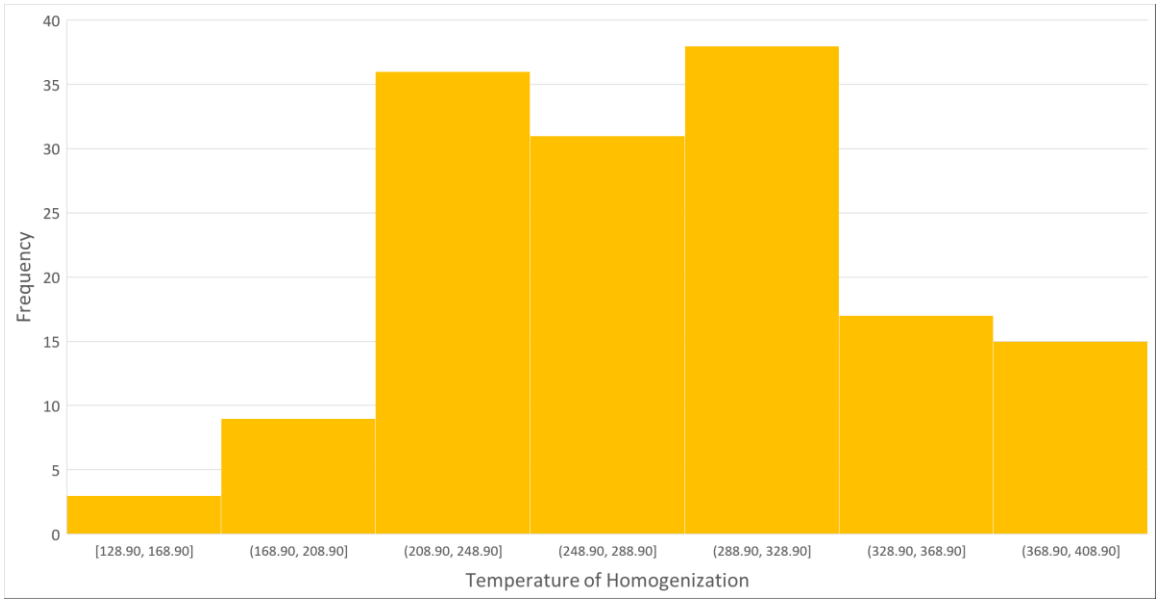

Histogram plot of FI homogenization temperatures verse the frequency of FI for both MRC and HR.

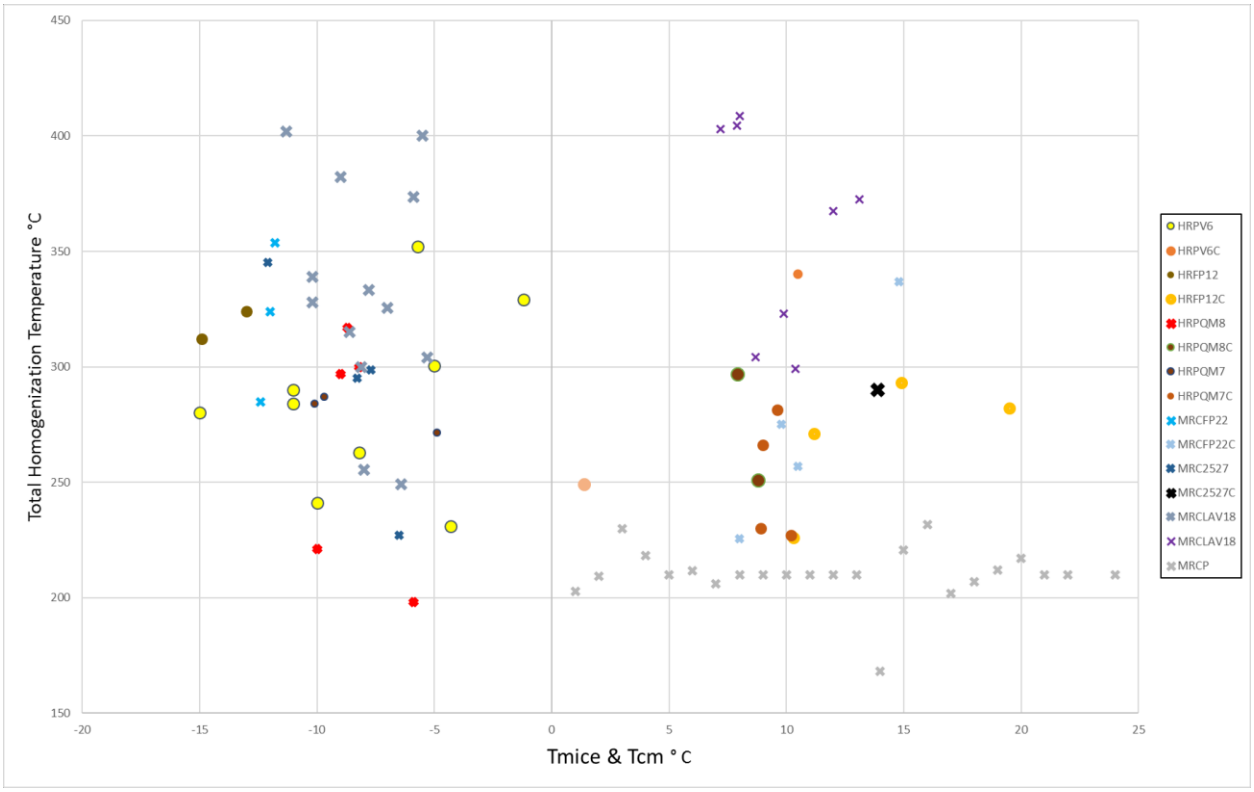

Microthermometry data for all samples quartz veins. To the left of zero are aqueous dominated FI and to the left are CO_2- H_2O FI. The crosses indicate MRC samples and circles indicate HR samples.